CARBON NANOTUBE GROWTH, DISPERSION, AND USE IN NANOELECTROMECHANICAL ACTUATORS

by

Michael Wright Forney

A dissertation submitted to the faculty of
The University of North Carolina at Charlotte
in partial fulfillment of the requirements
for the degree of Doctor of Philosophy in
Nanoscale Science

Charlotte

2011

Approved by:

____
Dr. Jordan C. Poler

____
Dr. James Amburgey

____
Dr. Patrick Moyer

____
Dr. Stuart Smith

____
Dr. Edward Stokes

____
Dr. Qiuming Wei

©2011
Michael Wright Forney
ALL RIGHTS RESERVED

ABSTRACT

MICHAEL WRIGHT FORNEY. Carbon nanotube growth, dispersion, and use in nanoelectromechanical actuators. (Under the direction of DR. JORDAN C. POLER)

The body of research comprising this dissertation spans the full spectrum of carbon nanotube (CNT) research: growth of CNTs, dispersion of SWNTs, controlled aggregation of SWNTs, and fabrication of CNT-based actuators. CNTs have been grown in our lab by chemical vapor deposition (CVD) and characterized by SEM and Raman spectroscopy. After growth, CNTs can be dispersed into a liquid for spectroscopic characterization or use in directed self-assembly, composites, or devices.

An important component of the dispersion research was focused on dispersing SWNTs into polar aprotic solvents containing methyl groups, where inappropriate ultrasonication conditions can initiate the sonochemical formation of methyl hydroperoxide, which destabilizes SWNT dispersions. This discovery was novel and had not been reported in the literature previously. That project lead to a careful study of SWNT dispersion stability at the "onset of aggregation", when ionic coagulants are added, in pure and mixed solvents. We found that optimizing bulk solvent parameters can enhance the stability of SWCNT dispersions in mixed solvents, which had not been published in the literature. After studying the "onset of aggregation", we studied critical coagulation concentrations (CCCs), which occur at much higher coagulant concentrations than the "onset of aggregation". We found that optimizing bulk solvent parameters does not enhance dispersion stability at the CCC. We also observed "transient stability" in dispersions that had NMP as the solvent or co-solvent. Computational work predicted that transient effects should be experimentally observable in NMP dispersions, but no experimental research has been published to support this prediction.

We have grown aligned CNT arrays onto microcantilever arrays to fabricate microcantilever-based actuators. This type of nano/microscale actuator has not been demonstrated in the literature. Also, we anticipate that these actuators will enable significantly larger microcantilever deflections than microcantilever actuators that employ other methods of force transduction. The CNT/microcantilever actuators developed in this project will provide an architecture that could be useful in applications such as nanovalves, release of drugs from a capsule, or nano-manipulation.

DEDICATION

I dedicate this dissertation to my amazing parents, who have provided me with a lifetime of guidance, love, and support, as well as my wonderful new family, Fe’Lix and Elijah, who motivate and encourage me daily.

ACKNOWLEDGEMENTS

I would first like to acknowledge the guidance of my advisor, Jordan Poler. Jordan has a wealth of scientific knowledge and is passionate about sharing his knowledge and experience. I have learned many valuable lessons from him and benefited from his willingness to mentor and support his students in every way he can.

I would also like to acknowledge and thank the members of my dissertation committee for their willingness to serve on my committee. I have appreciated their interest in my research and their suggestions for how to solve research problems. Furthermore, various members of the committee have helped me work on experimental problems, written letters of recommendation, and assisted me in finding job opportunities.

During my stay in the Poler group, there have been many fellow students that have helped me along the way. When I joined the group, Andrea, Harsh, Shiho, and Natalie assisted me as I adapted to working in a chemistry lab. Jeff has been an invaluable friend and labmate over the last few years. Josh and Anjail greatly assisted me in collecting data on the stability of carbon nanotube dispersions. Thanks also go to all the group members who have helped me indirectly, through their questions and conversations.

Thanks to Dan Deadwyler for his assistance in designing and building an electronics box to modulate a high voltage power supply’s output with a low voltage signal from a frequency generator or lock-in amplifier. Dan also helped me out on various other occasions and always has something interesting to say.

Many thanks go out to Caroline Kennedy, who has helped me out more times than I can count. Without her assistance and reliability, I would not have been able to get through this Ph.D. program. Beyond her professional skills, Caroline is always willing to talk and help out with personal problems or challenges.

Lastly, I would like to acknowledge the support of the Nanoscale Science Ph.D. Program, the UNC Charlotte Center for Optoelectronics and Optical Communications, and the Donors of the American Chemical Society Petroleum Research Fund.

TABLE OF CONTENTS

LIST OF FIGURES

LIST OF TABLES

LIST OF ABBREVIATIONS

2-PrOH	isopropanol
AAO	anodic aluminum oxide
AFM	atomic force microscopy
BQ	benzoquinone
BSQ	benzosemiquinone
BTB	bromothymol blue
CCC	critical coagulation concentration
CNT	carbon nanotube
CVD	chemical vapor deposition
D_2O	deuterium oxide
DFT	density functional theory
DI	deionized water
DLCA	diffusion-limited colloid aggregation
DLS	dynamic light scattering
DLVO	Derjaguin, Landau, Verwey, and Overbeek
DMA	*N,N*-Dimethylacetamide
DMF	*N,N*-Dimethylformamide
DNA	deoxyribonucleic acid
EDL	electrical double layer
EtAc	ethyl acetate
GC-MS	gas chromatography–mass spectrometry
H_2O	water

HiPCO	high-pressure carbon monoxide
HR-SEM	high resolution scanning electron microcopy
LMC	limiting molar conductivity
MD	molecular dynamics
MLCT	metal-to-ligand charge transfer
MWCNT	multi-walled carbon nanotube
NMP	*N*-methyl-2-pyrrolidinone
OM	optical microscopy
PID	proportional-integral-derivative
PMF	potential of mean force
PMMA	poly(methyl methacrylate)
PSD	position sensitive device
PVD	physical vapor deposition
RBM	radial breathing mode
RLCA	reaction-limited colloid aggregation
RMS	root mean squared
sccm	standard cubic centimeters per minute
SDS	sodium dodecyl sulfate
SEM	scanning electron microscopy
SWCNT	single-walled carbon nanotube
UHV	ultra high vacuum
UV	ultraviolet
VA-CNT	vertically-aligned carbon nanotube

VA-MWCNT	vertically-aligned multi-walled carbon nanotube
VA-SWCNT	vertically-aligned single-walled carbon nanotube
vdW	van der Waals

LIST OF SYMBOLS

$1/W$	inverse stability ratio
α	fitting parameter related to the effective interaction parameter w
A_1	asymptotic maximum in sigmoidal fitting function
A_2	asymptotic minimum in sigmoidal fitting function
A_F	scaling factor (fast)
A_S	scaling factor (slow)
β	slope of $d\log(\frac{1}{W})/d\log([coagulant])$ in the reaction-limited regime
B	parabolic rate constant
c_0	coagulant concentration
Γ_0	collection of terms (defined in text)
δ	Hildebrand solubility parameter
δ_D	Hansen dispersion parameter
δ_H	Hansen hydrogen bonding parameter
δ_P	Hansen polar parameter
δ_S	Hildebrand/Hansen parameter for the solvent
δ_{SWCNT}	Hildebrand parameter for SWCNTs
δ'	predicted optimal Hildebrand solubility parameter for SWCNTs
δ'_D	predicted optimal Hansen dispersion parameter for SWCNTs
δ'_H	predicted optimal Hansen hydrogen bonding parameter for SWCNTs
δ'_P	predicted optimal Hansen polar parameter for SWCNTs
d	diameter

ε_0	permittivity of free space
ε_r	dielectric constant
e	charge on an electron
E	energy
E_{EDL}	energy of EDL barrier
h	particle separation
H_{121}	Hamaker constant
H_{11}	represents interactions between solvent molecules
H_{22}	represents interactions between SWCNTs
H_{12}	represents interactions between solvent molecules and SWCNTs
I_S	scattering intensity
κ^{-1}	Debye screening length
k_{rect}	spring constant of microcantilever
k_B	Boltzmann constant
k_D	DLCA rate constant
k_F	aggregation rate constant (fast)
k_R	RLCA rate constant
k_S	aggregation rate constant (slow)
l	length of microcantilever
ν	Poisson’s ratio
n_S	number of moles of solvent
n_{SWCNT}	number of moles of SWCNTs
N_{SWCNT}	degree of polymerization ($N_{SWCNT} \propto$ SWCNT length)

π	pi
R	molar gas constant
$\Delta\sigma$	change in surface stress
τ	native oxide parameter
t	thickness of microcantilever
t	time
T	temperature
Φ_0	surface potential of dispersed particles
Φ_S	volume fraction of solvent
Φ_{SWCNT}	volume fraction of SWCNT
χ_{12}	Flory-Huggins interaction parameter
χ^2	statistical chi-square
χ_{DMF}	mole fraction of DMF
$V(h)$	DLVO interaction potential
V_{DMF}	volume fraction of DMF
w	effective interaction parameter
W	width of microcantilever
W_{11}	represents interactions between solvent molecules
W_{22}	represents interactions between SWCNTs
W_{12}	represents interactions between solvent molecules and SWCNTs
Δx	steepness of the transition between A_1 and A_2 in sigmoidal fitting function
x_0	center point of sigmoidal fitting function
Δz	microcantilever deflection

z	ion valence

CHAPTER 1: OVERVIEW

Nanoscale materials exhibit a blend of classical and quantum mechanical phenomena, offering rich basic research opportunities as well as great promise for applied research. Carbon nanotubes (CNTs) are one of the most exciting nanomaterials discovered. CNTs were first reported in 1991 by Iijima,[1] who discovered them when using an arc-discharge method of fullerene synthesis. Since their discovery, CNTs have generated tremendous research interest due to their unique properties. So many papers have been published on CNTs that Iijima's original paper has been cited over 10,000 times. Much of this interest originates from the fantastic properties of CNTs, such as their electronic one dimensionality and superior mechanical strength.[2-8] Furthermore, CNTs can be semiconductors or metals depending on the wrapping vector that defines their lattice structure.[9] The body of research comprising this dissertation spans the full spectrum of CNT research: growth of CNTs, dispersion of SWCNTs, controlled aggregation of SWCNTs, and functional devices that incorporate CNTs.

Significant effort has gone into building a CVD system and developing protocols for growing CNTs. The CVD system has gone through a series of upgrades and CNT growth parameters have been carefully studied. This has led to the capability of growing aligned CNTs on Si chips and microcantilever arrays. Growth of aligned CNTs on microcantilevers has allowed us to fabricate novel nanoelectromechanical actuators.

Future work in the group will also benefit from the ability to grow CNTs with well defined length distributions.

An important component of the dispersion research was focused on dispersing SWCNTs into certain non-aqueous solvents, where inappropriate conditions can inhibit formation of SWCNT dispersions due to solvent modification.[10] That work led to a study of the "onset of aggregation" of SWCNTs in DMF, DMF/NMP, and NMP. We found that mixed solvents can be used to optimize bulk solvent parameters, which can enhance the stability of those dispersions at low coagulant concentrations. This work has contributed to an ongoing discussion in the literature about solvents and solvent parameters for SWCNTs. After studying the "onset of aggregation", we broadened our testing of dispersion stability by measuring true critical coagulation concentrations of dispersions in DMF, DMF/NMP, and NMP. Further, we observed "transient stability" in NMP dispersions, which has not been shown previously, though it is theoretically predicted.

Current research is leading to the characterization of the CNT-based nanoelectromechanical actuators that we are fabricating. This type of nano-/micro-scale actuator has not been demonstrated in the literature, but it was inspired by various examples of related work on microcantilever and CNT actuators. Also, we anticipate that these actuators will enable larger microcantilever deflections than any related actuators that we have seen published in the literature. The actuators developed in this dissertation will provide an architecture that could be useful in applications such as nanovalves, release of drugs from a capsule, or nano-manipulation.

CHAPTER 2: GROWTH OF CARBON NANOTUBES

2.1 Motivation for Growing Aligned Carbon Nanotubes

One of the challenges of CNT synthesis is to create CNTs with uniform lengths and diameters. In order to study CNTs more carefully, it is necessary to synthesize relatively monodisperse batches. Additionally, any device that incorporates CNTs will require good control over the CNT properties and size. When researchers considered these needs, it was apparent that well aligned nanotube growth was a crucial step towards total control of CNT growth.[11] Growing vertically aligned CNTs (VA-CNTs) provides reasonable control over length and diameter of carbon nanotubes by adjusting growth time and other growth parameters.

CNTs have been synthesized through various methods, including laser vaporization, arc-discharge, pyrolysis, HiPCO, and chemical vapor deposition (CVD).[12] Each of these methods has advantages and disadvantages, but CVD is the most appropriate for growing VA-CNTs.

2.2 Applications of Aligned Carbon Nanotubes

Aligned CNTs are useful for a wide variety of applications. They were targeted for their potential as field-emission sources shortly after the first method for growing VA-CNTs was developed.[13] Electron guns have many uses in industry and research, as well as commercial devices.[13] Traditionally, cathode ray tubes have been used, where electrons are thermionically emitted from elements with low work functions.[13] Sharp tips have also been used for more precise applications in research and microscopy[13] because of the field amplification caused by the geometry of the tips. A major disadvantage to these older methods is that they require high vacuum to operate. Carbon fibers can provide a degree of improvement because they have less stringent vacuum requirements.[13] CNTs provide a better alternative than carbon fibers when grown in arrays of well-aligned nanotubes perpendicular to a surface.[13] de Heer, *et al.*[13] demonstrated successful fabrication of several field emitters that performed well in air and showed large field amplification as early as 1995.

Aligned CNTs can also be used to create nanoelectrodes. For example, Koehne e*t al.*[14] have successfully fabricated nanoelectrodes from arrays of multi-walled carbon nanotubes (MWCNTs). They are able to control the density of the nanoelectrodes and characterize their properties. Additionally, they demonstrated that highly sensitive electrochemical sensors could be created from nanoelectrodes formed from well-aligned MWCNTs.

Similarly, research has been done to explore the use of carbon nanotube based electrochemical biosensors.[15] The use of VA-CNTs has enabled improvements in the performance of nucleic-acid sensors, immunosensors, and other biological sensors. Furthermore, VA-CNTs efficiently transfer electrons from enzymes to electrodes.[15]

2.3 Methods for Growing Aligned Carbon Nanotubes

2.3.1 Multi-Walled Carbon Nanotubes

There is great variety in the methods used to grow aligned MWCNTs by CVD. The primary factors that affect growth are the substrate, catalyst, feedstock, carrier gas, temperature, and time of growth. Researchers have been varying these parameters in a continuing effort to find the most effective and efficient protocols for producing high quality carbon nanotubes.

Silicon or silica substrates have been used more than any other type of substrate.[12,16-22] Sometimes the silicon or silica substrates are pretreated, but this has been found to be unnecessary.[18] In some cases silicon is electrochemically etched to enhance MWCNT growth by producing porous silicon.[16] Similarly, mesoporous silica has been used as a substrate, but in that case, iron nanoparticles were embedded directly into the substrate to provide catalytic nucleation sites for the MWCNT growth.[17] A markedly different approach that has been taken is to use anodic aluminum oxide (AAO) to form a template.[23] The templates are prepared with a honeycomb-like pore structure that defines the size of the MWCNTs and ensures their alignment.

Catalyst nanoparticles must be used to facilitate CNT growth by CVD. Typical elements for catalysts are Fe,[16-18,21,22,24] Ni,[20] Co,[19,23] or an alloy of those elements.[12] The manner in which those metals are deposited onto the growth substrate varies greatly. In some cases, the metal is deposited directly onto the substrate by e-beam evaporation[16,19] or thermal evaporation.[12] Sometimes pre-made nanoparticles are deposited onto the substrate.[17,20] Otherwise, the catalyst is introduced by means of a precursor molecule such as ferrocene,[21,22] $Fe(CO)_5$,[18] or $CoSO_4 \cdot 7H_2O$[23] in the gas phase. Typically these molecules thermally decompose to release the catalyst.

Catalyst can be applied to the substrate prior to CVD growth[12,16-20,23] or the feedstock and catalyst can be inserted into the CVD chamber simultaneously.[18,21,25] Either way, once a sample is prepared and put into the CVD chamber, a controlled gas environment is established. Typically the environment is Ar,[12,16,18,19,22] H_2,[17,20] or a combination of the two.[21,23,24] Next, some sort of carbon feedstock must be flowed through the CVD chamber. Several different molecules are frequently used as carbon feedstock. The most common molecules are acetylene[12,16-18,23,24] and methane.[19,20] Sometimes more complex carbon sources are used, such as toluene[21] or xylene.[22]

CVD must be performed at high temperatures to ensure that the feedstock can thermally decompose and re-form as CNTs on the catalyst particles. Depending on what method is followed, CVD chamber temperatures can range from 400 °C to 940 °C. Most protocols, however, grow VA-MWCNTs between 500 °C and 800 °C.[16-19,21-24] Singh *et al.*[21] observed that the diameter of MWCNTs increased with increasing CVD temperatures and this agrees fairly well with other studies,[12,17,20,24] though the conditions of a particular method can cause exceptions.[19,22] MWCNTs are then grown for 10-60 minutes, but usually between 20 and 30 minutes. In addition, some groups use a bias to help align the MWCNTs as they grow.[19,20]

2.3.2 Single-Walled Carbon Nanotubes

Vertically aligned single-walled CNTs (VA-SWCNTs) appear to be grown exclusively through some form of CVD; either standard CVD,[26-30] plasma enhanced CVD,[31] or point-arc microwave plasma enhanced CVD.[32-34] Growth of SWCNTs depends on the same factors as MWCNT growth: the substrate, catalyst, feedstock, carrier gas, temperature, and time of growth.

The substrates chosen for growing SWCNTs seem to be more limited than for MWCNTs. Almost everyone is using silicon[28,30-34] or quartz.[27,30] However, one group[29] did grow SWCNTs directly on a W electron tip with the aid of a 50 V bias. In that case, though, there is not much alignment and the growth density is poor.

Growing aligned SWCNTs differs from growing MWCNTs most when it comes to the catalysts that are used. Several groups have met success using Co-Mo[26-28] in various ratios. One group prefers to make an $Al_2O_3/Fe/Al_2O_3$ sandwich on top of their silicon substrate.[32-34] Similar approaches, such as using Co/Al,[29] $Fe\text{-}Co/Al_2O_3$,[31] Fe/SiO_2, Fe/Al_2O_X, or Fe/Al_2O_3[30] have also proven to be successful. Considering these layered catalysts, and the success of Parthangal, *et al.*[24] on metals with Fe/Al_2O_3, it should also be possible to grow well-aligned SWCNTs on metal or metal alloy substrates. The primary difference between SWCNTs and MWCNTs, aside from the choice of catalyst, is the preparation of the catalyst layer. When growing SWCNTs, it is necessary to ensure that the catalyst layer (or layers) is approximately 1 nm thick so that the nucleation sites are sufficiently small to grow SWCNTs.

The temperatures used for SWCNT growth had a slightly smaller window than for MWCNT growth. Almost all groups heat the CVD chamber to a temperature between 600°C and 800°C. Only Koizumi, *et al.*[29] use a temperature as high as 850°C and no groups have demonstrated growth temperatures below 600°C. The SWCNTs are allowed to grow between 5 minutes and 60 minutes, though usually between 20 and 40 minutes.

The gas environment for SWCNT growth is often the same as for MWCNTs, using H_2[32-34] or Ar/H_2.[26,27,29] However, there are some exceptions where groups have used H_2/He[28,31] or even $H_2/H_2O/Ar$.[30] Methane is again used as a feedstock,[31-34] though carbon monoxide,[28] ethanol,[27,29] and ethylene[30] have also been found to be effective.

It is worth pointing out that using an $H_2/H_2O/Ar$ environment and ethylene feedstock led to what Noda, *et al.*[30] referred to as "super growth" of SWCNTs. The SWCNTs rapidly grew to lengths of several millimeters. SWCNTs of this length have phenomenal aspect ratios of approximately one million. These SWCNTs are significantly longer then those grown by any of the other groups, who grow SWCNTs that are tens to hundreds of micrometers[28,29,31-34] or sometimes fewer than ten micrometers.[26,27] In all cases, the SWCNTs were determined to have diameters between 1-2 nm[26-29,31] or 1-3 nm[32-34] based on Raman spectroscopy.

2.4 Carbon Nanotube Growth Capability and Goals

2.4.1 Early Growth Protocol

Our first CNT growth protocol was loosely modeled on the work of the Hata group,[35-38] in Japan, who has been extremely successful at growing VA-CNTs. The first generation CVD system had a 1" diameter quartz tube, heated by a tube furnace (Figure 2.1). The gas profile used during CNT growth was $Ar/H_2/C_2H_4$, with flow rates of 300 sccm, 200 sccm, and 10-100 sccm, respectively. Growth lasted for 10 min and the temperature was held at approximately 750 ºC.

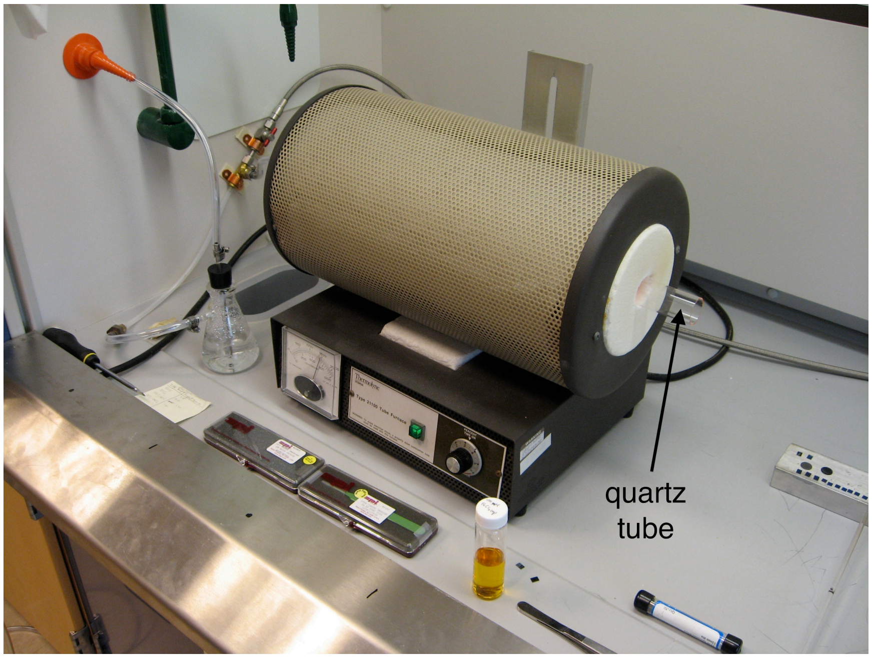

Figure 2.1: CVD tube furnace with 1" quartz tube. Used to wet oxidize Si dies and to grow CNT samples.

CNTs were grown on 5 mm x 5 mm Si dies that underwent several stages of sample preparation. First, the Si dies were washed with DI water, acetone, and methanol twice. Then the Si dies were wet oxidized at 1000 ºC for 1 hr, which formed approximately 500 nm of oxide on the surface. Next, a 10-20 nm catalyst support layer, Al or Al_2O_X, was deposited by physical vapor deposition (PVD) using a Lesker PVD 75. Lastly, a thin film of Fe was deposited by PVD. Growing SWCNTs requires a ~1 nm Fe film, but MWCNTs will grow from thicker Fe films. It has, however, been shown that MWCNTs will grow from ultrathin Fe films if there is too much carbon feedstock available.[39]

After sample preparation, dies were inserted into the CVD chamber in a 300 sccm flow of Ar and the CVD was ramped up 750 ºC in 15 min. After the temperature ramp, 200 sccm of H_2 was added for a 10 min annealing process to remove any surface oxidation of the Fe and to form CNT nucleation sites. Growth was then initiated by adding 10-100 sccm of C_2H_4 and lasted for 10-20 min. The H_2 and C_2H_4 flows were shut off and the CVD chamber was purged with 300 sccm Ar for 5 min, after which samples are removed.

This protocol provided initial success for growing CNTs. It was successful at consistently growing small diameter randomly-aligned MWCNTs. As demonstrated in Figure 2.2, the technique for growing randomly-aligned MWCNTs was relatively easy to achieve. Randomly-aligned MWCNT forests can be grown to lengths on the order of 10-20 μm in just 10 min, and the diameters can be tailored to be 10-100 nm by adjusting the thickness of the Fe catalyst layer. The loosely tangled growth morphology is consistent and repeatable using the above growth protocol.

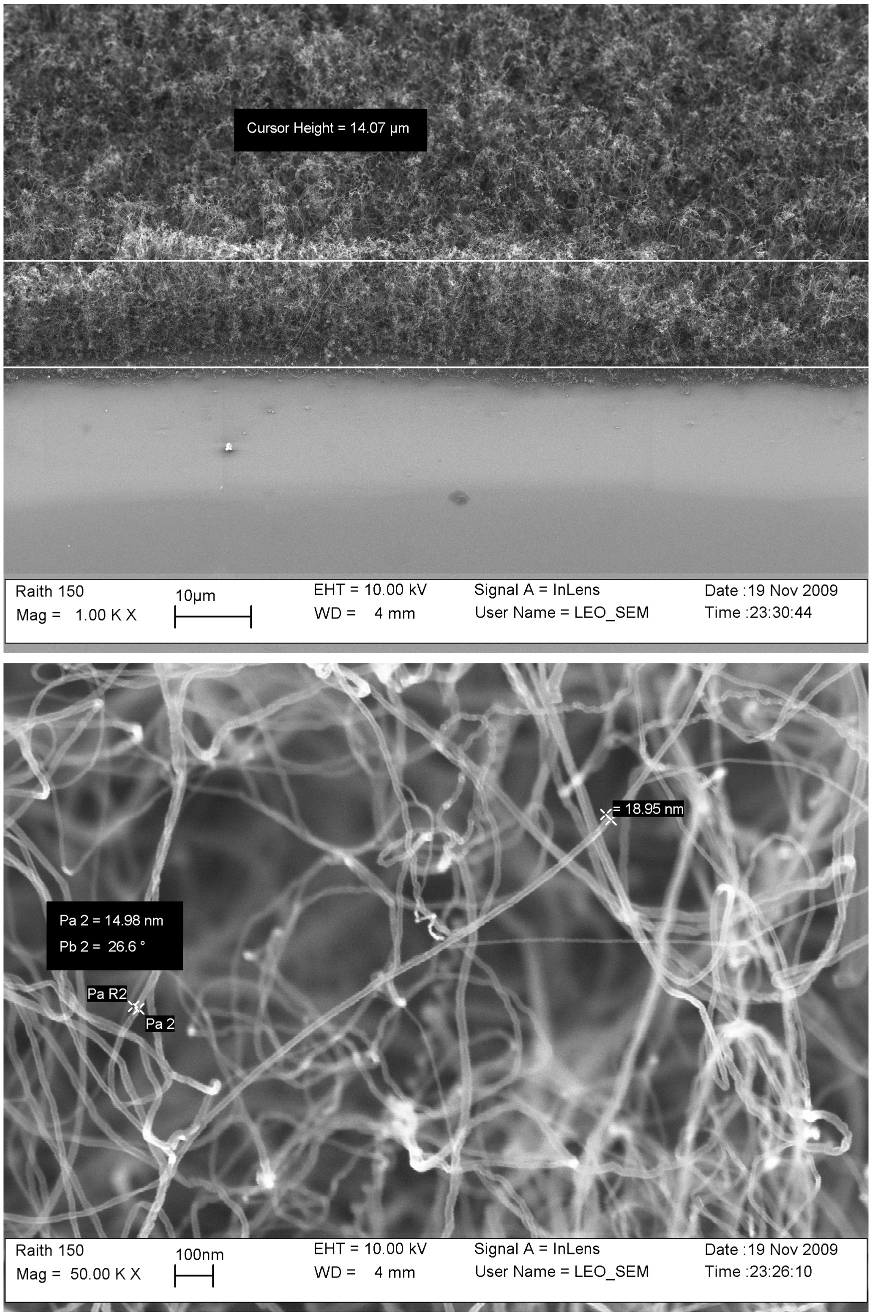

Figure 2.2: SEM images of randomly aligned MWCNT growth. Top: Randomly aligned MWCNT forest with an approximate height of 15 µm, viewed from a 45º angle. Bottom: High-resolution SEM image showing MWCNTs with diameters of 15-20 nm.

Growing SWCNTs under this growth protocol was generally unsuccessful, even when the Fe catalyst layer was approximately 1 nm thick. In a few instances, though, some domains on the sample produced what appears to be a region of “supergrowth” SWCNTs. The supergrowth regions grew SWCNTs that were hundreds of microns tall and blossomed from the surface in flower-like shapes that are much taller than the surrounding SWCNTs. Figure 2.3 shows the domains of flower-like supergrowth at the top, and Raman spectra proving that a significant percentage of the CNTs in the sample are SWCNTs. The strong G-band at 1600 cm^{-1} and weak D-band at 1300 cm^{-1} are indicative of high quality SWCNTs. Also, radial breathing modes (RBMs) show that SWCNTs are present, and the SWCNT diameters can be identified from the Raman shifts. The interpretation of these Raman modes will be discussed in more detail in Section 2.4.3. Unfortunately, these CNT growth results were difficult to reproduce, and the growth protocol needed significant improvement for consistent growth of SWCNTs. Moreover, the growth protocol needed to be improved so that CNT alignment could be controlled.

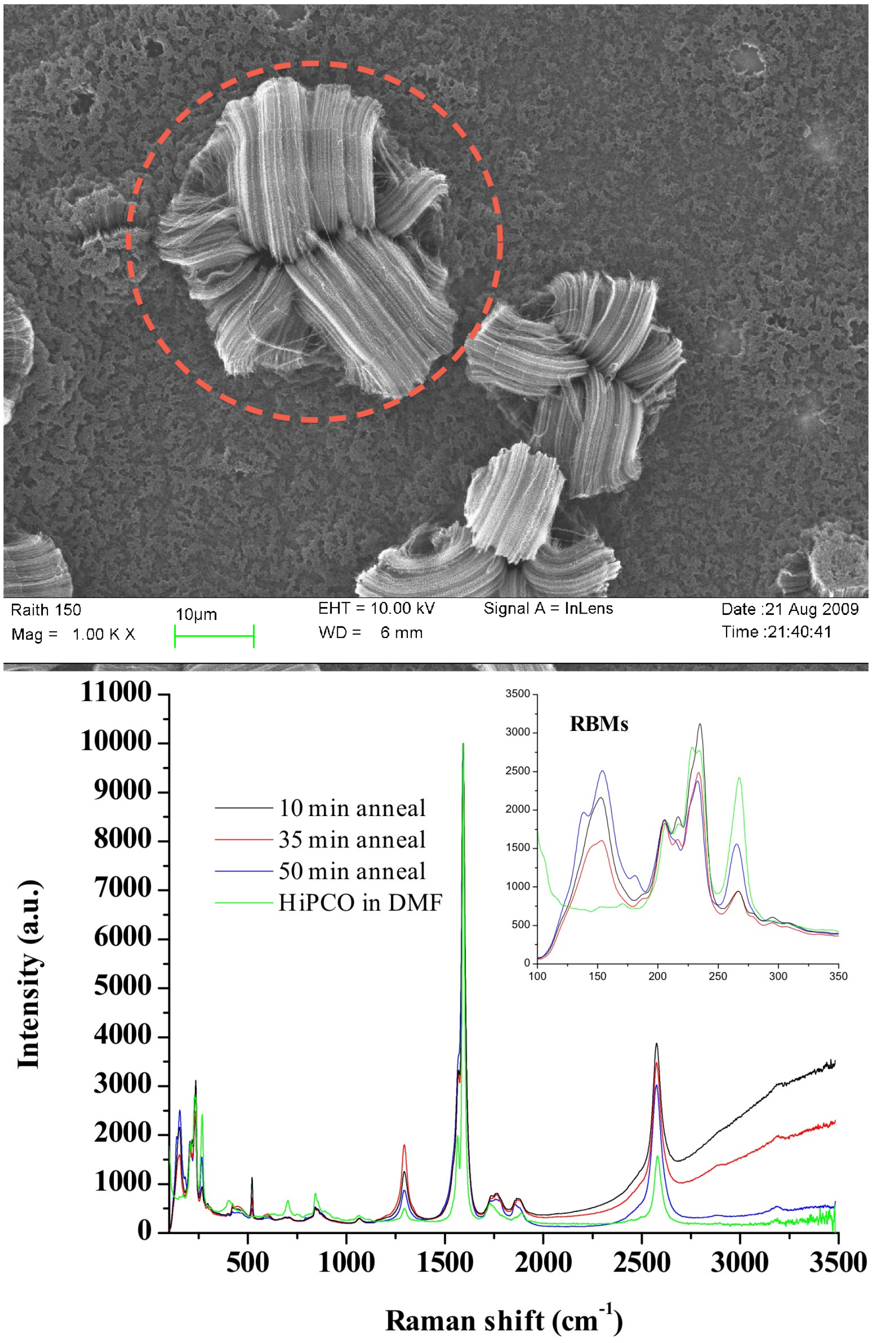

Figure 2.3: SWCNT “supergrowth”. Top: SWCNT growth, showing flower-like domains of "supergrowth". One such domain is circled with a dashed red line. Bottom: Raman spectra showing the strong G-band at 1600 cm^{-1} and RBMs that indicate the presence of SWCNTs (see inset).

2.4.2 Upgraded CVD System

In order to gain better temperature control in our CVD system, we upgraded from the simple tube furnace shown in Figure 2.1 to a Thermolyne 79300 Tube Furnace that has a programmable temperature controller, shown in Figure 2.4. We decided to carefully characterize the temperature profile of the new furnace to measure the width of the hot zone and to test the accuracy of the temperature controller. All temperature measurements were made with an Omega Model HH23 Microprocessor Thermometer, using a 12” Type K thermocouple rod.

The first test was to measure the uniformity of the hot zone across the range of temperatures that are appropriate for growing CNTs. The hot zone of the Thermolyne 79300 is 12” long, so we measured the temperature from the center to the outside edge of the insulating collar at 1” intervals. These temperature measurements were taken at 600 ºC, 700 ºC, 750 ºC, 800 ºC, and 900 ºC. The results, shown in Figure 2.5, reveal that the center 10” of the CVD have an extremely uniform temperature, and that the temperature only drops 10-20 ºC at the inside edge of the insulating collar.

Next, we tested the accuracy of the PID temperature controller. The tip of the thermocouple rod was placed at the center of the CVD, inside the 1” quartz tube, for the entire experiment. First, the CVD was ramped up to 600 ºC. Although the thermocouple in the furnace showed that the PID did an excellent job of bringing the furnace temperature to 600 ºC without overshooting, our thermocouple inside the quartz tube showed that the temperature inside the growth chamber does overshoot by about 25 ºC, and it takes over 30 min to come back down to 600 ºC, as shown in Figure 2.6. In the subsequent temperature steps, the overshoot stays below 10 ºC, as measured inside the growth chamber. These results show that the PID is well tuned to match the desired set point, but since the furnace thermocouple does not measure the temperature inside the quartz tube, there will always be some overshoot, unless a flexible thermocouple is threaded into the growth chamber.

We did not install such a thermocouple, but instead used a multi-step temperature ramp to get the thermal ramp profile that we desired, after measuring temperature profiles along the CVD and the response of the PID. The first test was a 15 min ramp to 750 ºC, then the temperature controller was held at 750 ºC, as shown in Figure 2.7. In this test, there was approximately 40 ºC of overshoot before the temperature inside the growth chamber started equilibrating to 750 ºC. We next added a second step in the temperature ramp to reduce the overshoot, ramping to 700 ºC in 10 min, then ramping 750 ºC in another 10 min. The second step in this ramp was too shallow and resulted in undershooting of the 750 ºC target, as shown in Figure 2.7. Lastly, we added a third step to smooth out the transition from the rapid heating, in the first 8-10 min, to holding the temperature at 750 ºC. The final temperature ramp protocol is to set the PID controller to ramp to 700 ºC in 10 min, then ramp to 740 ºC in 3 min, then ramp to 750 ºC in 20 min. This protocol yields a thermal ramp profile that matches our target profile quite well and with minimal overshoot. All subsequent CNT growth used this CVD temperature ramp.

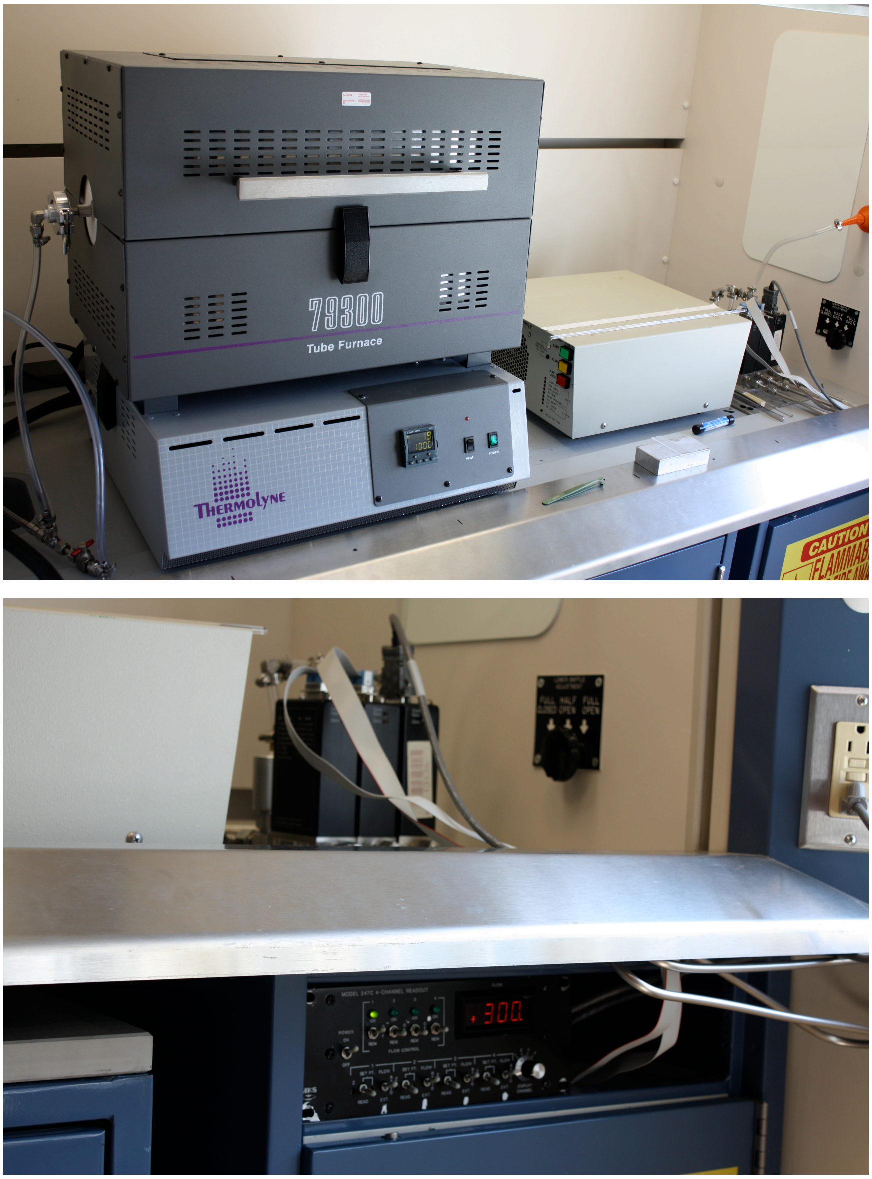

Figure 2.4: CVD system after upgrading to a Thermolyne 79300 Tube Furnace. The top image shows the Thermolyne 79300 and the bottom image shows the MKS Model 247C Flow Controllor (below hood) with the argon, hydrogen, and ethylene mass flow controllers (in hood).

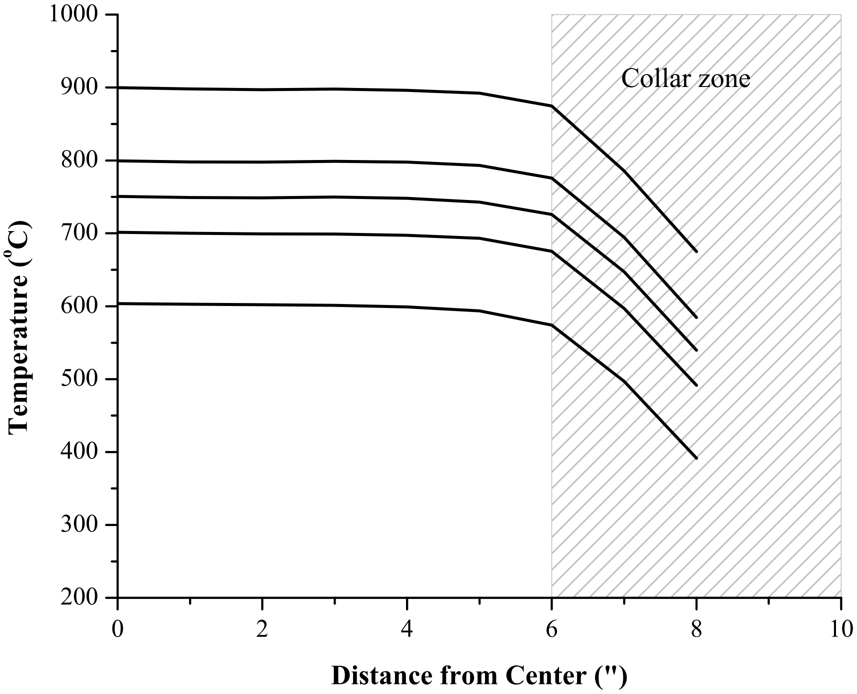

Figure 2.5: Temperature profiles along the length of the CVD using the Thermolyne 79300 Tube Furnace. Temperature set points, from bottom to top, were 600 ºC, 700 ºC, 750 ºC, 800 ºC, and 900 ºC.

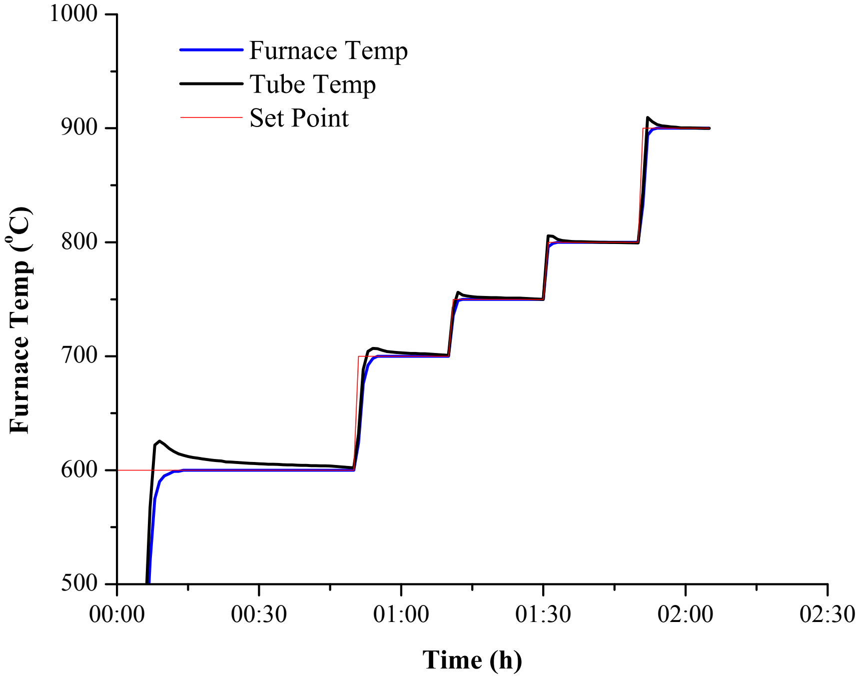

Figure 2.6: Temperature response of the CVD furnace. The red line shows the set point of the furnace. The blue line shows the temperature measured by the thermocouple inside the furnace chamber that the PID uses to control the furnace power. The black line shows the temperature measured inside the quartz tube.

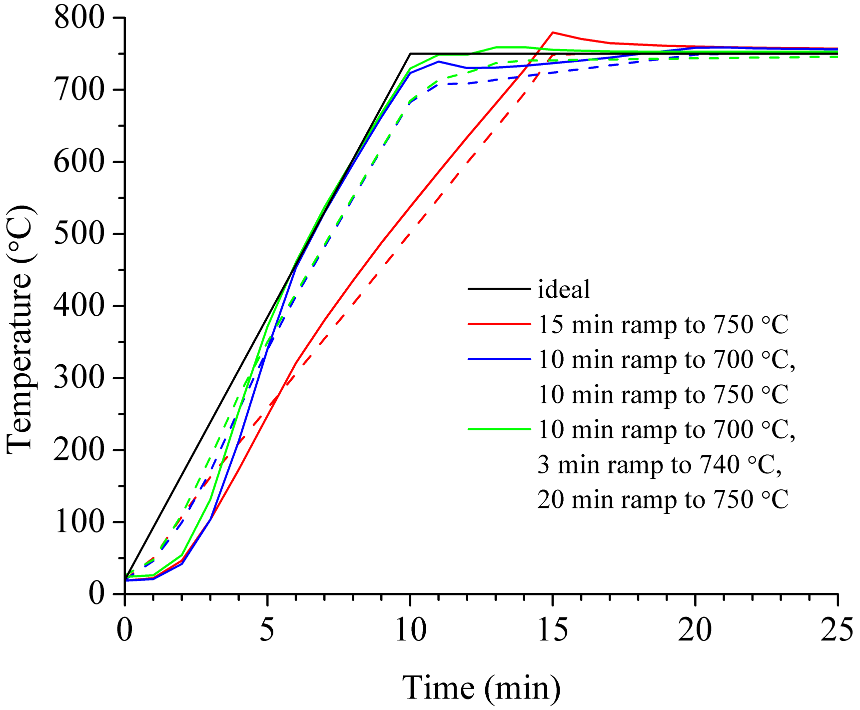

Figure 2.7: Thermal ramp profiles for Thermolyne 79300 Tube Furnace. Dashed lines show the temperature measured by the furnace's internal thermocouple and solid lines show the temperature measured inside the quartz tube.

In addition to testing the new furnace, we also included a test of the thermal ramp protocol that was used to grow CNTs with the old furnace. The old furnace did not have a controller and the furnace temperature is managed by a knob that controls the power percentage. A thermocouple gauge shows the temperature measured by the furnaces thermocouple, outside the quartz tube. The protocol that was developed for earlier CNT growth was to set the power knob to 6% power for 15 min, then the power was reduced to 3% power to maintain temperature. According to the furnace's thermocouple gauge, the temparature ramps to 750 ºC in 15 min, then holds at 750 ºC.

After measuring the thermal ramp profile inside the quartz tube with our thermocouple rod, it became apparent that the furnace's internal thermocouple gauge was extremely inaccurate. During the 15 min ramp at 6% power, the temperature was actually ramping up to 900 ºC, then it cooled down to 800 ºC after the power was reduced to 3%. It is clear that in our early CNT growth experiments, the growth temperate was quite different from our target temperature of 750 ºC.

In some CNT samples, such as the sample in Figure 2.3, we had observed a distinct change in growth morphology at some point during the CNT growth, as highlighted in Figure 2.8. We suspect that somewhere in the 800-900 ºC range, under our growth conditions, there is a change in the CNT growth mechanism that leads to a morphological change. In the first growth stage, the CNTs are relative straight, but they abruptly change to wavy growth that happens at a much faster rate. Most of the length of the "supergrowth" CNTs is wavy, which is why we assume a faster growth rate for the wavy part. This type of change has not been observed in any samples since upgrading the CVD system and developing an accurate thermal ramp profile.

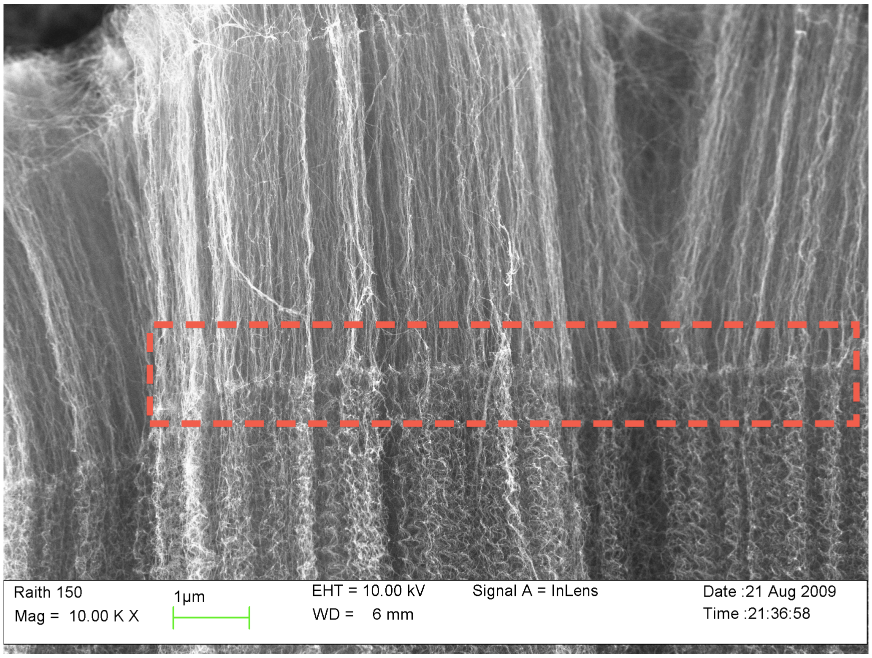

Figure 2.8: Distinct change in CNT growth morphology. The change in morphology occurs inside the red dashed rectangle. The top of the CNT forest has fairly straight CNTs, whereas the bottom has wavy CNTs.

2.4.3 Growth Protocol Refinement

After improving the CVD system by installing the Thermolyne 79300 furnace and characterizing the new system, we tested two key growth parameters: C_2H_4 flow and annealing time. The goal of these experiments was to improve our ability to grow SWCNTs as well as vertically-aligned CNTs. In these experiments, the CVD temperature profile was as described in the previous section, the Al catalyst support layer was 30 nm thick, and the Fe catalyst layer was approximately 1 nm.

2.4.3.1 Variation of C_2H_4 Flow

Most of the early CNT growth experiments used 100 sccm of C_2H_4 as the carbon feedstock, mixed with 300 sccm Ar and 200 sccm H_2. As mentioned previously, it has been shown[39] that an excess of carbon feedstock can lead to the formation of MWCNTs instead of SWCNTs, even if the Fe catalyst layer is as thin as 1 nm. We tested this observation to see if changing the C_2H_4 flow gave us the ability to control SWCNT vs. MWCNT growth.

Figure 2.9 shows Raman spectra for samples where CNTs were grown with C_2H_4 flow rates of 10-100 sccm. The spectra have been normalized to the D-band to facilitate comparison between the D-band (~1300 cm^{-1}) and G-band (~1600 cm^{-1}). It can be seen that the G/D ratio increases with decreasing flow rate, which indicates a lower defect density and more SWCNT character.

In MWCNTs, the G-band is a graphitic peak that shows up at 1582 cm^{-1}.[40] Also present in the Raman spectra of MWCNTs is a peak at 1620 cm^{-1} that results from a maximum in the 2D phonon DOS of graphene.[41] Vertical dashed red lines have been drawn in Figure 2.10 to indicate the location of those peaks. In the case of SWCNTs, the

G-band splits into G^+ and G^- bands at 1593 cm^{-1} and 1567 cm^{-1}, respectively.[40] The G^+ peak comes from phonons along the axis of the SWCNT and the G^- peak comes from phonons around the circumference of the SWCNTs.[40] In Figure 2.10, vertical dashed black lines show the location of the G^+ and G^- peaks. Inspection of the G-band in Figure 2.10 shows that decreasing the C_2H_4 flow rate increases the intensity of the peaks associated with SWCNTs and decreases the peaks associated with MWCNTs. More specifically, Figure 2.10 shows that a higher fraction of SWCNT growth occurs when the C_2H_4 flow rate is 10-30 cm.

Additional evidence for enhanced SWCNT growth at lower flow rates is the presence of RBMs (150-350 cm^{-1}). Figure 2.11 shows the RBMs at each of the flow rates tested. Several SWCNT chiralities have been identified and labeled in Figure 2.11, based on the work of Bachilo, *et al*.[42] As was noted in the G-band analysis, the RBMs indicate that SWCNTs are grown when the flow rate is 10-30 sccm. It should be pointed out that all CNT growth in these experiments was randomly-aligned and that the growth density was quite poor at the lower flow rates. For example, the 20 sccm sample, which had mostly SWCNT growth, is shown in Figure 2.12. The growth is clearly thin and patchy, and the growth substrate can easily be seen through the randomly-aligned SWCNT growth. Since the growth was even more sparse for a 10 sccm flow, 20 sccm was chosen as the best flow rate for future growth protocols, since it balanced the SWCNT growth quality and quantity.

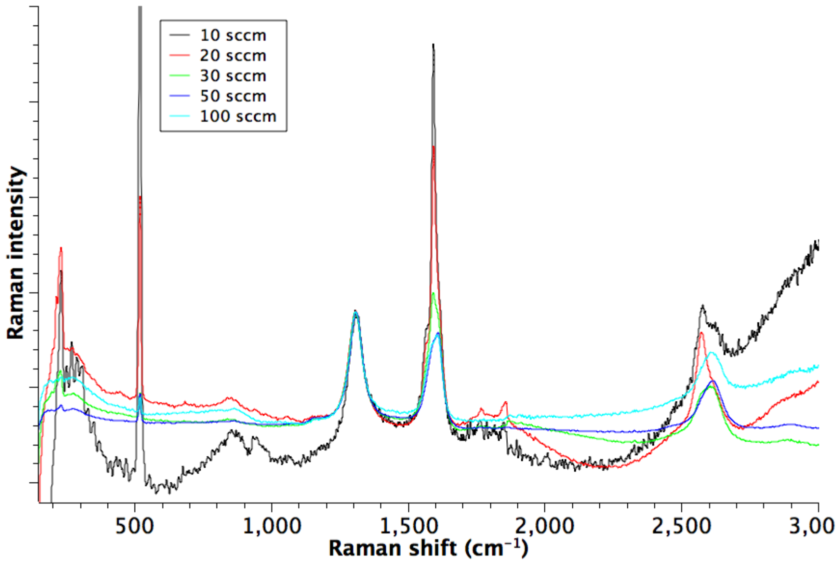

Figure 2.9: Raman spectra of CNTs grown with varying C_2H_4 flow rates.

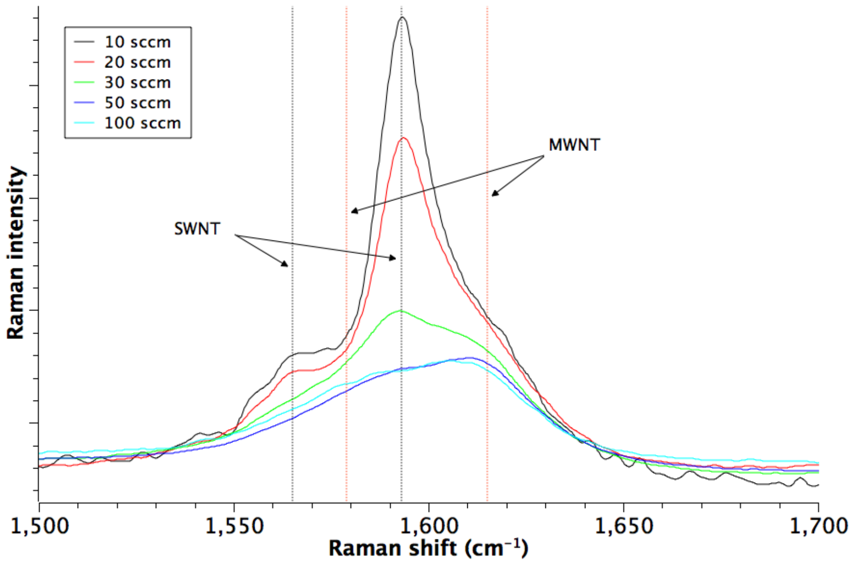

Figure 2.10: G-band from Raman spectra of CNTs growth with varying C_2H_4 flow rate. The G-band shows a transition from mostly MWCNT character at 100 sccm to mostly SWCNT character at 10 sccm. The vertical dashed lines indicate the peaks associated with SWCNTs and MWCNTs.

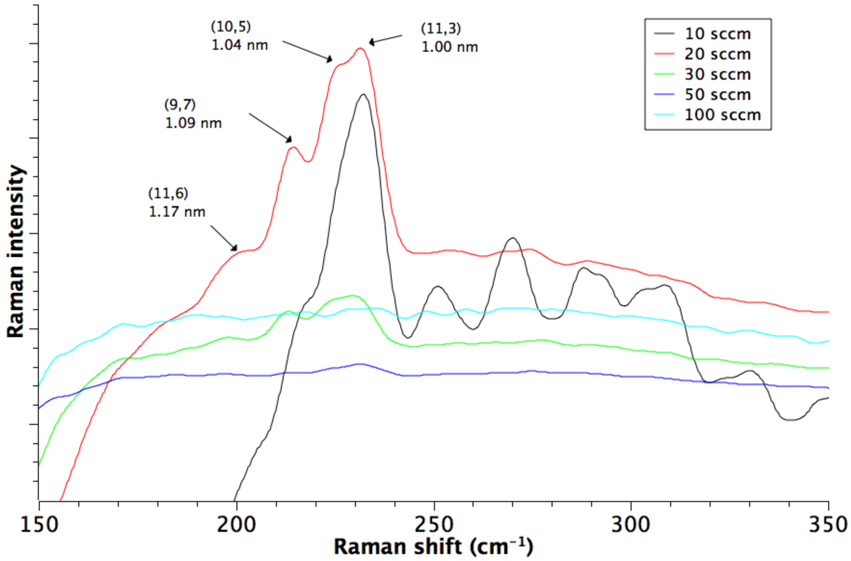

Figure 2.11: RBMs from Raman spectra of CNTs growth with varying C_2H_4 flow. Several RBMs have been identified and labeled.

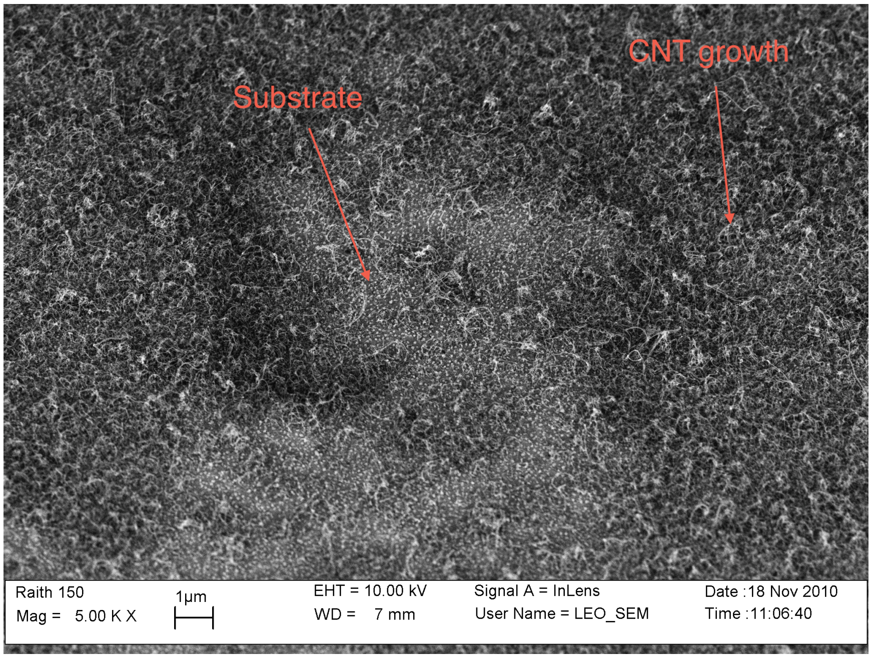

Figure 2.12: HR-SEM image of SWCNTs grown using a 20 sccm flow rate. The growth substrate can be easily seen through the thin SWCNT growth.

2.4.3.2 Variation of Annealing Time

After determining that 20 sccm was a good C_2H_4 flow rate for growing SWCNTs, we tested the effect of annealing time on SWCNT growth. Otherwise, the growth conditions were the same as described in the previous section, with a 30 nm Al catalyst support layer and 1 nm Fe catalyst layer. Three annealing times were tested: 10 min, 30 min, and 50 min.

Figure 2.13 shows the Raman spectra of CNT samples grown at each of those annealing times. Looking at the full spectra, which are normalized to the D-band, it can be seen that G/D ratio decreases and the strength of the RBMs decreases, indicating lower quality SWCNTs. The G-band, shown in Figure 2.14, shows that there are also MWCNTs for the longer anneal times of 30 min and 50 min. It is most pronounced in the 1620 cm^{-1} peak, but the G^{+}/G^{-} splitting also starts to fade away, especially in the 50 min anneal. MWCNTs probably start to grow with longer anneal times because an Ostwald ripening effect, where catalyst islands begin to merge and form sites where MWCNTs nucleate rather than SWCNTs.

The RBMs also show that the quality and/or quantity of SWCNTs grown is higher for the shorter annealing times. Figure 2.15 shows the RBMs, where the RBM intensity is higher for shorter annealing times. Three specific SWCNT chirality have been identified and labeled: (9,7), (10,5), and (11,3).

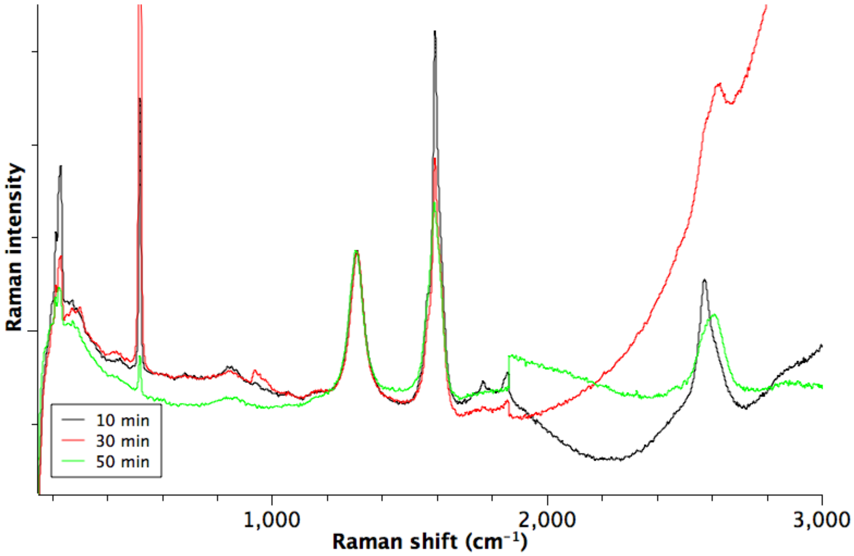

Figure 2.13: Raman spectra of CNT samples where the annealing time was varied. The large Raman intensity between 2000 cm^{-1} and 3000 cm^{-1}, in the 30 min sample, is an artifact due to poor sample alignment in the spectrometer.

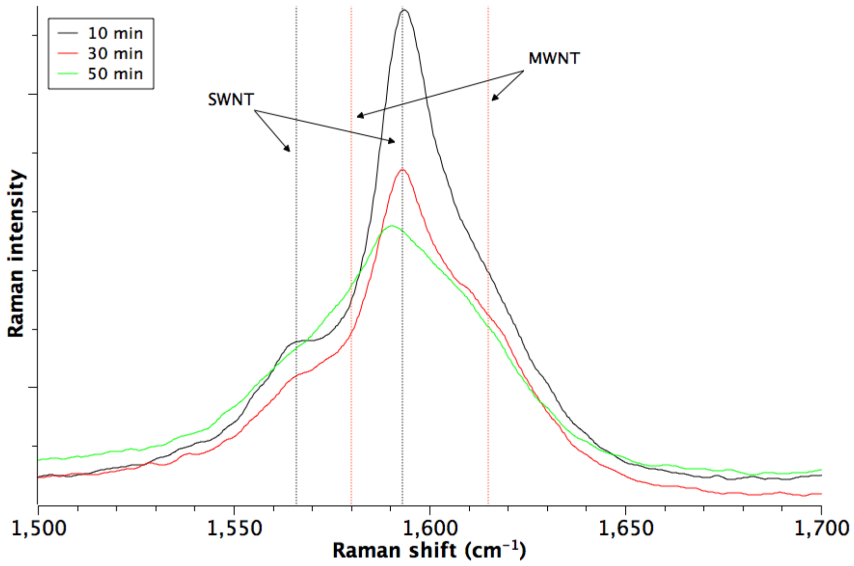

Figure 2.14: G-band of Raman spectra of CNTs grown with varying annealing times. Characteristic peaks for SWCNTs and MWCNTs are drawn as vertical dashed lines.

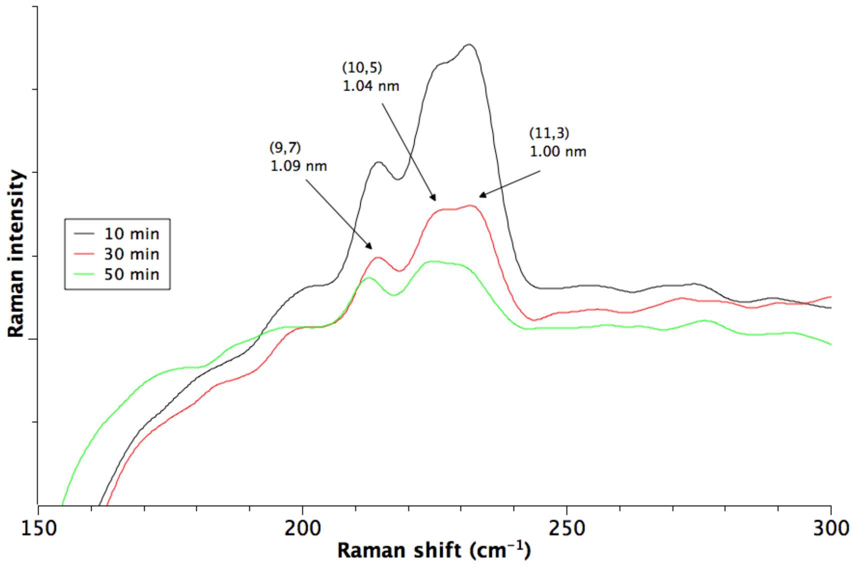

Figure 2.15: RBMs of Raman spectra of CNTs grown with varying annealing times. Several RBMs have been identified and labeled.

2.4.3.3 Switch from wet oxidation of Si chips to dry oxidation

In our early sample preparation protocol, we used 1 hr of wet oxidation at 1000 ºC try to thermally grow 500 nm of SiO_2 on top of our Si chips. To achieve wet oxidation, we bubbled compressed air through a water bubbler to increase the moisture content of the air that passed through the CVD furnace. We estimated the growth time of the SiO_2 layer based on the following equation:[43]

$$x = \sqrt{B(t+\tau)}$$

where B is the "parabolic rate constant" and τ accounts for the native oxide in the diffusion limited regime. For wet oxidation, $B = 0.287$ μm^2/hr and $\tau = 0$ hr at 1000 ºC.[43] Solving for x = 0.5 μm gives a growth time of 0.87 hr, and we chose a round 1 hr. However, when we compared the color of oxidized samples to a SiO_2 color chart for thermally grown silicon dioxide published by HTE Labs, the color of the oxidized chips was never correct.

Our suspicion was that our method for wet oxidizing was not getting sufficiently high moisture content in the air flowing over the samples. Dry oxidation is much slower, and the known growth parameters are $B = 0.0117$ μm^2/hr and $\tau = 0.37$ hr at 1000 ºC.[43] Solving for x = 0.5 μm gives a growth time of 21 hr. We dry oxidized a Si chip at 1000 ºC for 21 hr, and the sample came out with a pale blue-green, which is the color expected from a 502 nm thick oxide layer, based on the HTE Labs chart. A "wet" oxidized chip, a dry oxidized chip, and a chip that was not oxidized are shown in Figure 2.16.

Based on the HTE Labs color chart, the attempted "wet" oxidized chip should have approximately 50 nm of oxide, because of its tan color. 1 hr of dry oxidation should result in 16 μm of oxide, so our method of "wet" oxidation was only slightly successful at increasing the oxidation rate. Since the dry oxidation method was clearly more successful, all samples have been prepared with dry oxidation since this experiment.

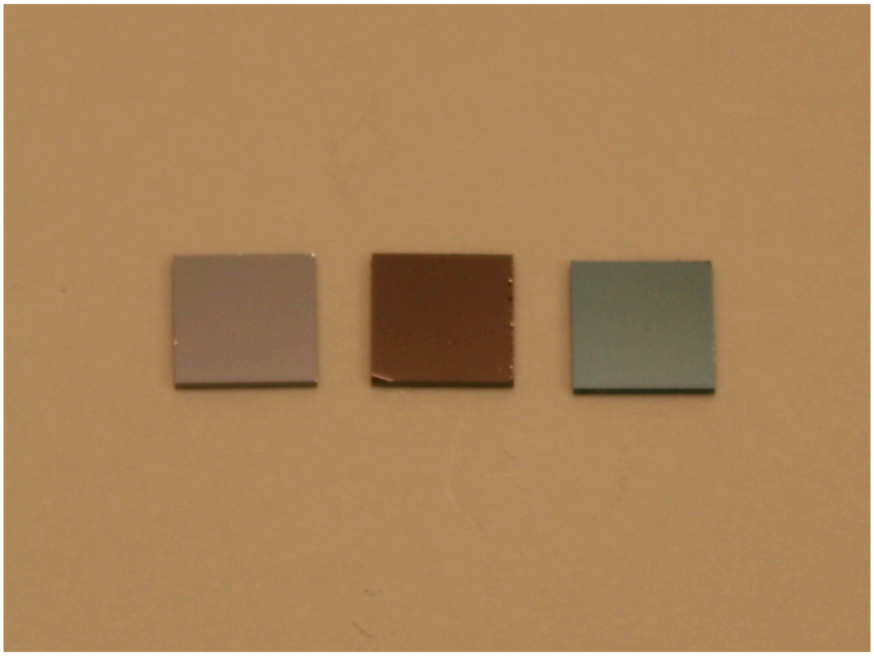

Figure 2.16: Comparison of 5 mm x 5 mm Si chips with different oxide thicknesses. The left chip was not oxidized, the center chip was "wet" oxidized for 1 hr, and the right chip was dry oxidized for 21 hr.

2.4.4 Hillocking

Early in the process of developing our CNT growth protocol, we noticed that the morphology of the growth substrate changes after annealing and CNT growth, as can be seen through the SWCNT growth in Figure 2.12. Even in samples that have denser CNT growth, those faceted structures can be seen at high magnification in the SEM. Figure 2.17 shows the post-annealing faceted structures more clearly, without any CNT growth. The roughened surface morphology is present across the entire sample, and the typical feature size is roughly 50-100 nm.

Despite occasional success in growing aligned CNTs, we were never able to consistently grow VA-CNTs, and we had a strong suspicion that the surface roughness post-annealing was responsible. While studying the effects of surface stress on microcantilevers (discussed in Chapter 4), we learned about hillock formation as a means of stress relief during the annealing of Al thin films.[44-50] When annealing Al films on SiO_2 substrates, the Al film develops a compressive stress because of its significantly higher thermal expansion coefficient.[45] Hillocking is a method of stress relief where protrusions form on the surface with a faceted pyramidal structure, exceeding the height of the thin film.[45,49] Thin passivating layers, such as native aluminum oxide or a thin Fe layer, develop flaws during the annealing process that allow the formation of a hillock as Al diffuses through the flaw to relieve stress.[49] The experimental conditions that lead to hillocking, and our observations of the substrates after annealing, match well with literature descriptions.

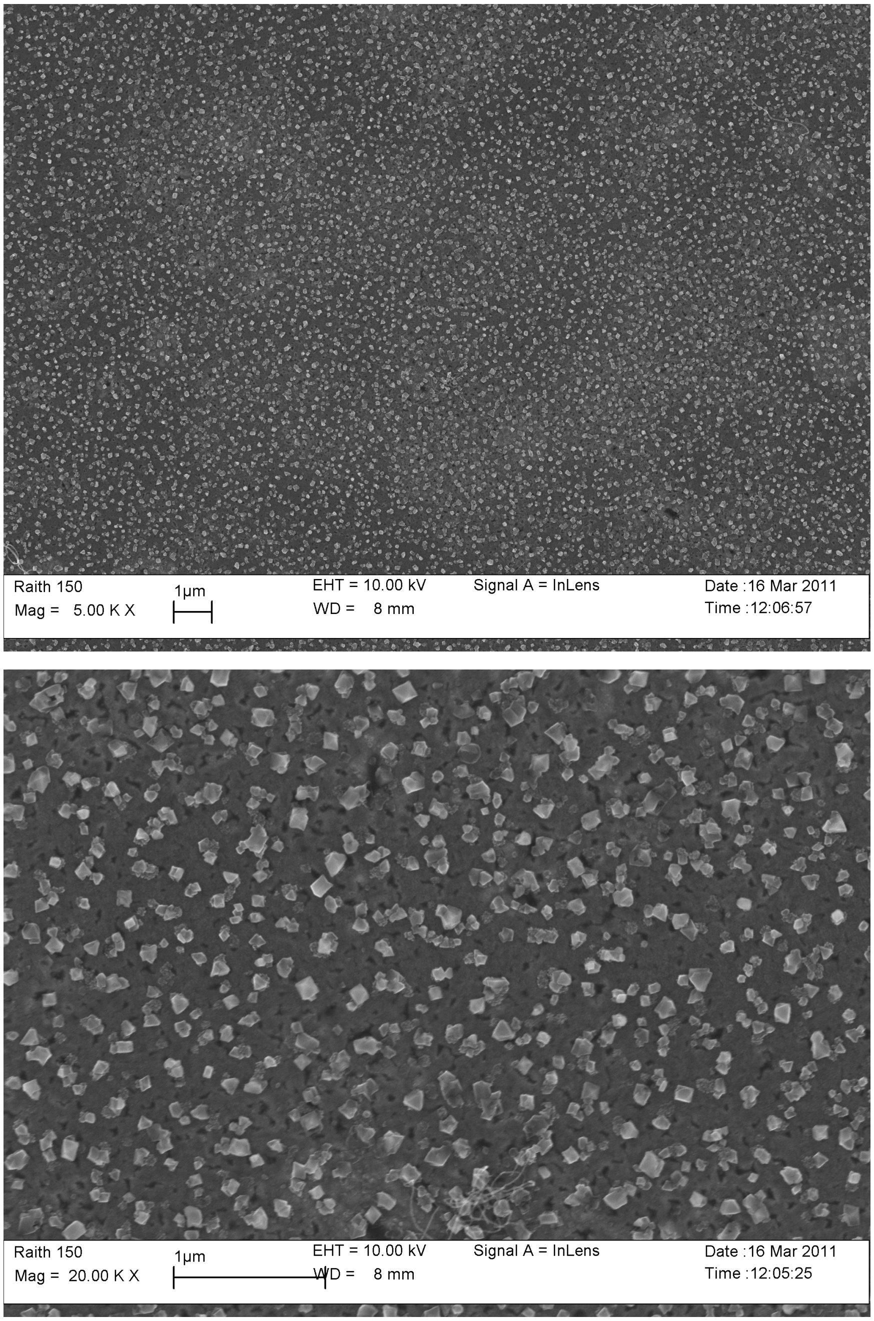

Figure 2.17: Growth substrate after annealing Al/Fe film. The top image shows the roughened surface over large areas, and the bottom image shows a zoomed in image of the faceted structures.

We wanted to eliminate this hillocking effect in order to reduce the surface stress (see Chapter 4) and to hopefully grow VA-CNTs. Unfortunately, the most common methods for stopping hillocking are thicker surface passivation or alloying with another metal, but neither of these methods is really appropriate for our system. To solve the problem, we purchased an Al_2O_3 source and switched to depositing Al_2O_3 as our catalyst support layer, rather than Al.

We deposit Al_2O_3 by e-beam evaporation of 2-4 mm Al_2O_3 pellets. To test the affect of annealing on the surface morphology, we deposited 20 nm Al_2O_3 and 40 nm Al_2O_3 onto two Si chips and annealed them using the sample protocol by which we grow CNTs. SEM images of the 40 nm film before and after annealing are shown in Figure 2.18. Note that the magnification is the same as shown in Figure 2.17, but no hillock structures have formed during the annealing process at 750 ºC. The images were taken at the edge of a place where the film had been fractured by handling with tweezers. Hillock structures do not form during annealing, the film looks extremely uniform, and the fractured edges still look sharp after annealing, indicating that the Al_2O_3 catalyst support layer is not affected by annealing.

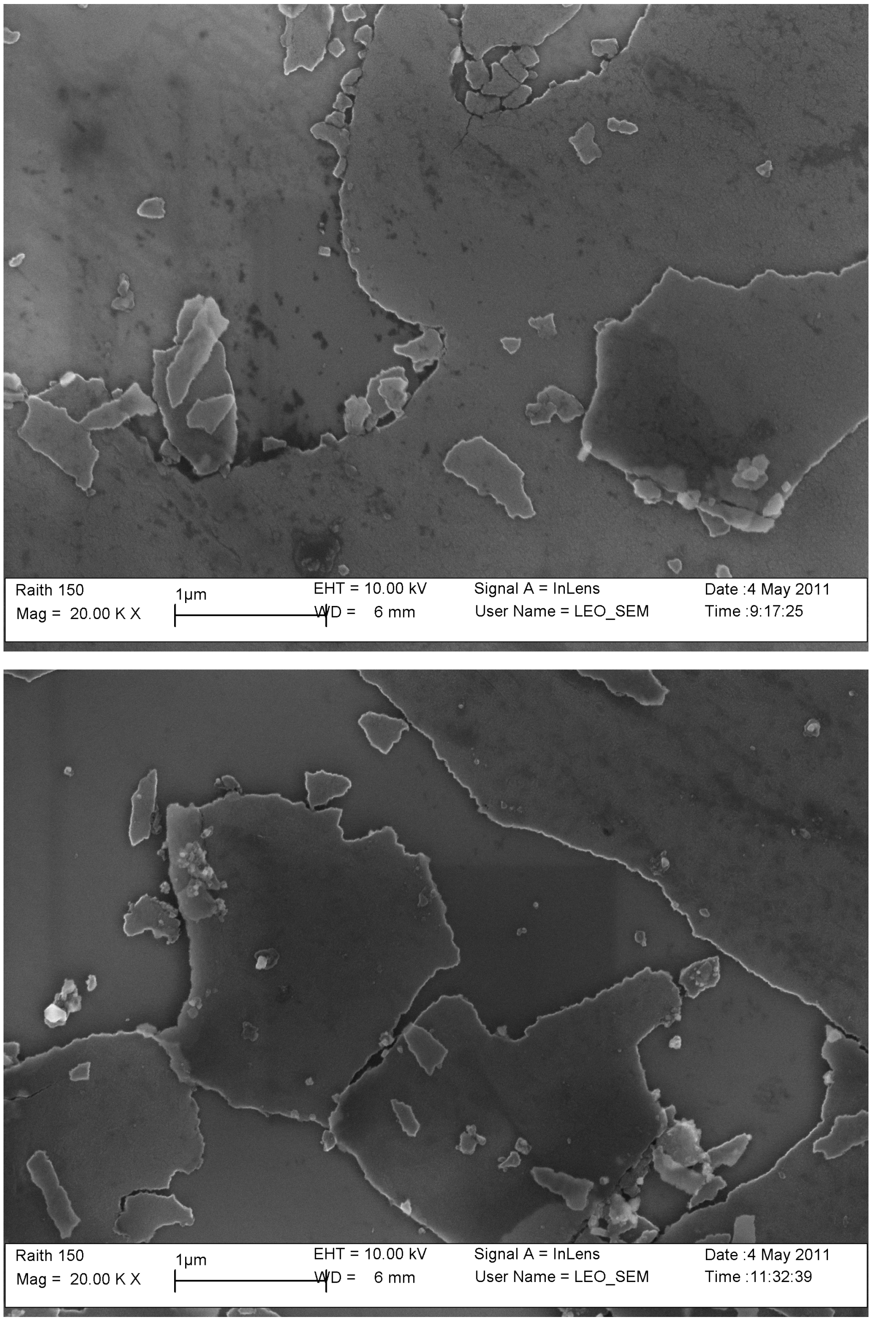

Figure 2.18: SEM images of a deposited Al_2O_3 film before (top) and after (bottom) annealing at 750 ºC.

2.4.5 Growth of VA-CNTs

After demonstrating that Al_2O_3 had no hillocking problems during annealing, 1 nm of Fe was deposited onto the two samples from the previous section and the samples were run through the CVD system to grow CNTs (100 sccm C_2H_4 flow was used to maximize CNT growth). As desired, we successfully grew VA-CNTs from these samples, as shown in Figure 2.19. The VA-CNT forest was ~20 μm tall and composed of a mixture of SWCNTs and MWCNTs, as determined by SEM and Raman spectroscopy, respectively.

2.4.5.1 Success of Mixed VA-SWCNTs/MWCNTs

With the success of our preliminary test, we tested several more samples, varying growth time and C_2H_4 flow rate. In the first set of experiments, we chose growth times of 2, 5, and 10 min, all using 100 sccm C_2H_4. After growing CNTs on the samples, it was visually apparent that the CNTs were vertically aligned, because samples with VA-CNTs have a uniform velvety black appearance, which is due to the strong optical absorption across the entire visible spectrum. Imaging with SEM showed that the 2 min sample had a ~4 μm tall VA-CNT forest (Figure 2.20), the 5 min sample had a ~10 μm VA-CNT forest (Figure 2.21), and the 10 min samples had a ~20 μm VA-CNT forest (Figure 2.22). These results show that the growth rate is approximately linear at 2 μm/min under these growth conditions. This growth rate likely saturates at longer growth times, but our goal is not to grow VA-CNT forests that are >20 μm, so we did not test any longer growth times. Raman spectroscopy showed that all three samples consisted of a mixture of SWCNTs and MWCNTs.

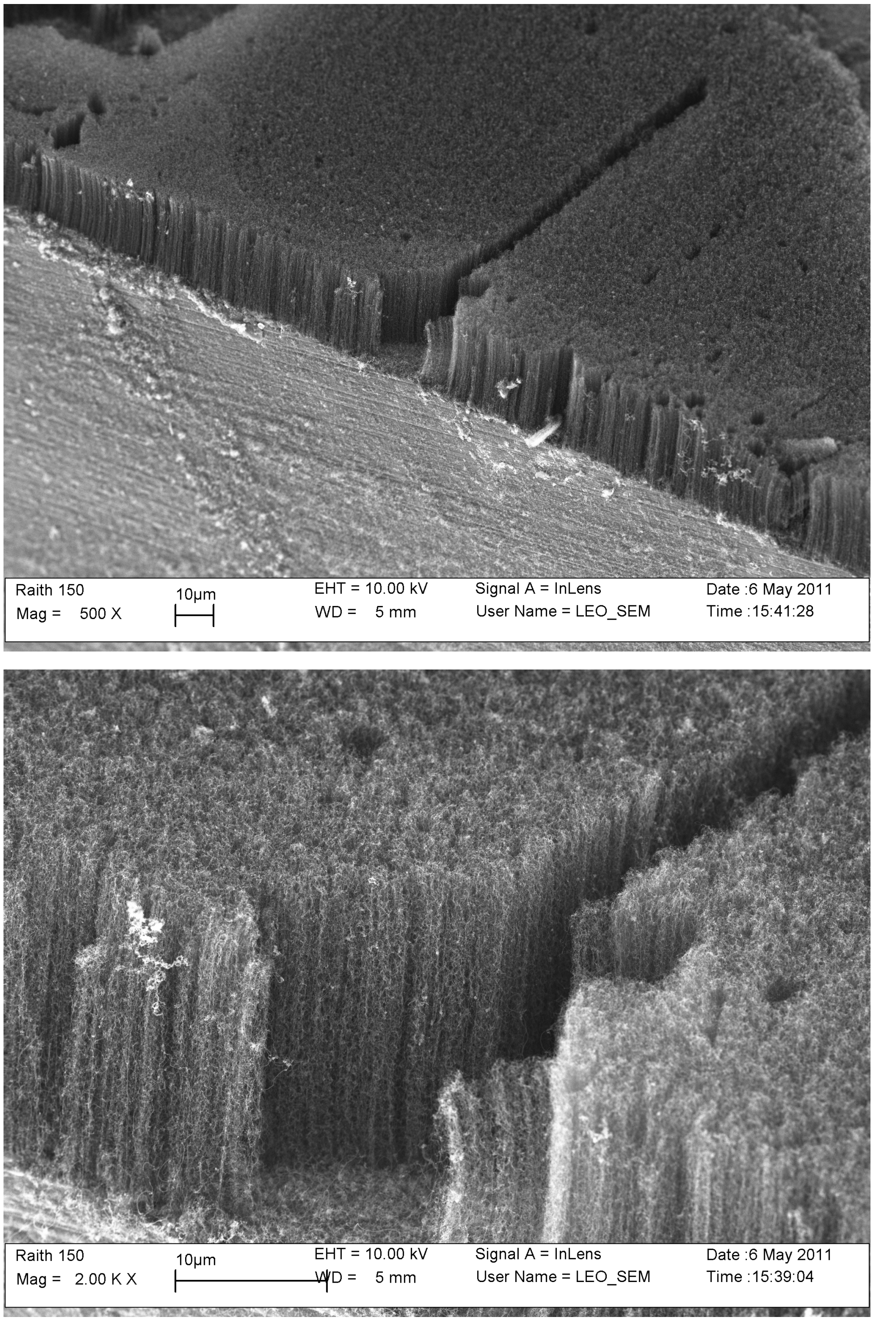

Figure 2.19: VA-CNTs grown using a 20 nm Al_2O_3 catalyst support layer.

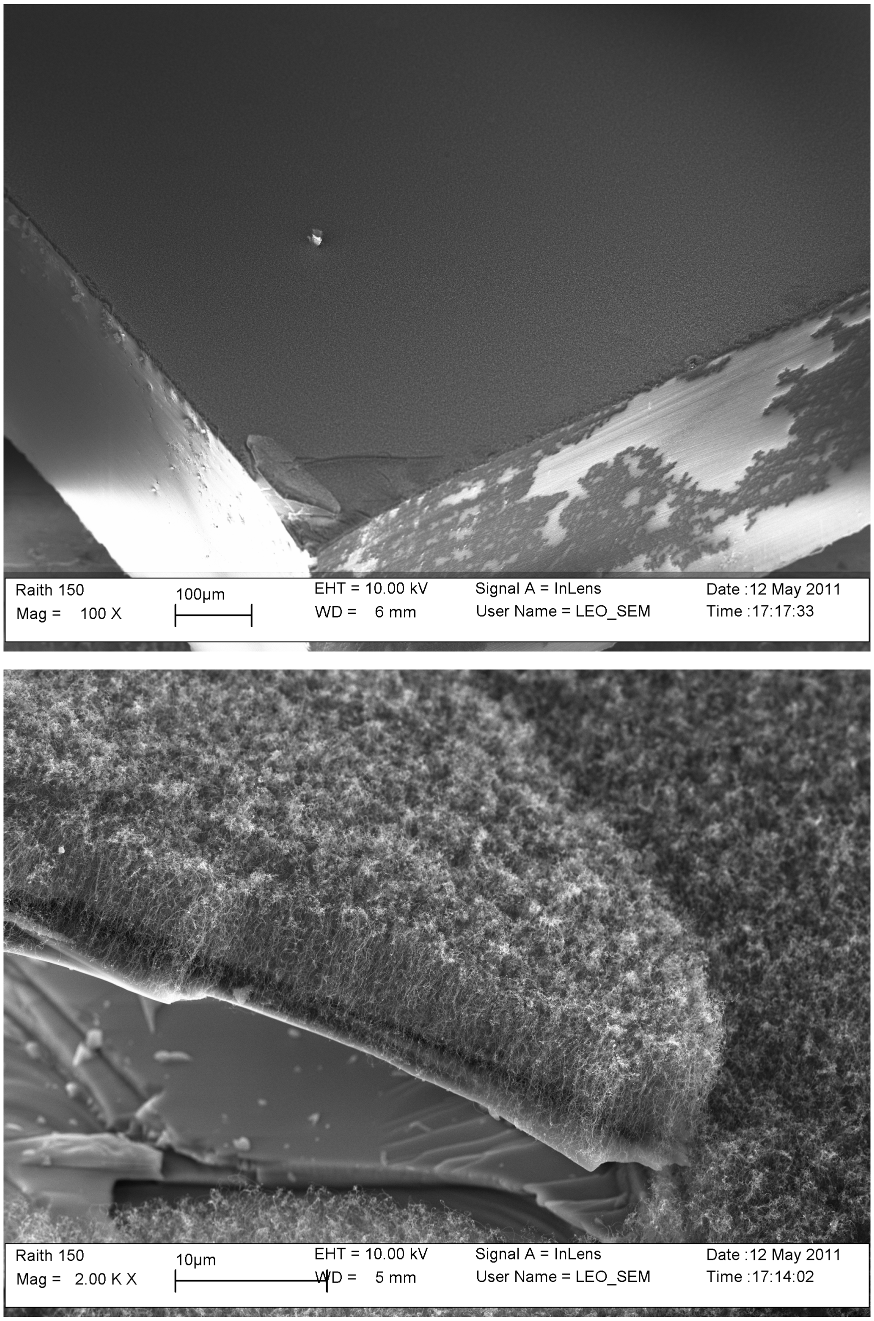

Figure 2.20: VA-CNTs grown in 2 min using Al_2O_3 catalyst support layer. The top image shows the growth uniformity over large areas, and the bottom image shows the aligned VA-CNT forest on a chipped piece near the corner.

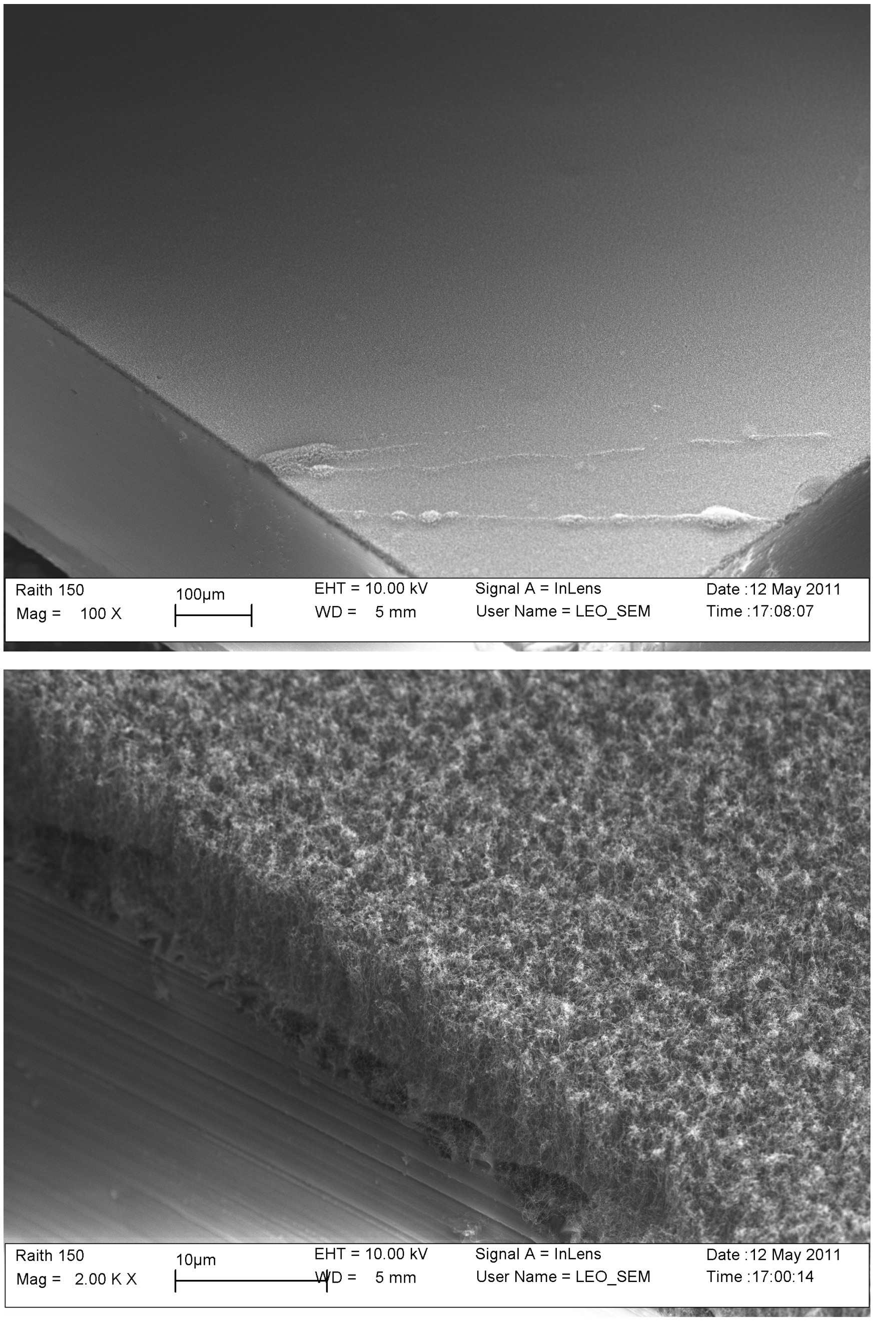

Figure 2.21: VA-CNTs grown in 5 min using Al_2O_3 catalyst support layer. The top image shows the growth uniformity over large areas, and the bottom image shows the aligned VA-CNT forest.

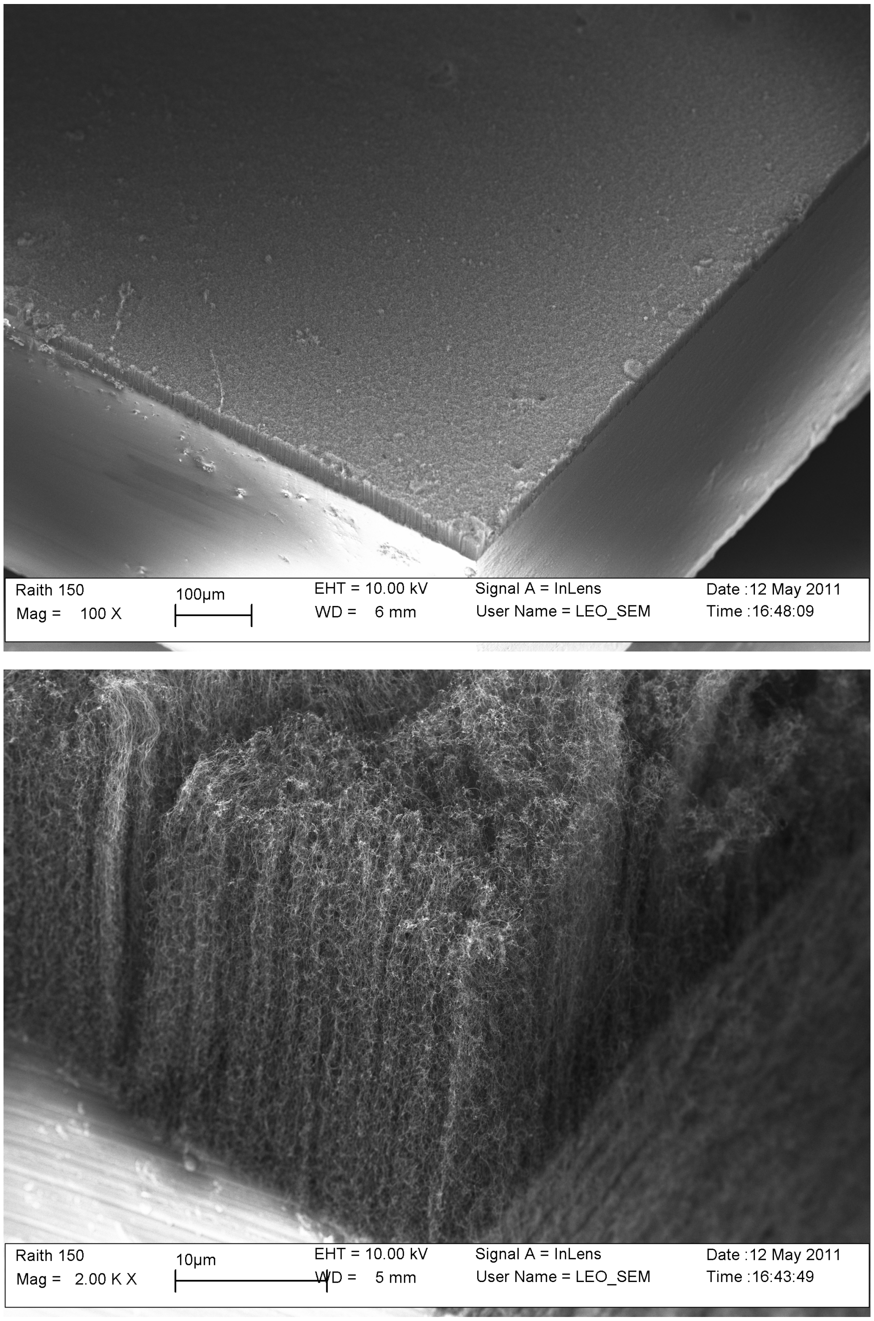

Figure 2.22: VA-CNTs grown in 10 min using Al_2O_3 catalyst support layer. The top image shows the growth uniformity over large areas, and the bottom image shows the aligned VA-CNT forest.

In the next set of experiments we varied the C_2H_4 flow in order to grow VA-SWCNTs instead of a mixture of VA-SWCNTs/MWCNTs. In these experiments, the growth protocol was exactly the same as for the sample shown in Figure 2.22, except that the C_2H_4 flow rate was held at 50 sccm or 20 sccm instead of 100 sccm. The CNT sample with 50 sccm C_2H_4 grew ~10 μm VA-CNTs, as shown in Figure 2.23. As with growth time, the relationship between the C_2H_4 flow and VA-CNT forest height appears to scale linearly. When we tested CNT growth with 20 sccm, we found that we were no longer able to grow VA-CNTs, as shown in Figure 2.24. The growth was still quite dense and uniform, but there was no visible alignment. Raman spectra showed that both of these samples still had a mixture of SWCNTs and MWCNTs, but the 20 sccm sample showed stronger SWCNT character in the G-band and had more pronounced RBMs.

2.4.5.2 Current Limitations & Future Work

We currently are able to grow VA-CNT forests that are composed of either VA-MWCNTs or a mixture VA-SWCNTs/MWCNTs. For the current needs of the actuator project, this growth capability is sufficient (see Chapter 4). In future generations of the actuator project, we will want to more carefully explore the CNT growth parameter space to get highly aligned SWCNTs. In addition, growing SWCNTs with well defined lengths will be significant for several other developing projects in the Poler research group.

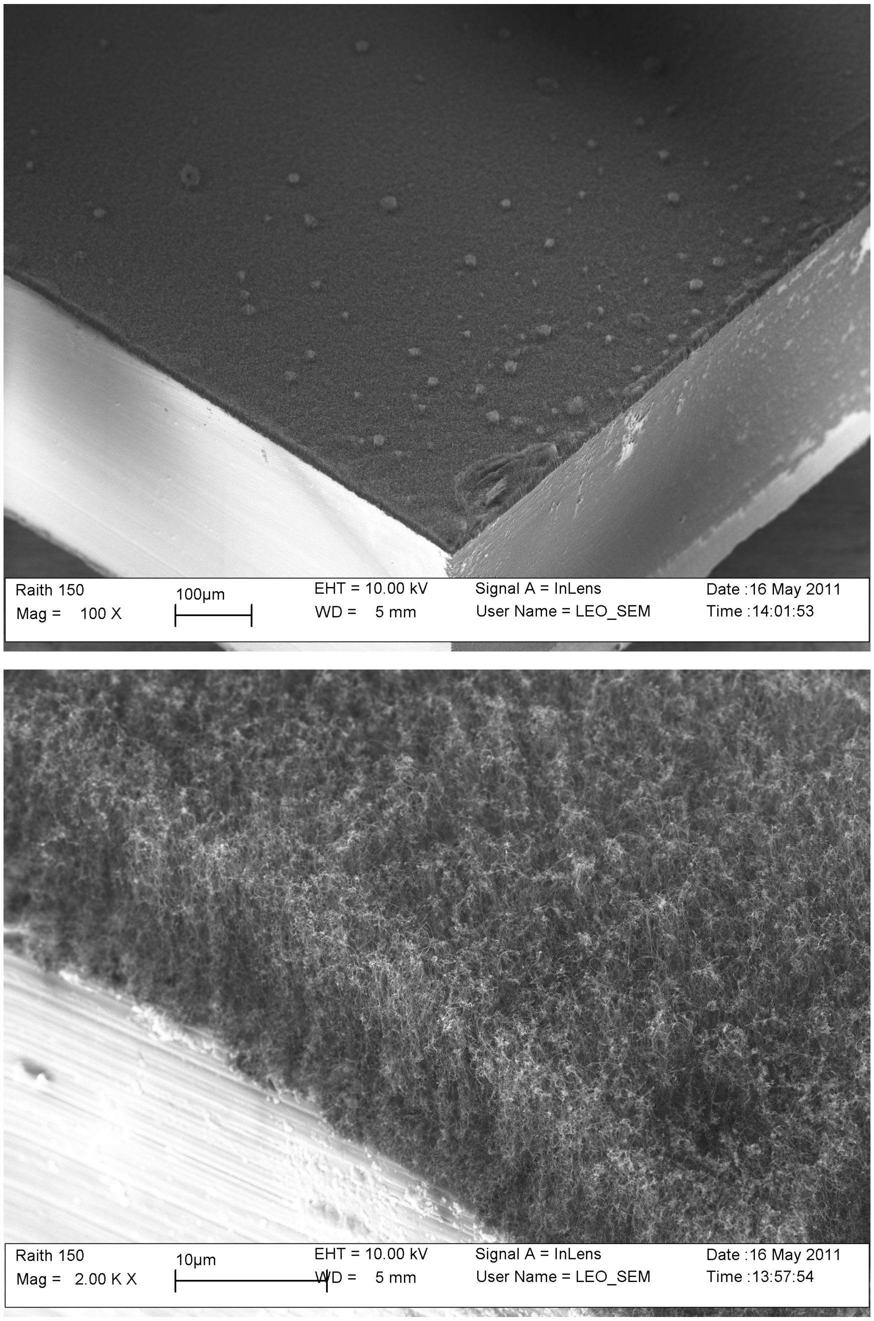

Figure 2.23: VA-CNTs grown in 10 min with 50 sccm C_2H_4 flow. The top image shows uniform growth, with a few tufts of taller growth, and the bottom image shows the aligned VA-CNT forest.

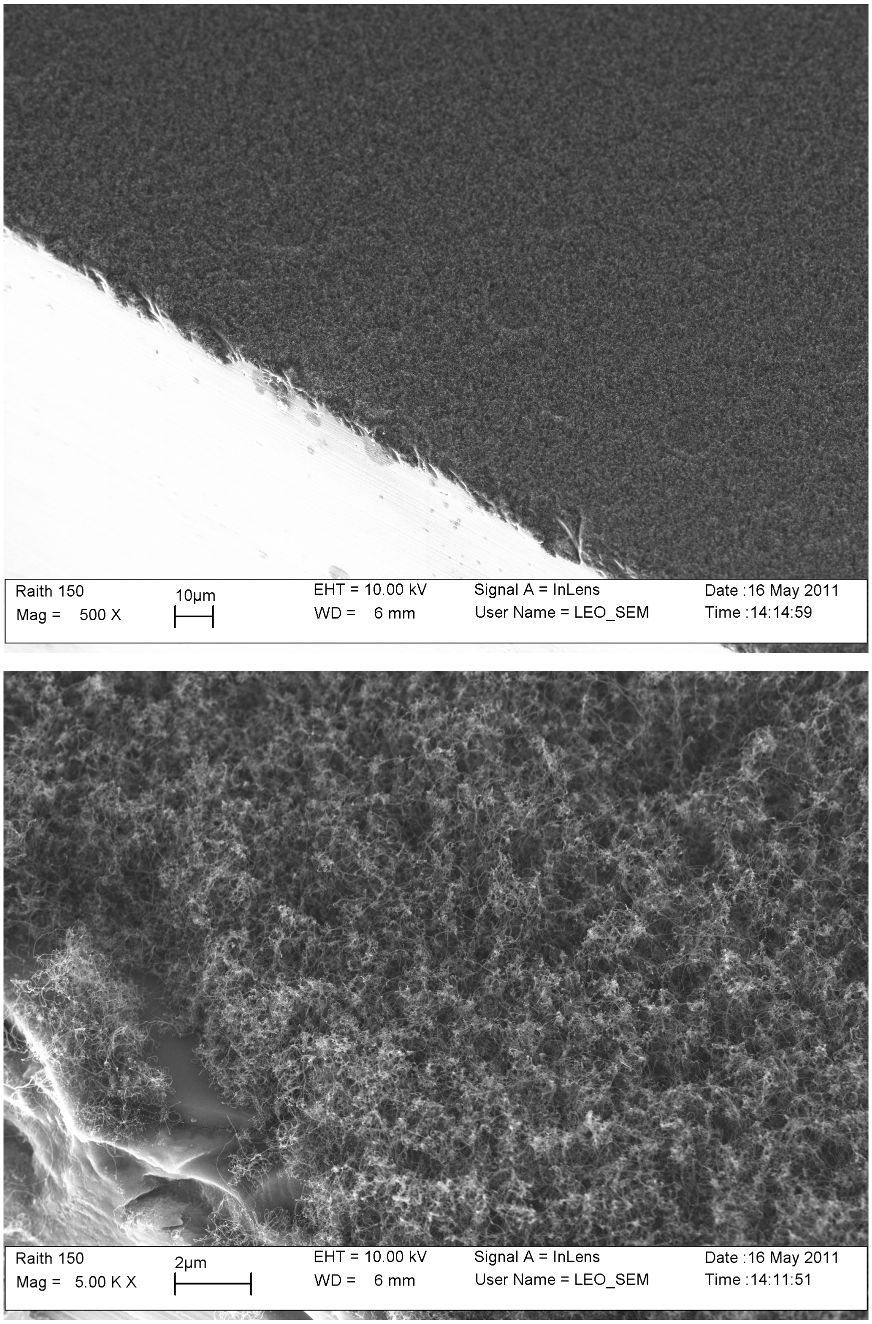

Figure 2.24: CNTs grown in 10 min with 20 sccm C_2H_4 flow. The top image shows uniform randomly-aligned growth, and the bottom image shows the unaligned CNTs at the edge of the chip.

CHAPTER 3: DISPERSION AND AGGREGATION OF CARBON NANOTUBES

3.1 Dispersion of Carbon Nanotubes

Dispersing CNTs in liquids is important for many reasons. When CNTs are grown by any of the methods described above, they are always solid state and bundled together due to π-π stacking. Whether one purchases CNTs in powder form or grows them, it is necessary to disperse them in a liquid to process them. CNTs are not easily dispersed due to their strong tube-tube interactions and their length (hundreds of nanometers or microns).

Ultrasonication is the most common method used to de-bundle CNTs, allowing them to be dispersed in a solvent. Depending on one's needs, three different types of ultrasonicators are used: bath, tip, and cup-horn ultrasonicators. Bath ultrasonication is the gentlest form of ultrasonication and does not cause many sidewall defects, but tip or cup-horn ultrasonicators can be used for more forceful de-bundling of the CNTs. Ultrasonication can shorten CNTs or damage the sidewalls, so ultrasonication power and time must chosen carefully. Furthermore, solvents respond differently to ultrasonication power and time, which can affect dispersion quality and stability.

3.1.1 Aqueous Dispersions

CNTs are completely insoluble in water when pristine. CNTs must be modified through acid treatment, a surfactant coating, or covalent functionalization if they are to be dispersed into water. Surfactants such as sodium dodecyl sulfate (SDS),[25,51-54] Triton X-100,[25,54-58] or sodium dodecylbenzene sulfonate (SDBS)[25,51,54,59,60] are used most frequently. However, other surfactants have also been explored, such as Gum Arabic,[61] 4-(10-hydroxy)decyl benzoate,[62] trimethyl-(2-oxo-2-pyren-1-yl-ethyl)-ammonium bromide,[63] PmPV-based polymer,[64] or even single-stranded DNA.[65]

Typical preparation methods use deionized water or D_2O with 1% surfactant, by weight.[53] However, lower surfactant concentrations can still exfoliate and de-bundle CNTs sufficiently. An alternative method to the 1% by weight method is a gradual addition of surfactant at intervals during ultrasonication.[59] There is some evidence that the gradual addition method may do a better job of dispersing individual tubes without a large excess of surfactant left in solution. Once a surfactant solution has been prepared, powdered CNTs are added and one of the ultrasonication methods is used to facilitate the de-bundling process.

An alternative to using surfactants is covalent functionalization of the CNT sidewalls. Many types of covalent functionalization have been employed, including amidation, thiolation, halogenation, bromination, esterification, chlorination, fluorination, and hydrogenation.[66] Covalent sidewall functionalization will significantly affect the electronic and mechanical properties because the change from sp^2 to sp^3 hybridization causes irregularities in the hexagonal lattice.[66] Consequently, this approach to CNT dispersion is not acceptable when studying properties of pristine CNTs.

The last major method used to render CNTs dispersible in water is acid treatment. Acid treatments severely damage the integrity of the CNT sidewalls by causing many defect sites. Moreover, when the acid/CNT mixture is ultrasonicated, CNTs will be cut at those defect sites due to the collapse of ultrasonication-induced cavitation bubbles.[56] Acid treatment is an effective way to make CNTs dispersible or rapidly reduce the mean length of a CNT dispersion, but should be avoided if features of pristine CNTs need to be studied.

3.1.2 Non-Aqueous Dispersions

To study the properties of pristine CNTs, non-aqueous solvents must be used since they do not require any type of surfactant, defect creation, or covalent functionalization, all of which modify CNT properties.[67] As with aqueous dispersions, sonication is used to disperse CNTs in non-aqueous solvents. A wide variety of non-aqueous solvents have been tested and the concentration of CNTs that can be dispersed in each solvent varies significantly.[67-69] We work primarily with several of the polar aprotic solvents, which can disperse more CNTs than most other non-aqueous solvents.[67,69,70] Specifically, we use DMF, DMA, and NMP. These solvents are good at dispersing CNTs for several reasons. There is a strong correlation between high electron pair donicity and the ability to produce good dispersions.[67] Another important solvent property is a low ability to hydrogen bond.[67] A high value of the solvochromatic parameter is also key to high dispersion limits.[67] DMF, DMA, and NMP all meet these criteria. Other significant parameters are Hansen parameters, the Hildebrand parameter, and solvent surface energy.[71,72]

3.2 Aggregation of Single-Walled Carbon Nanotubes

Given the size and shape of CNTs, it is appropriate to consider them as a colloidal system when dispersed[73] rather than a solute. The significance of this distinction is most apparent when considering the aggregation behavior of CNTs in response to ionic species.[10,73,74] Increasing the ionic strength in a CNT dispersion leads to collapse of the electrical double layer (EDL) that is central to DLVO theory.[75,76] In DLVO theory, EDL repulsion counteracts the van der Waals attraction between particles in solution.[77] The EDL forms in electrolytic solutions as solvated ions associate with surface charge on dispersed colloids. The interaction potential between two identical spheres is represented as[77]

$$V(h) = \pi R\left\{ -\frac{H_{121}}{12\pi}\frac{1}{h} + \frac{64 k_B T c_o \Gamma_0^2}{\kappa^2}\exp(-\kappa h) \right\}$$

which describes the potential of interaction, $V(h)$, as a function of the separation, h, and the Debye screening length, κ^{-1}.

From that equation and several assumptions, the critical coagulation concentration, where the dispersion undergoes fast diffusion limited aggregation, can be approximated by[77]

$$CCC \approx 1\times 10^5 \frac{\left(\varepsilon_r \varepsilon_0\right)^3 \left(k_B T\right)^5}{z^6 e^6 H_{121}^2}\Gamma_0^4$$

where the dielectric constant, ε_r, and the Hamaker constant, H_{121}, of the solvents are the key parameters when comparing dispersion stability of nanoparticles in those solvents. The interaction potential between dispersed nanoparticles is shown in Figure 3.1 for three cases; ionic strength below the CCC, at the CCC, and above the CCC. When below the CCC, the potential barrier from EDL repulsion prevents nanoparticles from aggregating ($V_{\max} > 0$). Increasing the ionic strength of the dispersant reduces that potential barrier by collapsing the EDL, as described above, and induces aggregation at or above the CCC ($V_{\max} \leq 0$). Regardless of the ionic strength, the thermodynamically stable state is when the CNTs fall into the primary minimum of the interaction potential, as illustrated in Figure 3.1.

Describing the colloidal behavior of nanoparticles like CNTs with DLVO is important when studying their aggregation in response to inorganic salts, ionic coordinating complexes, or other species in solution. Nevertheless, it is important to recognize the assumptions implicit in the equations presented above and whether those assumptions are appropriate for CNTs. Those equations were derived for the interaction of two rigid spherical particles, whereas CNTs are flexible rods with exteremly high aspect ratios. Further, when linearizing the electrostatics to get the Γ_0 function, which is described further in Section 3.5.3.1, the Debye-Huckle approximation requires particles to have a ζ-potential under 25 mV,[74] but experiment results[78-80] show that this assumption is not necessarily true for CNTs. Despite these limitations, DLVO has provided a framework to successfully describe the aggregation behavior of CNTs under various experimental conditions.[73,74,81-87]

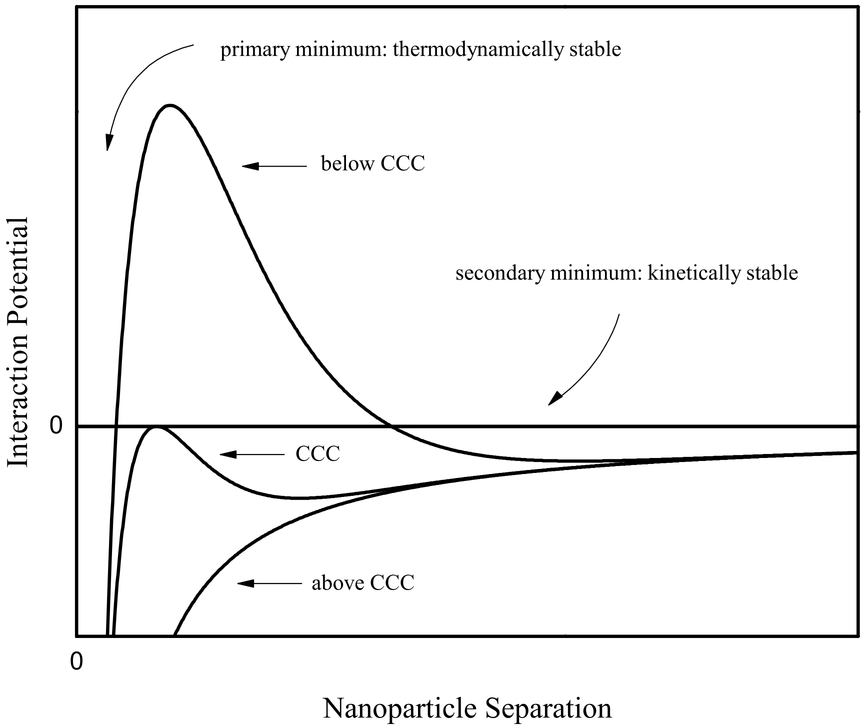

Figure 3.1: Plot of the interaction potential between two dispersed nanoparticles below the CCC, at the CCC, and above the CCC.

3.3 Challenges When Dispersing Single-Walled Carbon Nanotubes

Dispersing SWCNTs by ultrasonication is relatively straightforward, however, there are several issues that must be considered. When a dispersion of SWCNTs is formed, the ideal result is that all SWCNTs have been debundled and are no longer bound to any other SWCNTs. In reality, this never happens because the ultrasonication time is finite. It is also possible that the dispersion limit has been exceeded for the given solvent and no more SWCNTs can be dispersed.

To get a good and clean dispersion, it is necessary to remove any aggregated material or debris that has been introduced into the sample. There are generally two approaches used to remove any undispersed material: filtration or ultracentrifugation. Filtration has the advantage of being a fast method and it works reasonably well. Ultracentrifugation is cleaner and provides greater control over the process, but is much slower than filtration. If SWCNTs have been dispersed into water with surfactants, the samples can be ultracentrifuged for several hours at fields over 100,000 g to ensure that only individually dispersed SWCNTs or very small bundles remain.[53] Ultracentrifugation must be used carefully when working with non-aqueous solvents, because the dispersions are less kinetically stable than dispersions aided by surfactants. Fields that are too high or extended ultracentrifugation times will remove all SWCNTs from dispersion. Reasonable fields and times for dispersions in NMP, DMF, or DMA are 20,000 g for 20 min.

Another consideration when using high power tip ultrasonication is the potential for sonochemically generated byproducts. This phenomenon was discovered in our lab and published.[10] I determined that the sample temperature and presence of oxygen dramatically affect SWCNT dispersability due to the formation of an unwanted sonochemically byproduct, methyl hydroperoxide, in some polar aprotic solvents like NMP, DMF, and DMA.

3.4 Production of Methyl Hydroperoxide and its Effect on Dispersion Stability

3.4.1 Introduction

Sample preparation and solvent choice are quite important when handling nanomaterials. A wide variety of organic solvents are used to disperse pristine SWCNTs,[67-69,88] though amide solvents tend to be among the most successful.[69,88,89] *N,N*-Dimethylformamide (DMF) and *N*-methyl-2-pyrrolidinone (NMP) are two of the most frequently used organic solvents for dispersing SWCNTs; the experimental results focus on DMF. In addition to DMF and NMP, we also report on two other polar aprotic solvents: *N,N*-Dimethylacetamide (DMA) and acetonitrile (MeCN).

It has been observed that two parameters during ultrasonication can significantly affect SWCNT dispersion stability in several polar aprotic solvents: (1) oxygen concentration in the dispersant and (2) sample temperature during ultrasonication. Increasing the oxygen concentration during ice bath cooled (IB) ultrasonication (~20 ºC) reduces dispersion stability and decreasing oxygen concentration enhances dispersion stability. Hot ultrasonication (~110 ºC) yields stable dispersions, regardless of the oxygen concentration. It has been determined that the source of dispersion instability is a sonochemically generated byproduct, methyl hydroperoxide. These results were published in JACS: Forney, M. W.; Poler, J. C. *J. Am. Chem. Soc.* **2010**, 132, 791.[10]

3.4.2 Experimental

N,N-Dimethylformamide (Fisher, Spectranalyzed), *N*-methyl-2-pyrrolidinone (OmniSolv, Spectrophotometry & Gas Chromatography), *N,N*-Dimethylacetamide (Alfa Aesar, 99%), and acetonitrile (Burdick & Jackson, HPLC, anhydrous) were used as purchased. Deionized water was also Millipore filtered to 16 MΩcm (referred to as "DI water"). Dispersions and pure solvents were ultrasonicated with a power of 10 W RMS (yielding an average power density of 0.4-0.5 W/cm^3, depending on sample size).

Fluorescence measurements were taken with a HORIBA Jobin Yvon Fluorolog 2. The tip ultrasonicator was positioned over the fluorometer, with the tip inserted into a sample cuvette containing DMF and 100 μM Lucigenin (Alexis Biochemicals). All emission was due to sonochemiluminescence, as there was no optical excitation of the solution. A Cary 5000 UV-Vis-NIR spectrometer was used to measure optical absorption for concentrations of SWCNTs and triiodide. IR spectra were taken with a Nexus 870 FT-IR E.S.P. NMR spectra, for determination of water concentrations in DMF, were taken with a JEOL ECX-300.

A Thermo Finnigan Trace GC-MS with Xcalibur software was used to measure oxygen concentrations in DMF. Relative oxygen concentrations were determined by integrating the peak area for $m/z = 31.5 - 32.5$. As a control study, Ar was used to deaerate a sample and no O_2 peak was observed by GC-MS. The GC-MS was also used to detect the formation of ethane during low temperature ultrasonication of deaerated DMF samples.

"Ice bath" ("IB") ultrasonications were temperature regulated by submerging the sample vial in an ice bath during ultrasonication, which ensured that the average sample temperature was approximately 20 ºC. "Hot" ultrasonications were not temperature regulated, and reached an equilibrium temperature of approximately 110 ºC.

Most samples were prepared with a Fisher Scientific Sonic Dismembrator 60 (⅛" tip ultrasonicator). Dispersions were made by adding ~0.5 mg HiPCO SWCNTs (Grade P CNT, now Unidym) to the dispersants and ultrasonicated under various conditions. We monitored the dispersion stability as a function of ultrasonication time by removing 1 mL aliquots every 20 minutes. After ultrasonication, the aliquots were allowed to sit undisturbed for two days so that any undispersed SWCNTs would aggregate. Each aliquot was then centrifuged at 1000 g for 10 minutes in a Fisher Scientific Micro7 tabletop centrifuge to sediment any aggregated SWCNTs. 100 μL of the supernatant was immediately transferred to a cuvette to measure the SWCNT concentration based on the optical absorption.[68]

The presence of methyl hydroperoxide was detected by oxidizing iodide ions to triiodide. We measured the concentration of triiodide produced by adding KI to a 2 hour IB+O_2 ultrasonicated DMF sample. KI was dissolved in the sample to give an I^- concentration of 10^{-2} M (ensuring that the I^- concentration would be far in excess of the anticipated and measured I_3^- concentration of ~10^{-4} M). Methyl hydroperoxide as a function of ultrasonication time were measured by titration, using a NaOH titrant and bromothymol blue (BTB) as the indicator. The endpoint was reached when the solution was the same shade of green as a reference sample, which had the same concentration of BTB in fresh DMF. When measuring the concentration as a function of ultrasonication time, 1 mL aliquots were removed every 20 minutes during ultrasonication of a sample and tested. Generation of methyl hydroperoxide was independent of the SWCNT concentration.

Oxygen rich samples were prepared by bubbling pure oxygen through the samples for a minimum of 15 minutes before ultrasonication. Deaerated samples were prepared by bubbling pure argon through the samples for a minimum of 15 minutes. In both cases, the gas flow rate was kept low to prevent unnecessary solvent evaporation during ultrasonication. This was especially important at high temperatures, because excessive gas flow was observed to cause atomization of the solvent, leading to rapid solvent loss.

3.4.3 Discussion and Results

Anomalous dispersion instability was first observed when attempting to maximize the number of individually dispersed SWCNTs in DMF by tip ultrasonicating samples for 2 hours while keeping the sample cool with an ice bath ("IB"). Visible aggregates formed within seconds or minutes and the dispersion collapsed overnight. In contrast, dispersions formed by tip ultrasonicating for 30 mins without an ice bath ("Hot") can be stable for months with no visible aggregation, as shown in Figure 3.2. Figure 3.3 displays the effect of various ultrasonication conditions on SWCNT dispersion stability. The source of the observed dispersion instability was not obvious and required demonstrating that several reasonable possibilities were not occurring. This dissertation addresses the source of dispersion instability, methyl hydroperoxide, and the mechanism by which it is formed.

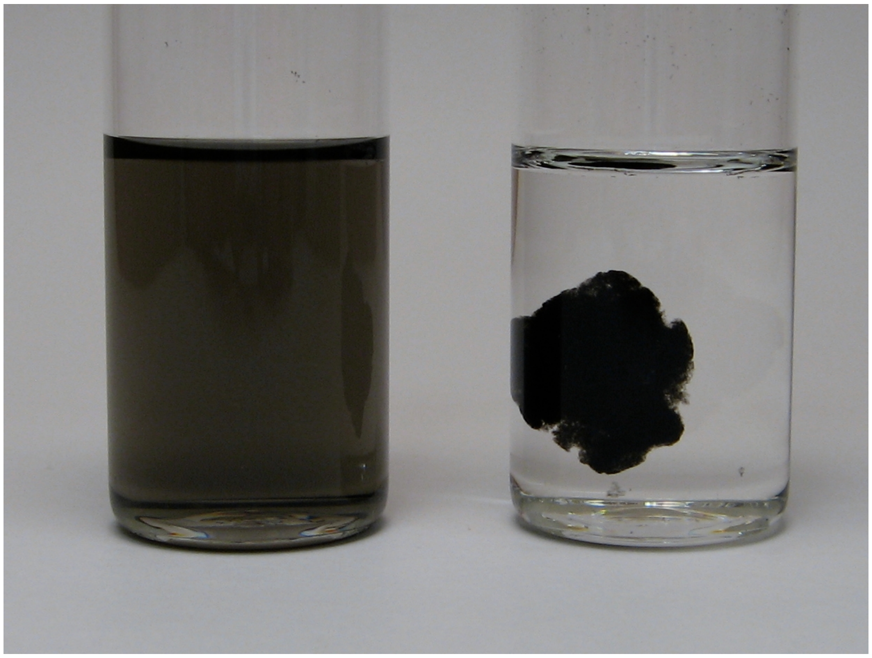

Figure 3.2: Comparison of samples prepared with two different dispersion protocols. The dispersion on the left was ultrasonicated for 2 hours without being cooled by an ice bath. The sample on the right was ultrasonicated for 2 hours with an oxygen sparge and kept at ~20 ºC by an ice bath.

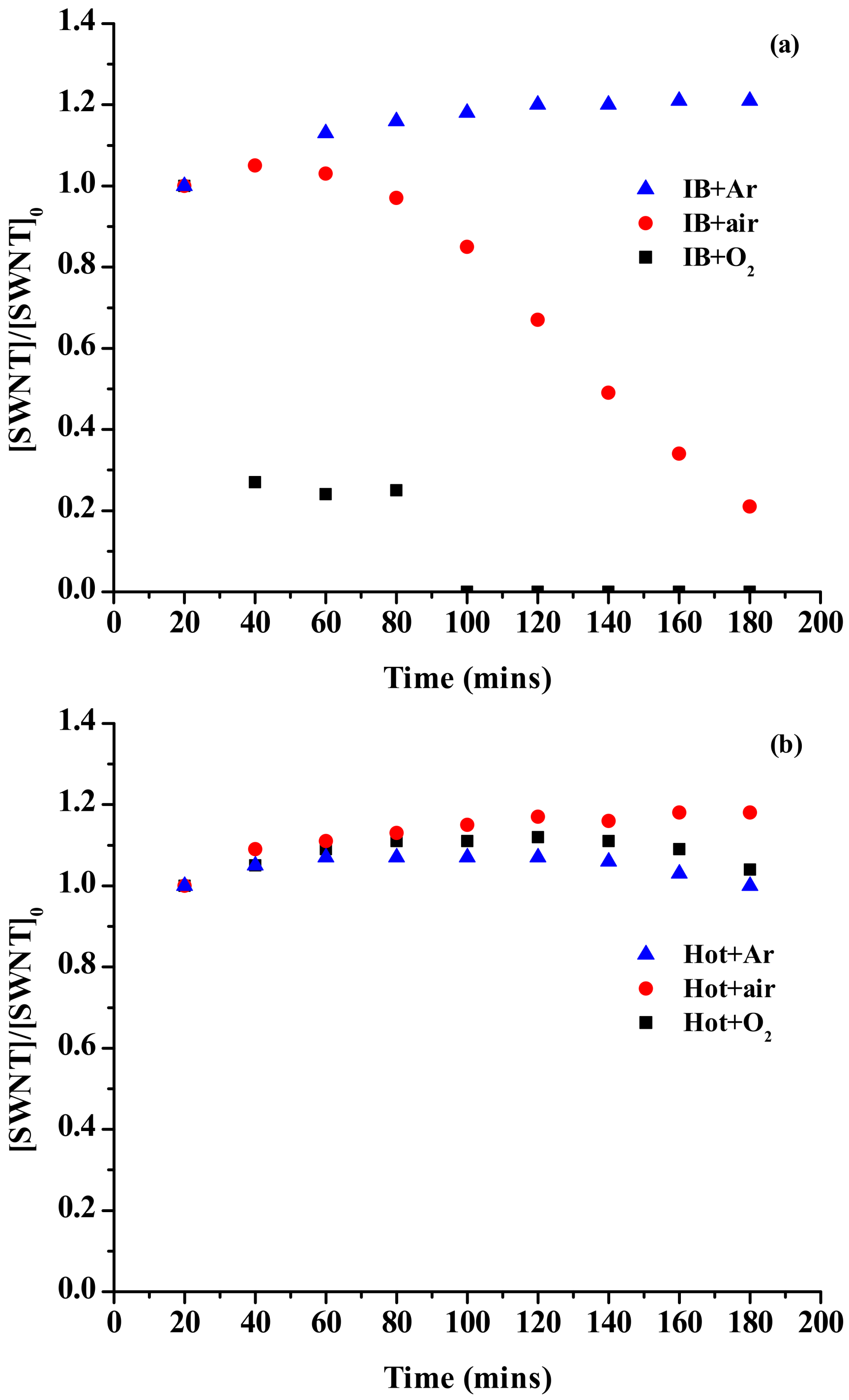

Figure 3.3: SWCNT concentration as a function of ultrasonication time under various conditions. (a) Dispersion stability for IB samples, normalized to the [SWCNT] at 20 min. (b) Dispersion stability for Hot samples.

It is known that radicals are produced during ultrasonication of DMF.[90-92] Moreover, cross-linking of bundled SWCNTs can result from UV-induced free radical formation.[93] Therefore, it is hypothesized that the lower temperature may be extending radical lifetimes to the point where they are cross-linking SWCNTs during ultrasonication. We were able to detect radical production by ultrasonication of DMF through the sonochemiluminescence of lucigenin as reported by Wang, *et al.*[92] The lucigenin emission spectrum we observed was similar to theirs (see Figure 3.4a). As shown in Figure 3.4b, we monitored the luminescence emission peak (410 nm) while turning the ultrasonicator on and off. No luminescence was observed when the ultrasonicator was off, but strong luminescence appeared as soon as the ultrasonicator was turned on. Our observations are consistent with Wang, *et al.*,[92] that the sonochemiluminescence is due to the reaction of Lucigenin with free radicals produced during ultrasonication. As indicated by Misik, *et al.*,[94] methyl radicals should be more reactive than the corresponding nitrogen centered radicals and we expect them to dominate any radical reactions that occur during ultrasonication.

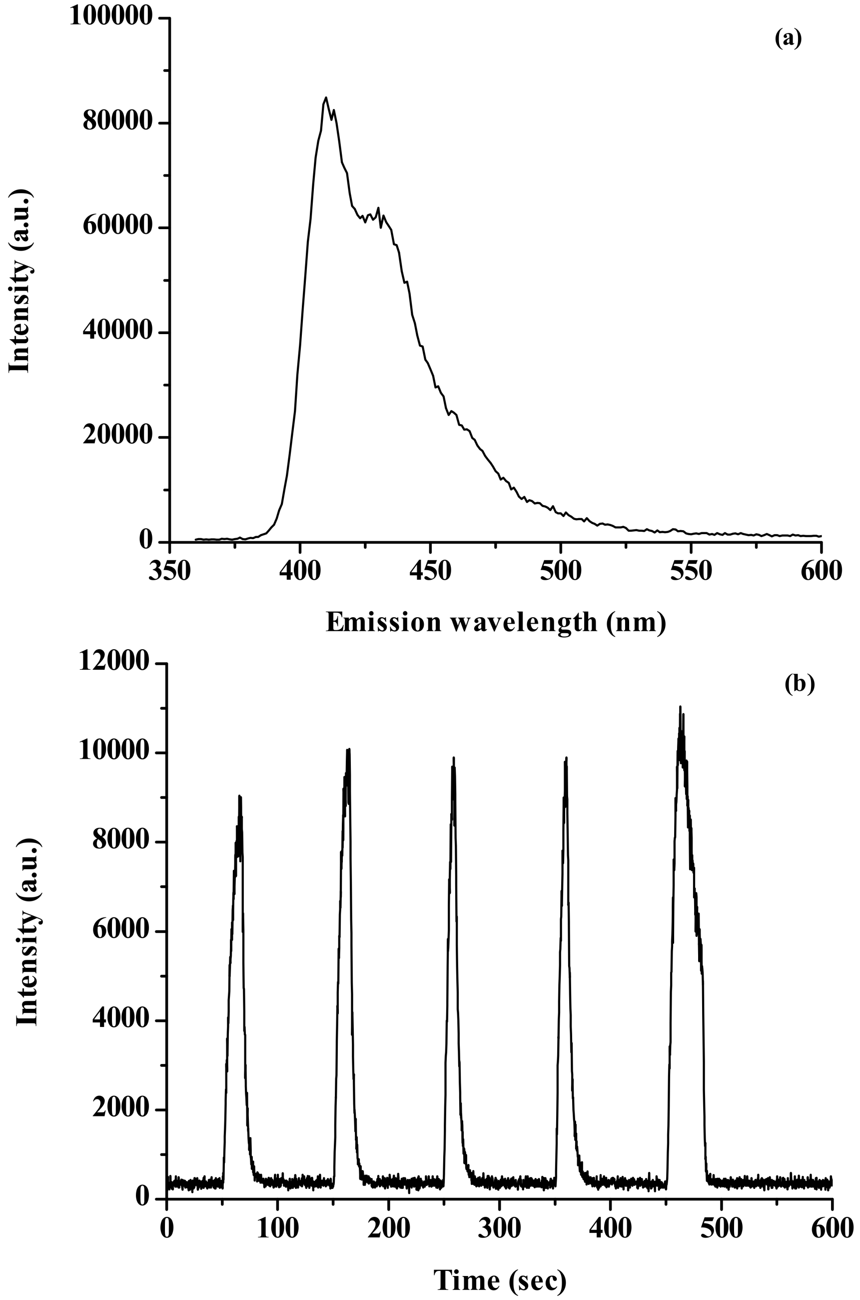

Figure 3.4: Sonochemiluminescence emission from lucigenin in DMF. Shown in (a) is the emission profile of lucigenin during ultrasonication. In (b), the sonochemiluminescence intensity at the emission peak (410 nm) is monitored as a function of time. The ultrasonicator was turned on for 10-15 seconds at 50 sec, 150 sec, 250 sec, and 350 sec. At 450 sec, the ultrasonicator was turned on for 1 min to see at what intensity the sonochemiluminescence would saturate.

Wang, *et al.*[92] used various natural flavonoids to suppress sonochemiluminescence of lucigenin by scavenging the free radicals generated by ultrasonication. We successfully used Morin, one of the more efficient radical scavenging flavonoids, to quench the sonochemiluminescence and to stop the rapid aggregation observed after low temperature ultrasonication. Interestingly, we found that Morin also acts as a surfactant capable of dispersing SWCNTs into water. Consequently, the enhanced dispersion stability may have been due to Morin's surfactant ability, free radical scavenging, or a combination of the two.

If SWCNTs were cross-linked through radical initiation, they would exhibit modified electronic, optical, and vibrational properties due to disruption of their otherwise uniform sp^2 bonded structure. Raman spectra of SWCNTs ultrasonicated under various ultrasonication protocols were extensively studied. The D/G^+ band ratio and the width of the G' overtone band were compared in the Raman spectra. Point defects due to cross-linking should cause an increase in the defect (D) band and a relative decrease in the G^+ band. There was no observed change in the D/G^+ ratio upon ultrasonication. The width of the G' band can be an indicator of the aggregation state of dispersed SWCNTs.[95] While there was a correlation between dispersion stability and the G' band width, this provided little insight into the cause of dispersion instability. We could not distinguish between SWCNTs from stable and unstable dispersions by Raman or UV-Vis-NIR spectroscopy. It is clear from our data that ultrasonication under these conditions does not damage the SWCNTs.

We also compared SWCNTs from stable and unstable dispersions with scanning electron microscopy (SEM). When deposited onto a substrate, one would expect a significantly more “crossed” network of tubes if the SWCNTs were cross-linking due to free radical initiation. There was no obvious morphological difference between stably dispersed SWCNTs and SWCNTs from unstable dispersions.

Further experimentation led to the observation that aggregated SWCNTs from an unstable dispersion could be centrifuged out and stably redispersed into fresh DMF. Also, DMF could be “pretreated” by a 2 hour ultrasonication while cooled by an ice bath, and it would be rendered unusable for making dispersions. Adding SWCNTs to “pretreated” DMF and ultrasonicating under a good protocol (*i.e.*, 30 minutes at high temperature) still resulted in an unstable dispersion. From these experiments and the Raman and SEM results, we concluded that SWCNTs are not significantly damaged or cross-linked during ultrasonication, but rather, the DMF is modified in a way that renders it incapable of dispersing SWCNTs.

Fresh DMF was compared to DMF that had been “IB” or “Hot” ultrasonicated for 2 hours using several analytical methods. UV-Vis and Raman spectroscopy showed no discernable difference between ultrasonicated and fresh DMF. NMR spectra showed an additional singlet for ultrasonicated DMF, due to small amounts of water absorbed during ultrasonication. FTIR spectra were, again, almost identical for ultrasonicated and fresh DMF. The only change was an increase in OH stretches, which we attributed to the absorbed water. There was no clear difference in the absorbed water concentration between “IB” and “Hot” ultrasonicated samples.

Water concentration can affect the dispersion limit of SWCNTs in DMF, so we tested whether it might also be affecting dispersion stability. DMF’s hygroscopic nature causes water to be absorbed during processing of uncovered samples, though ultrasonicated samples typically contain less that 0.5% water, as measured by NMR. To ensure that absorbed water was not significantly affecting SWCNT dispersability, a large stock dispersion was prepared by ultrasonicating 30 min without an ice bath. Samples were drawn from the stock dispersion and DI water was added to yield eight water concentrations ranging from 0.02% to 15% in DMF. Dispersion stability was monitored for five days at each of these water concentrations. Samples were centrifuged to remove aggregated SWCNTs and the SWCNT concentration of the supernatant was measured by UV-Vis-NIR spectroscopy.[68] Dispersion stability was unaffected on that time scale, but the SWCNT dispersion limit was reduced by up to 13% for higher water concentrations, but all of the samples showed stable SWCNT concentrations at a give water concentration. Since much higher water concentrations (15% compared to 0.5%) only seem to affect the dispersion limit, but not dispersion stability, absorbed water is not the cause of dispersion instability.

There were no detectable changes in the SWCNTs or DMF using standard analytical techniques. However, it was found that if a sample is deaerated with argon before and during "IB" ultrasonication, stable dispersions are formed. Conversely, if oxygen is bubbled through a sample during "IB" ultrasonication, dispersions become completely unstable, even during ultrasonications as short as 20 min. We also observed that "IB" ultrasonicated DMF exhibited an increase in conductivity and turned acidic, as determined by the indicator bromothymol blue (BTB).[96] The conductivities observed corresponded to ion concentrations on the order of 10^{-4} M, when compared to a conductivity calibration curve for NaBr in DMF, which is sufficiently high to collapse the electrical double layer that normally stabilizes dispersed SWCNTs. For comparison, the critical coagulation concentration of NaBr is $6.8\text{x}10^{-5}$ M for SWCNT dispersions in DMF.[74] It is well known[73] that DLVO theory can be used to model the aggregation of SWCNT dispersion, thus the observed SWCNT aggregation can be explained by classic DLVO theory.[75,76]

A variety of solvents often used to disperse SWCNTs were tested to see whether they exhibited similar properties after being "IB" ultrasonicated for 2 hours. *N*-methyl-2-pyrrolidinone (NMP) and *N,N*-Dimethylacetamide (DMA) dispersions also become unstable under those ultrasonication conditions. Dispersions in chloroform, o-dichlorobenzene, and THF were unaffected. Comparing the general properties of the solvents tested, DMF, DMA, and NMP are all polar aprotic solvents with methyl substituents. Acetonitrile, which does not disperse SWCNTs, but is a polar aprotic solvent with a methyl group, also showed the characteristic increase in conductivity and acidity after "IB" ultrasonication.

The observed commonalities among these solvents, especially the methyl groups, support our hypothesis that highly reactive methyl radicals are the cause of dispersion instability. However, the methyl radicals are not affecting the SWCNTs directly, but are modifying the solvent in a way that increases the ionic strength and acidity, which collapses the electrical double layer of dispersed SWCNTs due to the increased amount of electrolyte in solution.[73,74] Well known radical chemistry[97,98] details the formation of alkyl hydroperoxides by the autoxidation mechanism:

$$\cdot\mathrm{R} + \mathrm{O_2} \longrightarrow \cdot\mathrm{RO_2}$$

$$\cdot\mathrm{RO_2} + S\mathrm{H} \longrightarrow \mathrm{RO_2H} + \cdot S$$

Substituting a methyl radical for $\cdot\mathrm{R}$, as found in ultrasonicated DMF, NMP, DMA, and MeCN, the autoxidation mechanism specific to our study is:

$$\cdot\mathrm{CH_3} \;+\; \mathrm{O_2} \xrightarrow{1} \cdot\mathrm{CH_3O_2}$$

$$\cdot\mathrm{CH_3O_2} \;+\; S\mathrm{H} \xrightarrow{2} \mathrm{CH_3OOH} \;+\; \cdot S$$

where SH represents some solvent species. When $\cdot S$ is the methyl radical then this chain reaction should result in an exponential accumulation of methyl hydroperoxide. Our GC-MS data do not confirm a significant accumulation of methane and the accumulation of methyl hydroperoxide increases as a weak power law function as shown in Figure 3.7. While other radicals formed during ultrasonication and could form additional alkyl hydroperoxides, the formation of methyl hydroperoxide is the dominant reaction pathway for the solvents DMF, DMA, NMP, and acetonitrile. Solvents which do not contain a methyl group do not form any detectable alky hydroperoxide. The presence of water in our system is not included in this mechanism. Hydrogen abstraction from water would lead to the formation of HO_2, a weak acid which dissociates into H^+ and superoxide O_2^-. Using chemical and spectroscopic studies we were unable to detect the presence of superoxide.

In the sonochemically initiated autoxidation reaction outlined above, the product that accumulates is methyl hydroperoxide (CH_3OOH). There are no other examples of sonochemically initiated solvent autoxidation destabilizing SWCNT dispersions reported in the literature. The most similar example[99] of sonochemical hydroperoxide production uses sonochemistry to convert alkyl halides into alkyl hydroperoxides by “reductive oxygenation”. The sample conditions in this work are similar to ours, since they also cool their samples and aerate them to enhance the reaction.

Methyl hydroperoxide is acidic, which causes ultrasonicated polar aprotic solvents with methyl groups to show an increase in both acidity and conductivity. Although methyl hydroperoxide is a weak acid in water, based on the conductivity measurements mentioned above and [CH_3OOH] measurements described below, it dissociates well in these polar aprotic solvents. It is this dissociation into ions that causes dispersions to aggregate once the CCC has been reached. The accumulation of methyl hydroperoxide is a slow process, which is why dispersion collapse is not observed for short "IB" ultrasonications (unless O_2 is bubbled through). The rate-limiting step in radical initiated autoxidation reactions is typically H abstraction,[90,91,98] but it is apparent from our results that the concentration of dissolved oxygen ultimately limits the rate of methyl hydroperoxide production. It is obvious from the two-step autoxidation mechanism that methyl hydroperoxide will not be produced if oxygen is not present, which is why deaerated solvents remain pH neutral and deaerated dispersions remain stable and pH neutral.

Recall that dispersions from "Hot" ultrasonications are stable and dispersions from "IB" ultrasonications are sensitive to the presence of oxygen, as shown in Figure 3.2. Two hypotheses were considered to explain the temperature dependence; either O_2 solubility could be significantly reduced for high temperature ultrasonication or other radical reaction pathways become preferable to the H abstraction step in the mechanism above. Oxygen solubility versus temperature was measured with GC-MS. Samples were prepared by bubbling O_2 through a septum into DMF for 2 hours, to ensure O_2 saturation. O_2 solubility was measured at three temperatures: 0 ºC, 20 ºC, and 110 ºC. The samples were then injected into a GC-MS and the area under the oxygen peak was integrated. The relative concentration of O_2 at 0 ºC and 110 ºC were roughly 70% and 10% higher than at 20 ºC, respectively. This result revealed a common misconception we held, that gas solubility goes down with increasing temperature. Our results are consistent with Henry's Law constants[100], where the lowest O_2 solubility is at room temperature. O_2 solubility does not explain the observed temperature dependence.

There are many radical reaction pathways that can lead to terminal rather than chain reactions. The three primary terminal pathways are:[98]

$$2(\cdot RO_2) \xrightarrow{3} O_2 + ROOR$$

$$\cdot RO_2 + \cdot R \xrightarrow{4} ROOR$$

$$2(\cdot R) \xrightarrow{5} RR$$

where step 3 dominates at high $O_{2(g)}$ partial pressures and step 5 dominates for the $Ar_{(g)}$ sparged samples. Low temperature "IB" ultrasonication of acetonitrile yields an acidic, high conductivity solution. However, when the acetonitrile is held at 50 ºC or higher, the solution stays pH neutral and there is no conductivity increase. Moreover, there is a strong peroxide peak (~200nm) that does accumulate for all high temperature ultrasonications. At low temperature, the rate of methyl hydroperoxide formation is first order in $O_{2(g)}$ partial pressure in the solvent, yet at high temperature the rate is not as high due to competing chain termination reactions Though difficult to prove, these terminal reaction pathways may dominate over the slow H abstraction step at high temperatures. Consequently, no excess of methyl hydroperoxide can accumulate, solvents stay pH neutral, and dispersions are stable.

For IB+Ar ultrasonicated samples, ethane was detected by GC-MS, further confirming that the active radical species is the methyl radical. When samples did contain O_2 (IB+air or IB+O_2), ethane was not detected. This supports our claim that methyl radicals are consumed in the first step of the autoxidation mechanism. We were unable to determine which terminal pathway dominates during "Hot" ultrasonications, but the terminal pathways proposed above are appropriate for an autoxidation reaction. Nevertheless, the autoxidation mechanism, leading to methyl hydroperoxide production, explains all previous observations about SWCNT dispersion stability and the properties of "IB" ultrasonicated polar aprotic solvents.

We detected methyl hydroperoxide using standard methods such as the oxidation of iodide ions to triiodide.[101] The general reaction scheme is outlined below:

$$\mathrm{ROOH + 2H^+ + 2I^- \longrightarrow ROH + H_2O + I_2}$$

$$\mathrm{I^- + I_2 \rightleftharpoons I_3^-}$$

where we used a large excess of I^- to push the equilibrium to the right in the second step. Triiodide has strong optical absorption peaks at 290 nm and 365 nm.[101] After ultrasonicating an IB+O_2 sample for 2 hours, triiodide was detected with a concentration on the order of 10^{-4} M (as determined by the absorption peak at 365 nm), showing that methyl hydroperoxide is formed due to sonochemically initiated autoxidation of methyl radicals.

We used several spectroscopic methods to look for methyl hydroperoxide. NMR, although quite sensitive, was unable to detect the low concentration of methyl hydroperoxide. A concentration on the order of 10^{-4} M is less than 10 ppm, with respect to DMF (or other solvent), which we are unable to easily detect. The methyl hydroperoxide concentration is also too low to see in an IR spectrum. We were able to detect methyl hydroperoxide by UV-Vis-NIR, as it is known[102] that peroxides have an optical absorption below 200 nm. This absorption had not been observed in DMF, due to its UV cutoff at 270 nm, but a strong optical absorption was observed in IB+O_2 ultrasonicated acetonitrile, since this solvent has a lower UV cutoff at 190 nm. The intensity of this absorption scaled with ultrasonication time. This absorption is not a result of H_2O_2 formation, because it is present in "IB" ultrasonicated samples that were kept dry during ultrasonication with $MgSO_4$, so we attribute the absorption to methyl hydroperoxide.

Methyl hydroperoxide concentrations were quantitatively determined by titrating with NaOH, using BTB as the indicator. The final methyl hydroperoxide concentration was determined under six ultrasonication conditions in DMF. Three samples were "IB" ultrasonicated and three were "Hot" ultrasonicated. Figure 3.5 shows sample temperatures during ultrasonication. "IB" samples reach a final temperature of about 20 ºC and "Hot" samples reach about 110 ºC, both within about half an hour. For each temperature condition, one sample was deaerated with argon (Ar), one was bubbled with oxygen (O_2), and the third was left under atmospheric conditions (air). All ultrasonications were 2 hours long. The results, shown in Figure 3.6, correlate well with the observed dispersion stabilities. Whenever the methyl hydroperoxide concentration exceeded the critical coagulation concentration (CCC) for a $Z_+=1$ salt in DMF, the dispersions were unstable. This occurred when oxygen was present and samples were "IB" ultrasonicated. Further, we found that the amount of methyl hydroperoxide produced for IB+O_2 was 5x higher than for IB+air, indicating a first order reaction, since the partial pressure of oxygen in air is roughly 20%.

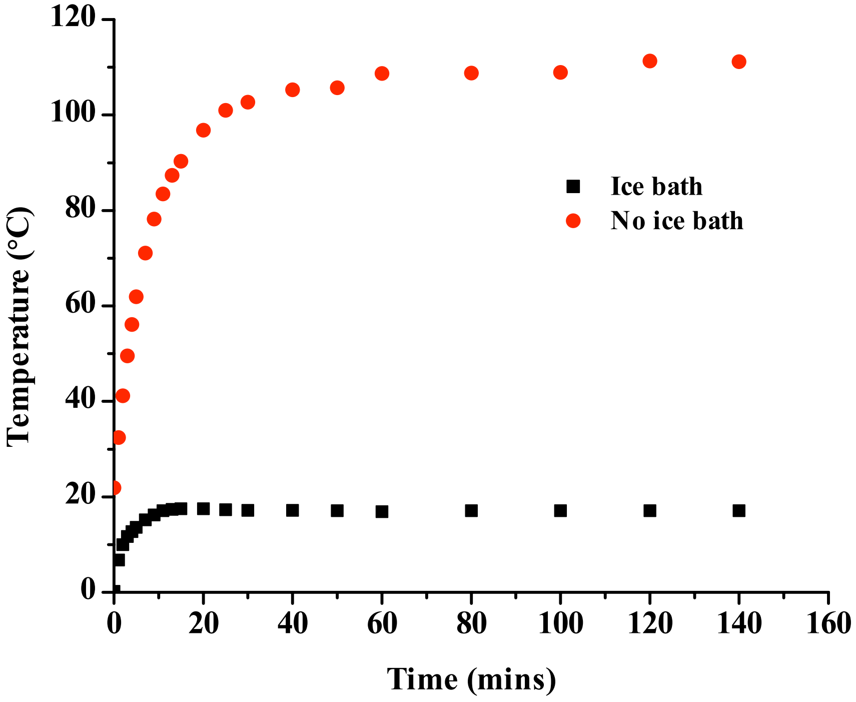

Figure 3.5: Temperature profile of samples during ultrasonication with and without an ice bath. Without an ice bath, the temperature stabilizes at ~110 ºC. With an ice bath, it stabilizes at ~20 ºC.

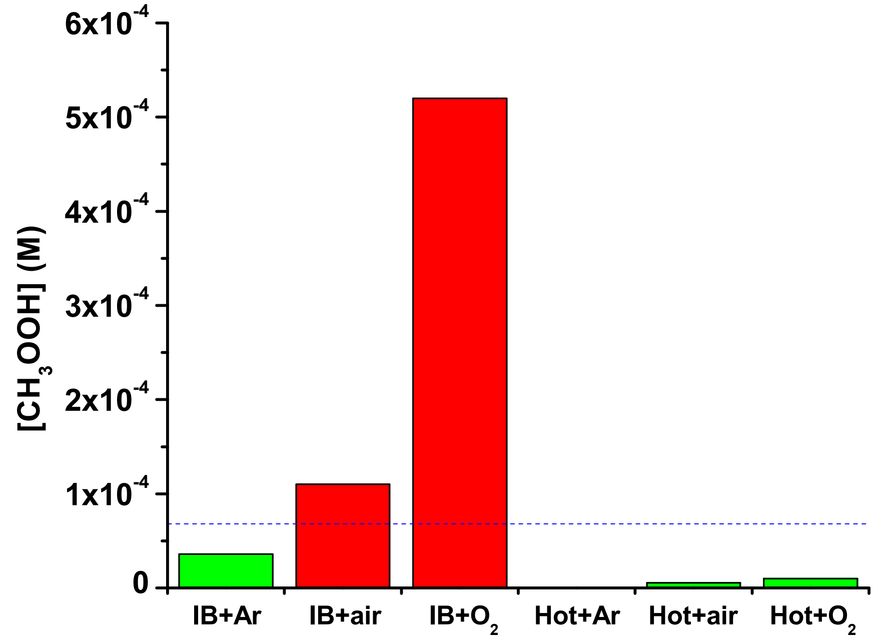

Figure 3.6: Typical methyl hydroperoxide concentrations in pure DMF after 2 hours of ultrasonication under various ultrasonication conditions. Shown in red are the two cases where stable dispersions cannot be formed, IB+air and IB+O_2. Under these conditions, the approximate methyl hydroperoxide concentration is greater than the CCC for NaBr (6.8 x 10^{-5} M), which is shown as a blue dashed line, demonstrating that the dispersions are unstable due to collapse of the electrical double layer.

For the two cases in which SWCNT dispersions are rendered unstable (IB+O_2 and IB+air), the concentration of methyl hydroperoxide was monitored as a function of ultrasonication time (Figure 3.7). In both cases, the methyl hydroperoxide concentration accurately predicts SWCNT dispersion stability when compared with the CCC for monovalent symmetric salt (6.8 x 10^{-5} M). Samples that were "IB" ultrasonicated and had O_2 bubbled through them are not stable after just 20 mins, where the methyl hydroperoxide concentration is equal to the CCC for a +1 coagulant. Without O_2 bubbling, it takes approximately 120 minutes of ultrasonication to reach that CCC. As shown in Figure 3.7, the concentration of methyl hydroperoxide increases according to a weak power law dependence.

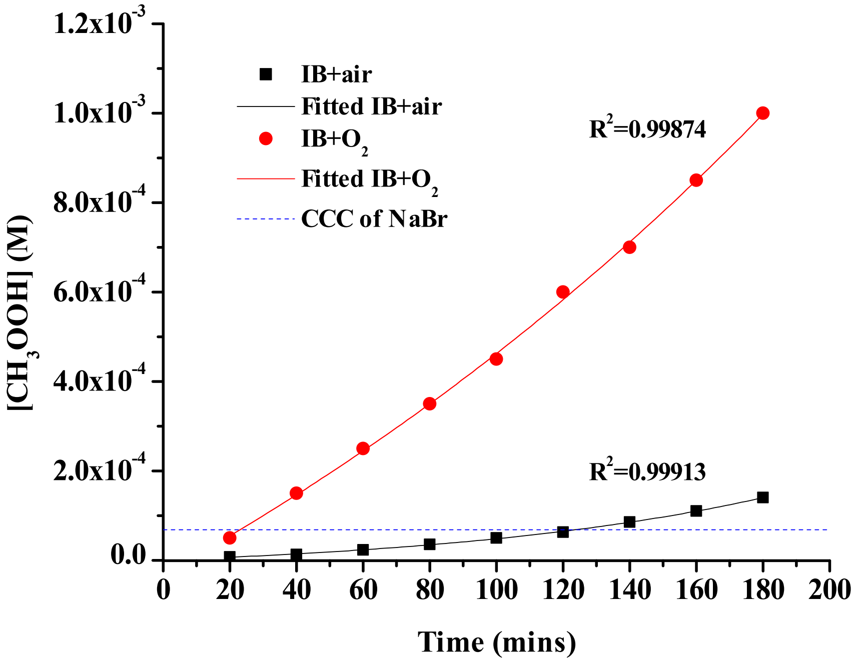

Figure 3.7: Concentration of methyl hydroperoxide in pure DMF as a function of ultrasonication time, when ultrasonicated in an ice bath. If O_2 is bubbled through the sample, the CCC is reached after ~20 min of ultrasonication. If no gas is bubbled through, it takes ~120 min to reach the CCC.

Many research groups use bath ultrasonication rather than tip ultrasonication to disperse SWCNTs, so we also checked whether methyl hydroperoxide is produced during bath ultrasonication. The power generated by bath ultrasonication is much lower, so we expect less of an effect than with tip ultrasonication. An O_2 saturated sample was bath sonicated for 5 hours kept at 0 ºC with a loose ice slurry, ensuring proper power transfer from the bath to the sample. Afterwards, the methyl hydroperoxide concentration was determined by titration to be 5.8×10^{-5} M, which is close to the expected CCC. Therefore there is enough power in a bath sonicator to produce similar reactions and thereby unintentionally destabilize a dispersion. More common bath ultrasonication protocols for dispersing SWCNT or other nanoparticles into small volumes do not use an ice bath or call for O_2 saturating the samples. Accordingly, we bath sonicated samples for 24 hours and allowed them to heat up to ~35 ºC. No change in acidity was detected, such that bath ultrasonication under mild and standard conditions does not induce the formation of methyl hydroperoxide in any appreciable quantity. As we scale these processes to larger volumes, higher power and possibly cooling will be required. The results presented here suggest that an O_2 free solution will enable a higher dispersion limit and a more stable dispersion.

We varied the ultrasonication temperature and oxygen concentration to demonstrate the stability of SWCNT dispersions as a function of ultrasonication time (Figure 3.3). The same six ultrasonication conditions used for the titration experiments were also used to study SWCNT dispersion stability. At high temperatures, dispersions are stable regardless of whether argon, oxygen, or no gas is bubbled through the sample. Dispersion instability occurs when the samples are cooled with an ice bath during high power tip ultrasonication. As can be seen in Figure 3.3, samples left under atmospheric conditions show progressively less stability as ultrasonication time increases. Samples that have argon bubbled through them are stable regardless of ultrasonication time because the autoxidation mechanism cannot occur. When oxygen is bubbled through the sample, the oxygen concentration (and consequently methyl hydroperoxide) is increased to the point where dispersions are not even stable after just 20 min (the concentration of SWCNTs falls to zero) of ultrasonication, precisely as predicted by the methyl hydroperoxide concentration as a function of time study (Figure 3.7).

3.4.4 Conclusions

SWCNTs and other nanoparticles have high surface energies and are prone to aggregation due to collapse of the electrical double layer, as described by DLVO theory. Sonochemical reactions that could lead to acidic or other ionic species must be avoided to maximize the dispersion limit and stability. It is apparent from the results of this study that is extremely important to monitor the experimental conditions when using ultrasonication to disperse nanomaterials into organic liquids, especially the methyl containing polar aprotic solvents. We have found that, given the right conditions, ultrasonically generated methyl radicals can initiate an autoxidation reaction leading to the production of methyl hydroperoxide and consequent destabilization of SWCNT dispersions. However, elimination of oxygen from samples prevents this reaction from occurring and high temperature ultrasonication allows terminal reaction pathways to dominate. Whenever dispersing nanoparticles, it is advisable to deaerate samples to eliminate potential sonochemical reactions involving absorbed oxygen, which could result in undesirable byproducts. As we show here, the polar aprotic solvent family is particularly susceptible to forming methyl hydroperoxide. We show that methyl hydroperoxide production by sonochemically initiated solvent autoxidation, leads to the destabilization of SWCNT dispersions.

This result is general across the polar aprotic solvents we studied and is particularly salient for DMF and NMP, as they are two of the best and most frequently used organic dispersants for SWCNT dispersions. We have noted discrepancies in dispersion limits reported in the literature[67-69] for these solvents, and believe that the formation of methyl hydroperoxide may be an important source of these discrepancies. Recent reports have even claimed that NMP can dissolve small SWCNTs in a true thermodynamically stable fashion.[70] We have shown that SWCNTs are not stable in NMP when the ionic strength exceeds the CCC. This low concentration of ions does not significantly change the dielectric constant of the dispersants, yet is does collapse the electrical double layer around the tubes. Therefore, SWCNTs in DMF, DMA, and NMP behave as a kinetically stable dispersion and do not appear to be a thermodynamically stable solution. More work is needed in this field to determine the true dispersion limits of SWCNTs in these and other solvents by ensuring that no sonochemical byproducts affect the dispersion limits. Further, it is important to clarify whether nanomaterials, such as SWCNTs, are forming solutions or dispersions and how we distinguish between the two.

3.5 Significantly Enhanced SWCNT Dispersion Stability in Mixed Solvent Systems

3.5.1 Introduction

Single-walled carbon nanotubes (SWCNTs)[1] must be dispersed into non-aqueous solvents to maintain pristine SWCNTs during processing. Pristine SWCNTs are necessary when studying unperturbed SWCNT properties[67,68] or supramolecular interactions.[103-105] Significant research effort has been directed towards determining dispersion limits for a wide variety of non-aqueous solvents,[67-70,72] yet little attention has been paid to the stability of SWCNT dispersions in response to perturbations like changes in ionic strength. Our recent work[10] showed that ultrasonication under certain conditions can destabilize SWCNT dispersions in some common solvents (NMP, DMF, and DMA). In this dissertation, we study the stability of SWCNT dispersion in mixtures of *N,N*-Dimethylformamide (DMF) and *N*-methyl-2-pyrrolidinone (NMP), which are commonly used to disperse pristine SWCNTs.

SWCNT dispersion limits are usually determined by ultrasonically dispersing SWCNTs into a solvent, removing any aggregated material by ultracentrifugation, then measuring the concentration of dispersed SWCNTs by absorption spectroscopy. The dispersion limit is acceptable if the concentration of the dispersion is stable for days or months. If, on the other hand, one wants to measure the stability of that dispersion rather then the dispersion limit, the system must be perturbed in a way that induces SWCNT aggregation. Knowledge of dispersion stability is important for scaling up SWCNT and nanomaterial processing, and this dissertation addresses one method (mixed solvents) that may help to move towards industrial scale processing of pristine SWCNTs.

Derjaguin, Landau, Verwey and Overbeek (DLVO) theory states that electrical double layer (EDL) repulsion counteracts the van der Waals attraction between particles in a dispersion.[75,77,106] Increasing the ionic strength of a SWCNT dispersion leads to collapse of the EDL, as described by DLVO theory. While the limitations of applying DLVO theory to SWCNT dispersions are known, it provides the motivation to use ionic species for experimentally determining the onset of aggregation, as well as the critical coagulation concentration (CCC) of SWCNT dispersions. The CCC and the onset of aggregation provide quantitative comparisons of the SWCNT dispersion stability in any solvent of interest.

Based on DLVO theory, an approximate particle-particle interaction potential between dispersed SWCNTs is calculated and shown in Figure 3.8a as a black line. The red and blue lines represent the attractive and repulsive terms, respectively, of the interaction potential, which come from vdW attraction and EDL repulsion. The interaction potential is shown in Figure 3.8b for three cases: ionic strength below the CCC, at the CCC, and above the CCC. When the coagulant concentration is significantly below the CCC, the potential barrier from EDL repulsion inhibits SWCNT aggregation. Increasing the ionic strength of the solvent reduces that potential barrier by collapsing the EDL, which allows slow aggregation (reaction-limited aggregation). The CCC is defined as the onset of fast aggregation (diffusion-limited aggregation), where the rate of aggregation reaches a maximum.

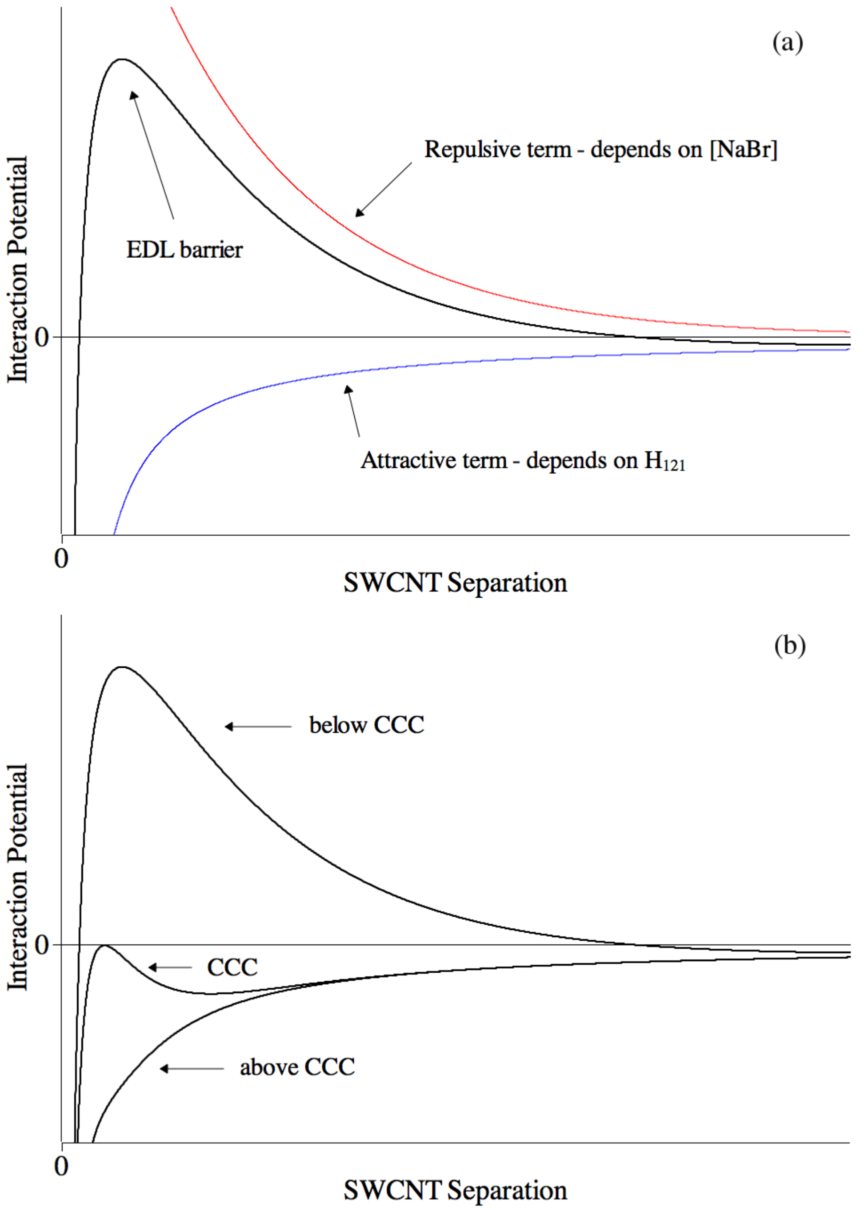

Figure 3.8: DLVO interaction potential, showing attractive and repulsive terms. (a) Plot of the interaction potential between two dispersed SWCNTs. The attractive and repulsive terms of the DLVO potential are shown red and blue lines, respectively. (b) Plot showing the interaction potential below, at, and above the CCC.

Measuring the CCC provides fundamental insight into the stability of a dispersion and yields quantitative information about the interaction potential for a solvent/SWCNT system. However, when processing dispersions of pristine SWCNTs, it is more important to know how sensitive the system is to ionic contaminants that may be unintentionally introduced into the sample. Alternatively, one might develop a directed assembly process, where an ionic species is necessary in one or more steps. In this case, one needs to know how robust the SWCNT dispersion will be during these processing steps.

We have studied the onset of slow aggregation, as a measure of SWCNT dispersion stability, for mixtures of DMF and NMP. By measuring the fraction of SWCNTs dispersed as a function of coagulant concentration, it is possible to determine the SWCNT dispersion stability in a given solvent system. We provide a physical model based on DLVO theory and the Maxwell-Boltzmann energy distribution function, which fits the data well and allows quantitative comparison between solvent systems. These results were published in J. Phys. Chem. C: Forney, M. W.; Poler, J. C. *The Journal of Physical Chemistry C* **2011**, 115, 10531.

3.5.2 Experimental Methods

N,N-Dimethylformamide (Fisher, Spectranalyzed), *N*-methyl-2-pyrrolidinone (OmniSolv, Spectrophotometry & Gas Chromatography), and deuterium oxide (Acros Organics), were used as purchased, and kept dry under an $N_{2(g)}$ blanket. Single-walled carbon nanotubes were HiPCO (Grade P CNT from CNI, now Unidym), and were used as-received.

SWCNT dispersions were prepared by adding SWCNT powder (0.5-1.0 mg) to the chosen solvent (20 mL). The mixture was tip ultrasonicated without temperature or gas environment regulation for 30 min at 10 W RMS by a Fisher Scientific Sonic Dismembrator 60 (1/8" tip ultrasonicator). After ultrasonication, dispersions were ultracentrifuged with a Beckman Optima XL-100K at 20,000 g for 20 min to sediment any undispersed SWCNTs. The supernatant was carefully collected, and the final concentration of SWCNT dispersions was 6-12 mg L^{-1}, depending on the solvent and sample.

Coagulation experiments for SWCNT dispersions were performed by adding NaBr dissolved in the appropriate solvent or solvent mixture. NaBr dissociates in these solvents, as confirmed by conductivity measurements with a Fisher Scientific Accumet AR20. 1 mL samples for the aggregation studies were prepared by adding NaBr solution to SWCNT samples, yielding NaBr concentrations from 10^{-5} M to 10^{-3} M. The samples were allowed to incubate for 48 hours, because of the slow aggregation rates near the onset of aggregation. Each sample was then centrifuged at 1000 g for 10 minutes in a Fisher Scientific Micro16 tabletop centrifuge to sediment any aggregated SWCNTs. Supernatant (100 μL) was immediately transferred to a cuvette to measure the SWCNT concentration based on the optical absorption.[68,74] SWCNT concentrations were normalized to a reference sample that did not have any NaBr added to it. Three to five measurements were collected for each NaBr concentration.

3.5.3 Results & Discussion

We determined the dispersion stability of SWCNTs dispersed in mixed solvent systems of DMF and NMP, using NaBr as the coagulant. The seven mixed solvent systems had volume fractions of V_{DMF} = 0.0, V_{DMF} = 0.1, V_{DMF} = 0.3, V_{DMF} = 0.5, V_{DMF} = 0.7, V_{DMF} = 0.9, and V_{DMF} = 1.0. The aggregation results for DMF/NMP mixtures are summarized in Figure 3.9. We found that NMP has higher dispersion stability than DMF, which correlates with reports in the literature that NMP has a higher dispersion limit than DMF.[68,71] We also found that mixtures of NMP and DMF can yield significantly higher dispersion stability than either pure solvent.

NaBr was chosen because it is a monovalent inorganic salt that does not bind to the SWCNTs. This is important, because we study the kinetics of aggregation at a constant coagulant concentration. We confirmed that NaBr does not bind to SWCNTs during aggregation by measuring the conductivity of the supernatant from four fully aggregated SWCNT dispersions in NMP, where [NaBr] = 10^{-3} M. The samples were centrifuged to pellet the SWCNTs before measuring the conductivity of the supernatant. After a 10x dilution, the average supernatant conductivity of the four samples was 6.12 μS, with a standard deviation of 0.20 μS. The expected conductivity was 6.3 μS, meaning that [NaBr] is not binding and not affected by SWCNT aggregation.

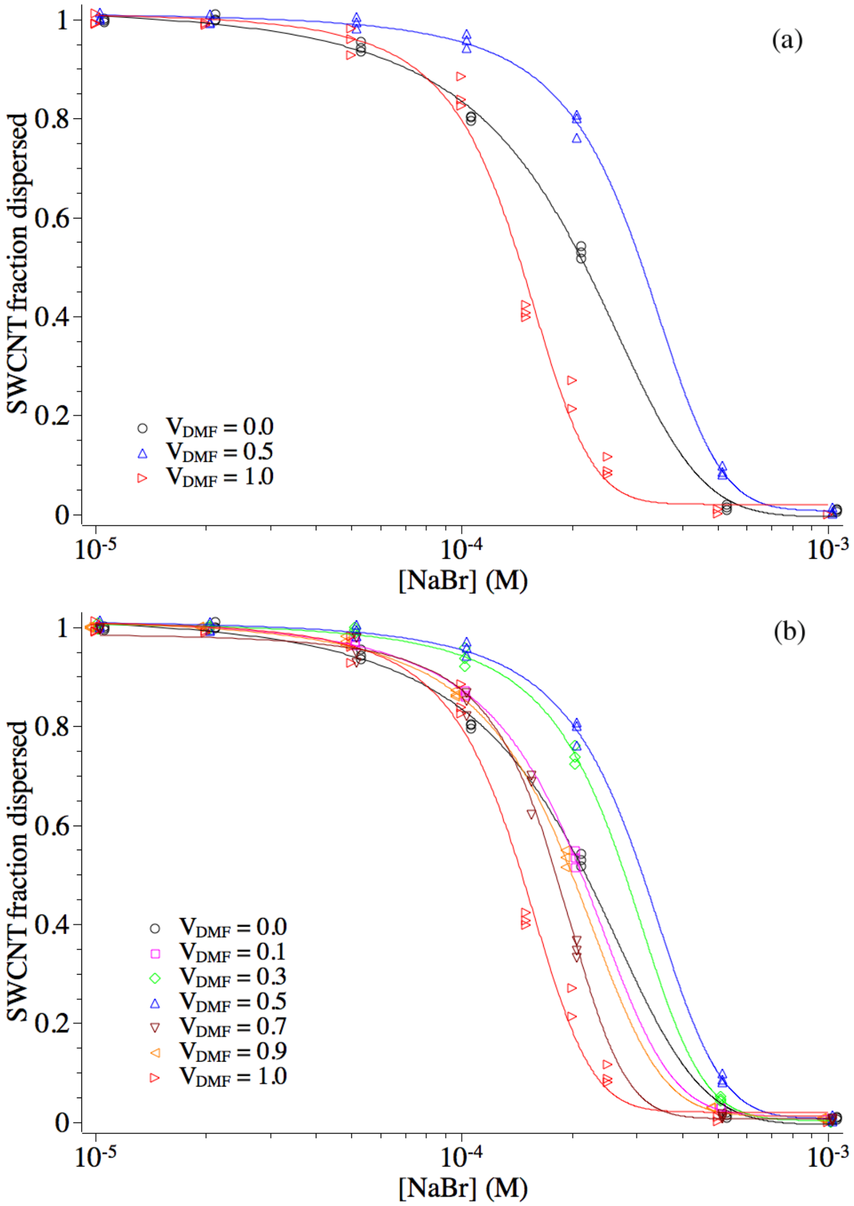

Figure 3.9: Summary of dispersion stability data for mixtures of DMF and NMP. In (a), only the points $V_{DMF} = \{0.0, 0.5, 1.0\}$ are shown, for visual clarity. All of the data points are shown in (b) and fitted with our mathematical model (solid lines).

3.5.3.1 Physical and mathematical models

To understand and properly analyze our dispersion results, we start with DLVO theory, as it describes the stability of colloidal dispersions. When a stable dispersion is created, the colloids (or SWCNTs) are unable to aggregate due to the potential barrier from EDL repulsion. The barrier, illustrated in Figure 3.8, can be described by the sum of the attractive vdW interactions between particles and the EDL repulsive force.[77] The EDL barrier can be described by the following potential[77]

$$V(h) = \pi R\left\{-\frac{H_{121}}{12\pi}\frac{1}{h} + \frac{64k_BTc_0\Gamma_0^2}{\kappa^2}\exp(-\kappa h)\right\}$$

where h is the particle separation, H_{121} is the Hamaker constant, and c_0 is the coagulant concentration. This potential is formulated for sphere-sphere interactions, but there is no appropriate formula for interactions between flexible rods, so we use this as a first approximation. The Debye screening length is defined as

$$\frac{1}{\kappa} = \left(\frac{\varepsilon_0\varepsilon_r k_BT}{2e^2c_0}\right)^{1/2}$$

for a monovalent salt, and the parameter Γ_0 is defined by

$$\Gamma_0 = \tanh\left(\frac{e\Phi_0}{4k_BT}\right)$$

where e is the charge on an electron and Φ_0 is the surface potential of dispersed particles. For non-adsorbing ions, we use a constant surface potential and assume the

Langmuir approximation. $V(h)$ can be rewritten to highlight the variables that modulate the attractive and repulsive terms

$$V(h) = -\left[\frac{R}{12}\frac{1}{h}\right]H_{121} + \left[\frac{32k_B^2T^2\Gamma_0^2\varepsilon_0\varepsilon_r\pi R}{e^2}\exp\left(\frac{\sqrt{2}eh}{(\varepsilon_0\varepsilon_r k_B T)^{1/2}}\right)\right]\exp(-c_0^{1/2})$$

To clarify the dependence of the potential on the relevant parameters, we have re-written the above equation as:

$$V(h) = -C_1H_{121} + C_2\exp(-c_0^{1/2})$$

where the left brackets contain C_1 and the right brackets contain C_2 from the previous equation. The left term of the interaction potential, $V(h)$, is the attractive term and depends on the Hamaker constant. The right term is from EDL repulsion, which will depend on the coagulant concentration, c_0. Note that the repulsion term decreases exponentially with increasing coagulant concentration. All other variables are held constant in our experiments and have been collected into coefficients C_1 and C_2.

Although SWCNT dispersions can be kinetically stable for long time periods, they are thermodynamically unstable. Dispersed SWCNTs diffuse through their dispersing medium with an average kinetic energy of 3/2 k_BT. The distribution of energies is described by the Maxwell-Boltzmann distribution. Even when the EDL repulsion barrier is significantly larger than k_BT, an infinitesimal fraction of the SWCNTs can leak over the barrier and aggregate, which is why all SWCNT dispersions will eventually collapse.

After preparing a stock SWCNT dispersion, we add NaBr to 1 mL samples at varying concentrations and incubate the samples for 48 hours. No measurable aggregation occurs for the control samples, which contain no NaBr, even after weeks or months. The fraction of SWCNTs that remain dispersed falls of sigmoidally, as a function of increasing [NaBr], (see Figure 3.9). When adding coagulant, we lower the EDL barrier and effectively increase the fraction of SWCNTs that have enough energy to overcome the repulsive barrier. The distribution of SWCNT energies is described by the Maxwell-Boltzmann distribution

$$f(E) = \frac{2}{\sqrt{\pi}} \frac{1}{\left(k_B T\right)^{3/2}} \sqrt{E} \exp\left(-\frac{E}{k_B T}\right)$$

which depends solely on the temperature of the system. By taking the integral of the Maxwell-Boltzmann distribution for energies higher than the EDL barrier

$$P(aggregation) = \int_{E_{EDL}}^{\infty} f(E)dE = 1 + \left[\frac{2}{\sqrt{k_B T \sqrt{\pi}}}\right] \sqrt{E_{EDL}} \exp\left(-E_{EDL}/k_B T\right) - \left[\frac{2}{\sqrt{\pi}}\right] \int_{0}^{\sqrt{E_{EDL}/k_B T}} e^{-u^2} du$$

we are able to compute the fraction of SWNTs that will aggregate. To simplify this equation as:

$$P(aggregation) = \int_{E_{EDL}}^{\infty} f(E)dE = 1 + C_3 \sqrt{E_{EDL}} \exp\left(-E_{EDL}/k_B T\right) - C_4 \int_{0}^{\sqrt{E_{EDL}/k_B T}} e^{-u^2} du$$

where C_3 and C_4 are constant and E_{EDL} is inversely related to [NaBr]. The integral with respect to u is the sigmoidally-shaped error function. In Figure 3.10a, P(aggregation) is represented by the red shaded area underneath a Maxwell-Boltzmann distribution and indicates the fraction of SWCNTs that will aggregate at a given NaBr concentration. Using the function P(aggregation), we are able to compute the fraction of SWCNTs that will aggregate as a function of [NaBr], as shown in Figure 3.10b (see Supplemental Information for more details). Due to the inverse relationship between

[NaBr] and E_{EDL}, the horizontal axis in Figure 3.10b represents the reduction of E_{EDL} with the addition of NaBr. The black curve is P(aggregation) and the blue curve is 1 - P(aggregation). The blue curve indicates the fraction of SWCNTs that stay dispersed, which is what we measure experimentally.

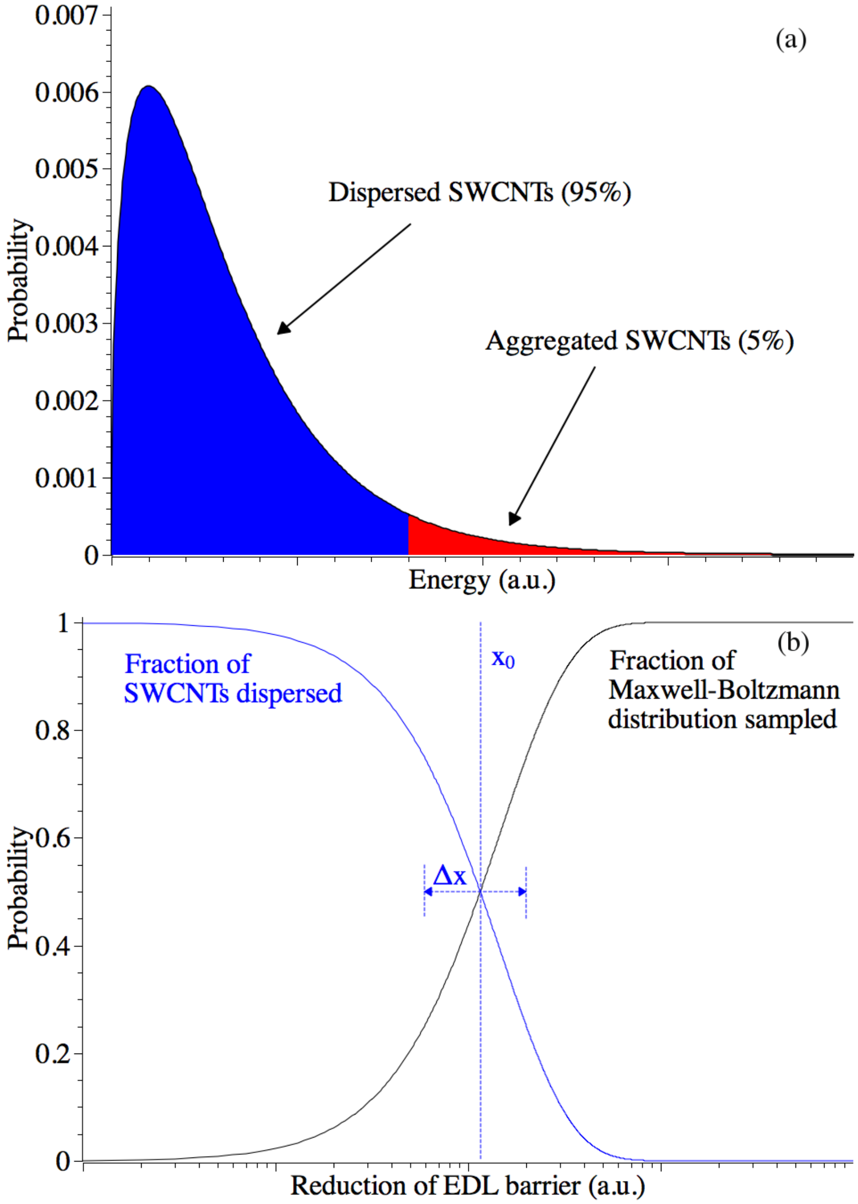

Figure 3.10: Physical model for aggregation profile. (a) Maxwell-Boltzmann distribution for a situation where 5% of the dispersed SWCNTs have enough energy to overcome EDL repulsion. (b) Shows the effect of reducing the EDL barrier (adding coagulant) on the fraction of SWCNTs that stay dispersed, which is the inverse of the P(aggregation).

To model our experimental aggregation data, we use a sigmoidal equation that approximates P(aggregation) as

$$\frac{[SWCNT]}{[SWCNT]_0} = A_2 + \frac{A_1 - A_2}{1 + \exp\left(\frac{[NaBr] - x_0}{\Delta x}\right)}$$

where A_1 is the asymptotic maximum, A_2 is the asymptotic minimum, [NaBr] is the coagulant concentration, x_0 is the center point, Δx indicates the steepness of the transition between A_1 and A_2, and $\frac{[SWCNT]}{[SWCNT]_0}$ is the measured probability of each SWCNT to stay dispersed at that NaBr concentration. This equation offers a simple set of parameters to describe our data and fits the integrated probability of aggregation with a reduced χ^2 of 5.3×10^{-6} and $R^2 = 0.9999$. SWCNT concentrations are normalized to reference samples without NaBr, so $\frac{[SWCNT]}{[SWCNT]_0}$ ranges between 0 and 1, and can be interpreted as the probability for SWCNTs to remain dispersed at the corresponding [NaBr].

We know from DLVO theory that the EDL barrier height is inversely related to the coagulant concentration, [NaBr]. When $[NaBr] = x_0$, the EDL barrier height is such that half of the SWCNTs aggregate ($\frac{[SWCNT]}{[SWCNT]_0} = 0.5$). A higher x_0 value indicates higher SWCNT dispersion stability, since more coagulant is needed to aggregate half of the dispersed SWCNTs. The parameter Δx is the width of the range $0.25 \le \frac{[SWCNT]}{[SWCNT]_0} \le 0.75$ (see Figure 3.10b). Thus, a larger Δx value also indicates higher SWCNT dispersion stability. When comparing dispersion stability, x_0 is the primary parameter we consider. The fitting parameters from the experimental data shown in Figure 3.9 are listed in Table 3.1. All data were fitted with our mathematical model and the fitted functions are plotted in Figure 3.9 as solid lines. In most cases, we found that $A_1 \approx 1$ and $A_2 \approx 0$.

Table 3.1: Fitting parameters for all solvent systems tested, when using our mathematical model. Data is fit with the Levenberg-Marquardt algorithm, and the reported errors are the errors in the fitting parameters.

Solvent System	A_1	A_2	x_0 (μM)	Δx (μM)
$V_{DMF} = 0.0$	1.17 ± 0.04	-0.01 ± 0.01	191.0 ± 6.6	97.7 ± 7.2
$V_{DMF} = 0.1$	1.07 ± 0.01	0.01 ± 0.01	201.9 ± 1.9	69.1 ± 3.1
$V_{DMF} = 0.3$	1.04 ± 0.01	0.00 ± 0.01	273.3 ± 3.7	75.3 ± 3.7
$V_{DMF} = 0.5$	1.04 ± 0.01	0.01 ± 0.01	304.0 ± 4.6	85.0 ± 3.4
$V_{DMF} = 0.7$	1.00 ± 0.01	0.01 ± 0.01	180.5 ± 2.4	42.0 ± 2.7
$V_{DMF} = 0.9$	0.98 ± 0.02	0.00 ± 0.02	190.8 ± 3.3	38.9 ± 3.0
$V_{DMF} = 1.0$	1.03 ± 0.02	0.02 ± 0.02	142.2 ± 3.7	35.4 ± 3.5

3.5.3.2 Mixtures of DMF and NMP

We have plotted the fitting parameters x_0 and Δx as a function of mole fraction (χ_{DMF}) in Figure 3.11. We show that mixtures of DMF and NMP can improve the stability of SWCNT dispersion significantly. Using x_0 as the primary measure of dispersion stability, we find that a mixture at χ_{DMF} = 0.55 is 59% more stable than pure NMP and 114% more stable than pure DMF. In fact, as little as 10% NMP (v/v) makes DMF dispersions as stable as pure NMP dispersions. These dispersion stability experiments in mixed solvents have huge implications for researchers who want to increase the stability of pristine SWCNT dispersions in organic solvents. The change in x_0 is quadratic in χ_{DMF}, which reflects the favorability of using mixed solvents to increase SWCNT dispersion stability (see Figure 3.11).

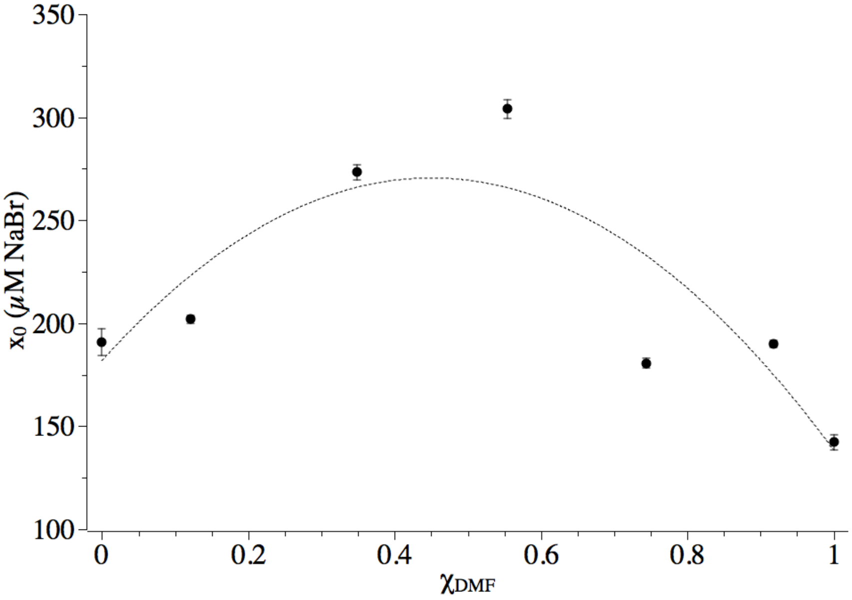

Figure 3.11: Plot of the primary stability parameter, x_0 vs mole fraction DMF. A parabola has been fitted through the x_0 data to highlight the increased stability when a mixture of DMF and NMP is used to disperse SWCNTs.

Hansen solubility parameters take into account dispersion, polar, and hydrogen bonding interactions of solvents,[107] and provide insight into our dispersion stability results. The relationship between these three parameters and the Hildebrand solubility parameter is[107]

$$\delta^2 = \delta_D^2 + \delta_P^2 + \delta_H^2$$

where δ is the Hildebrand solubility parameter, δ_D is the Hansen dispersion parameter, δ_P is the Hansen polar parameter, and δ_H is the Hansen hydrogen bonding parameter. Research has shown that Hildebrand/Hansen parameters have strong correlations with dispersion limits of good nanotube solvents.[71,108] We find that Hildebrand/Hansen parameters also provide insight into our dispersion stability experiments. Table 3.2 shows the Hildebrand/Hansen parameters that have been predicted to yield optimal dispersion limits by Coleman, *et al.*[71] These proposed optimal Hildebrand/Hansen parameters will be referred to as δ', δ'_D, δ'_P, and δ'_H.

Table 3.2: Hildebrand/Hansen solubility parameters for solvent systems and predicted optimal SWCNT parameters. Solubility parameters for solvent mixtures were calculated by linear interpolation.

Solvent system	x_0 (μM NaBr)	δ (MPa$^{1/2}$)	δ_D (MPa$^{1/2}$)	δ_P (MPa$^{1/2}$)	δ_H (MPa$^{1/2}$)
SWCNT [71]	-	20.8	17.8	7.5	7.6
$V_{DMF} = 0.0$	191.0 ± 6.6	23.0	18.0	12.3	7.2
$V_{DMF} = 0.1$	201.9 ± 1.9	23.2	17.9	12.4	7.6
$V_{DMF} = 0.3$	273.3 ± 3.7	23.6	17.8	12.7	8.4
$V_{DMF} = 0.5$	304.0 ± 4.6	24.0	17.7	13.0	9.3
$V_{DMF} = 0.7$	180.5 ± 2.4	24.3	17.6	13.3	10.9
$V_{DMF} = 0.9$	190.8 ± 3.3	24.7	17.5	13.6	10.9
$V_{DMF} = 1.0$	142.2 ± 3.7	24.9	17.4	13.7	11.3

Dispersion stability (x_0) has been plotted against each of the solvent parameters on a common horizontal axis in Figure 3.12a. By plotting the data this way, we can see how DMF/NMP mixtures compare to the optimal values suggested by Coleman, *et al.* The δ_D parameter correlates best with our experimental data, as it predicts that the optimal mixture of DMF and NMP would occur at V_{DMF} = 0.3, as shown in Figure 3.12b. For the δ_H and δ parameters, the optimal value lies outside of the range spanned by DMF/NMP mixtures and are closer to the values for pure NMP (V_{DMF} = 0). The last parameter, δ_H, has an optimal value that corresponds to the mixture V_{DMF} = 0.1. These observations are consistent with our experimental results showing that dispersion stability is highest when $V_{DMF} \leq 0.5$. Also, since the δ_D parameter has the greatest magnitude, it is reasonable that we observe the highest dispersion stability in the range $0.3 \leq V_{DMF} \leq 0.5$.

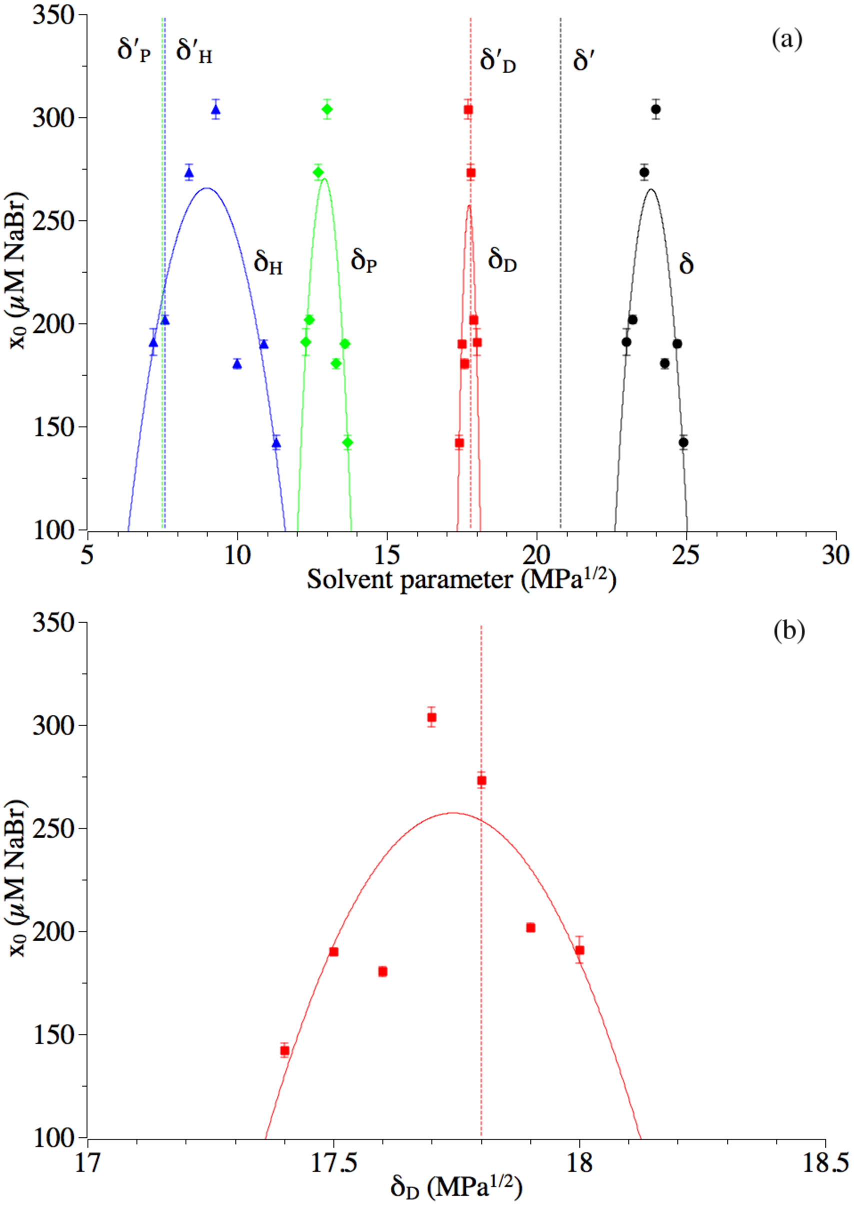

Figure 3.12: Hildebrand and Hansen parameters plotted against x_0. In (a), dispersion stability (x_0) is plotted against each of the solubility parameters independently. The solid lines are quadratic fits to the experimental x_0 values (marked with δ_i), and the vertical dashed lines indicate the optimal solubility parameters (marked with δ'_i) , as determined by Coleman, *et al.*[71] In (b), the dispersive parameter, δ_D, is plotted alone because it supports our experimental observations that an equal mixture of DMF and NMP enhances dispersion stability.

We can qualitatively explain why SWCNT dispersions are more stable in mixtures of DMF and NMP by applying Flory-Huggins polymer solubility theory.[109] In Flory-Huggins theory, the free energy of mixing is[77]

$$\Delta G_{mix} = RT(n_s \ln \Phi_s + n_{SWCNT} \ln \Phi_{SWCNT}) + (n_s + N_{SWCNT} n_{SWCNT}) w \Phi_{SWCNT} \Phi_s$$

where the first term is the entropy and the second term is the enthalpy of mixing. R is the molar gas constant, T is the temperature, n_S is the number of moles of solvent, n_{SWCNT} is the number of moles of SWCNTs, N_{SWCNT} is the degree of polymerization ($N_{SWCNT} \propto$ SWCNT length), and Φ_{SWCNT} and Φ_S are the volume fractions of SWCNT and solvent, respectively. The effective interaction parameter, w, is related to the Flory-Huggins interaction parameter by

$$\chi_{12} = \frac{w}{RT} = \frac{V_0 \left(\delta_{SWCNT} - \delta_s\right)^2}{RT}$$

where V_0 is the solvent molar volume, δ_{SWCNT} is the Hildebrand parameter for SWCNTs, and δ_S is a Hildebrand/Hansen parameter for the solvent.[109] When mixing solvents, any differences in dispersion stability will result mainly from changes in the enthalpy term, because the interaction parameter, χ_{12}, changes. The farther a solvent parameter is from the optimal value, δ_{SWCNT}, the larger the value of χ_{12}, which means a larger excess enthalpy of mixing and lower dispersion limits.

The interaction parameter w, and thus χ_{12}, is a measure of pair-wise interactions[77]

$$w = \alpha\left(W_{11} + W_{22} - 2W_{12}\right)$$

where W_{11} represents interactions between solvent molecules, W_{22} represents interactions between SWCNTs, W_{12} represents interactions between solvent molecules and SWCNTs, and α is a fitting parameter. The interaction parameter has the same physical meaning as the Hamaker constant used in DLVO theory[77]

$$H_{121} = H_{11} + H_{22} - 2H_{12}$$

where H_{11} represents interactions between solvent molecules, H_{22} represents interactions between SWCNTs, and H_{12} represents interactions between solvent molecules and SWCNTs.

Since $\chi_{12} \propto H_{121}$, through w, the best SWCNT dispersion are formed when $\delta_{SWCNT} = \delta_S$, which results in a minimum value for χ_{12} and H_{121}. When H_{121} is minimized, there is a maximum in the dispersion stability, x_0, as shown in Figure 3.11. This is important for understanding how mixing solvents affects the interaction potential between dispersed SWCNTs. We know that by adding coagulant, we reduce the EDL barrier height, thereby reducing the repulsive term of the DLVO interaction potential (see Figure 3.13a). However, by mixing solvents, we reduce the magnitude of the attractive term of the DLVO interparticle potential by reducing the Hamaker constant, H_{121}. When we minimize H_{121} by mixing two solvents, the EDL barrier height is effectively increased due to the reduction in the attractive DLVO term, leading to more stable SWCNT dispersions (see Figure 3.13b).

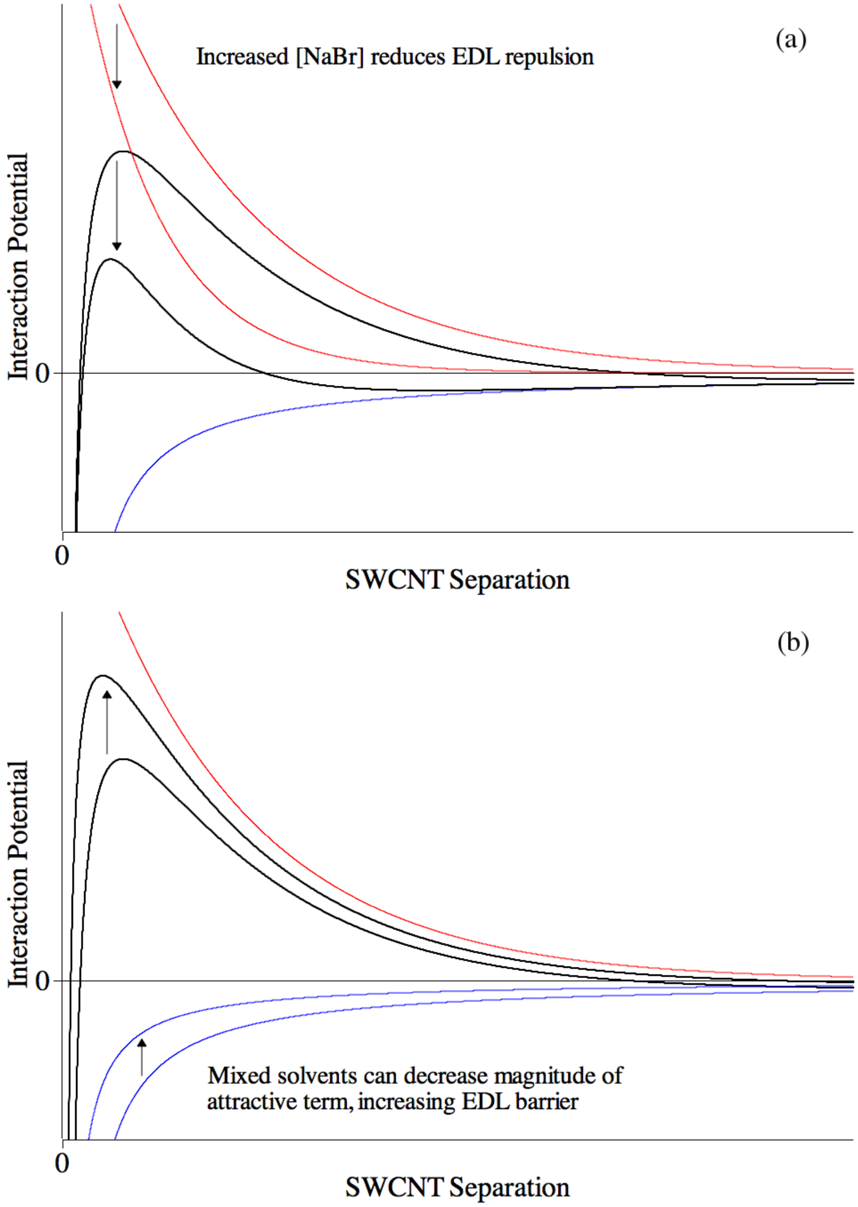

Figure 3.13: Effect of adding NaBr or mixing solvents on interaction potential. Red curves show the repulsive term of the DLVO potential, blue curves show the attractive term of the DLVO potential, and black curves are the full DLVO potential. (a) Shows how increasing [NaBr] reduces the repulsive term of the interaction potential and the EDL barrier height. (b) Shows how mixing solvents to optimize solvent parameters can decrease the magnitude of the attractive term (H_{121}), thereby increasing the EDL barrier height.

By mixing solvents, we can optimize the Hansen parameters of the solution. Hildebrand/Hansen parameters for solvent mixtures were estimated by linear interpolation between accepted values for DMF and NMP. Our results in Figure 3.12 show that we get the most stable dispersions when the dispersive Hansen parameter of the solvent mixture nearly matches the optimal SWCNT dispersive parameter (i.e. $\delta_D \cong \delta'_D$), which agrees with our qualitative model based on Flory-Huggins polymer theory. This model suggests that the most stable dispersions should occur when $V_{DMF} = 0.3$, and we find experimentally that $0.3 \leq V_{DMF} \leq 0.5$ produces the most stable dispersions. The hydrogen bonding Hansen parameter indicates that a mixture of $V_{DMF} = 0.1$ should be optimal. The Hildebrand parameter and the polar Hansen parameter suggest that NMP dispersions should be the most stable. By combining DLVO theory, Flory-Huggins polymer theory, and Hildebrand/Hansen solubility parameters, we are able to understand how coagulants destabilize SWCNT dispersions and how solvent mixing can be used to enhance dispersion stability.

3.5.4 Conclusion

This work demonstrates that mixtures of solvents can yield significantly higher dispersion stability than pure solvents. We have described the probability of SWCNT aggregation in mixtures of DMF and NMP, as a function of coagulant concentration (i.e. [NaBr]). By combining DLVO theory, Flory-Huggins polymer theory, and Hildebrand/Hansen solubility parameters, we have modeled the enhanced SWCNT dispersion stability in mixed solvents. We are currently studying SWCNT dispersion stability in other mixed solvent systems. We anticipate that mixed solvents can also be useful for enhancing dispersion limits. More research needs to be focused on understanding and quantifying the stability of SWCNT dispersions under conditions that arise during dispersion processing, such as the introduction of ionic species or water. Theoretical work is needed to better understand the mechanism by which the enhanced dispersion stability occurs and to more accurately model SWCNT interparticle interaction.

3.6 Aggregation Kinetics of Single-Walled Carbon Nanotubes in Non-aqueous Solvents – Critical Coagulation Concentrations and Transient Dispersion Stability

3.6.1 Introduction

Single-walled carbon nanotubes (SWCNTs)[1] have been widely studied because of their excellent electronic, optical, and mechanical properties.[2-8] Pristine SWCNTs are typically dispersed into non-aqueous solvents, while acid-oxidized or surfactant-coated SWCNTs are typically dispersed into water/D_2O. The choice of solvent medium depends on the experimental or application needs, but the only way to study truly pristine SWCNTs is by dispersing them into non-aqueous solvents, even though the dispersion limits and stability are typically lower than for surface functionalized or surfactant-coated SWCNTs. It is important to understand dispersion stability from both fundamental and applied perspectives.

In Derjaguin, Landau, Verwey, and Overbeek (DLVO) theory, colloidal dispersions remain stable due to electrical double-layer repulsion (EDL),[75,77,106] which can be reduced by adding ionic coagulants (i.e. salts that coagulate dispersions). DLVO theory describes two different regimes of aggregation: reaction-limited colloid aggregation (RLCA) and diffusion-limited colloid aggregation (DLCA). In the RLCA regime, there is some small probability that two interacting colloids will aggregate. In the DLCA regime, the EDL barrier has been reduced to the point where the aggregation probability of two closely interacting colloids is essentially 100%. Critical coagulation concentrations (CCCs) are used in DLVO theory to define the critical point at which diffusion-limited aggregation is reached, and adding more coagulant no longer changes the aggregation rate constant.

The DLVO model is commonly used to describe aggregation of carbon nanotubes (CNTs),[73,74,81-87] though the limitations in approximating the physical and chemical constraints of a SWCNT dispersion are appreciated. Dynamic light scattering (DLS) is frequently used to measure the change in effective diameter for dispersed CNTs,[83-87] and the initial rate of change in the effective diameter is used to determine relative aggregation rate constants. There are three weaknesses with this method: (1) the effective diameter is approximated using a model that assumes spherical particles, (2) aggregation kinetics are observed indirectly based on effective diameter approximations, and (3) the intensity of scattered light is dominated by large aggregates ($I_S \propto d^6$). SWCNT aggregates can quickly reach sizes of microns or tens of microns, which makes it difficult to observe the initial stages of aggregation, where the measured effective diameter is approximately 200 nm. In order to observe the aggregation kinetics of SWCNT dispersions directly, we developed a sedimentation technique that allows us to remove aggregated SWCNTs, as the bundles form, by centrifuging the samples for the duration of the aggregation experiment.

Using this technique to study CCCs of SWCNT dispersions in DMF, NMP, and 50/50 DMF/NMP (v/v) has led to several important results. Through our sedimentation technique, we have found strong evidence of a “transient stability” in the aggregation kinetics of NMP and DMF/NMP dispersions. It is hypothesized that the transient stability we observe is due to differences between interfacial SWCNT-DMF and

SWCNT-NMP interactions. Computational studies support our understanding of why transient stability is observed in dispersions with NMP as the (co-)solvent.[110,111]

Our recently published paper[82] focused on studying the "onset of aggregation", which occurs at much lower coagulant concentrations, showed that dispersion stability could be significantly enhanced in that aggregation regime by mixing DMF/NMP to optimize the dispersive Hansen solubility parameter. The data presented in this dissertation show that solubility parameter optimization does not enhance dispersion stability at higher coagulant concentrations, as determined by comparing CCCs. It is clear from our results that non-DLVO interactions play a significant role in the aggregation process. These results have been submitted for publication in the Journal of Physical Chemistry C.

3.6.2 Experimental Methods

N,N-Dimethylformamide (Fisher, Spectranalyzed) and *N*-methyl-2-pyrrolidinone (OmniSolv, Spectrophotometry & Gas Chromatography) were used as purchased, and kept dry under an $N_{2(g)}$ blanket such that water contamination is below 1000 ppm. Single-walled carbon nanotubes were HiPCO (Grade P CNT from CNI, now Unidym), and were used as-received.

SWCNT dispersions were prepared by adding SWCNT powder (1-2 mg) to the chosen solvent or solvent mixture (20 mL). The mixture was tip ultrasonicated without temperature or gas environment regulation[10] for 30 min at 10 W RMS by a Fisher Scientific Sonic Dismembrator 60 (1/8" tip ultrasonicator). After ultrasonication, dispersions were ultracentrifuged with a Beckman Optima XL-100K at 20,000 g for 20 min to sediment any undispersed SWCNTs. The supernatant was carefully collected, then diluted to a final SWCNT concentration of ~6 mg L^{-1} and ultrasonicated for another 30 min to ensure excellent dispersion. Stock coagulant solutions (NaBr and $CaCl_2$) were prepared for each solvent or solvent mixture, typically with coagulant concentrations 10x higher than needed for the data point with the highest coagulant concentration (usually 0.01-0.1 M).

Aggregation kinetics experiments were performed by centrifuging SWCNT dispersions, immediately after adding coagulant to the system, for 1-20 min at 10,000 g in an Eppendorf 5415C microcentrifuge. Below 10,000 g, the final SWCNT concentration depends strongly on the sedimentation field, but it remains essentially constant above 10,000 g for a fixed coagulant concentration and aggregation time. In each experiment, a sample and control are centrifuged simultaneously. The control is prepared by mixing 900 μL SWCNT dispersion with 100 μL solvent, and the sample is prepared by mixing 900 μL SWCNT dispersion and 100 μL of appropriately diluted salt solution. The 900 μL of SWCNT is added to the 100 μL of solvent or diluted salt solution and mixed thoroughly by pipet 3 times to ensure homogeneity. After 10-20 min of aggregation/centrifugation time, the supernatant (100 μL aliquot) of the sample/control was immediately transferred to a cuvette to measure the SWCNT concentration based on the optical absorption.[68,74] The SWCNT concentration of the control samples did not decrease during centrifugation. Five aggregation times were measured for each coagulant concentration and 6-9 coagulant concentrations were tested for each solvent or solvent mixture. As described elsewhere,[82] we used conductivity measurements to confirm that the coagulating ions do not bind to the tubes during aggregation, and the salt concentration remains constant throughout each kinetics experiment.

Thermogravimetic analysis (TGA) experiments were used to compare the affinity of the three solvent systems for the SWCNT surface. For these experiments, we used a Mettler Toledo TGA/SDTA 851 and Sigma-Adrich SWCNTs (Product #589705-1G). For each solvent system, 25 mg of SWCNT were added to 2 mL of solvent and tip ultrasonicated for 15 s to create a slurry. The slurry was then deposited on a glass frit and "air dried" by vacuum filtration for 15 min. The resulting SWCNT mat was removed, crushed, and transferred to an Al_2O_3 crucible. In the TGA, the sample was heated to 100 ºC and allowed to soak for 120 min to remove most of the residual bulk solvent. Then the TGA was ramped to 600 ºC at a rate of 5 ºC/min to collect desorption data.

3.6.3 Results & Discussion

Our sedimentation technique allows us to directly measure, by optical absorption, the amount of SWCNT that remains dispersed after aggregating for a certain time at a certain coagulant concentration. Four sets of aggregation data are shown in Figure 3.14. Each set of data is collected at a specific [NaBr] so that aggregation rate constants can be determined. In DLVO theory, it is typically assumed that aggregation is described by a single rate constant,[77] but we find that a single exponential decay does not describe our aggregation data well. Our data is better fit by a double exponential decay, indicating that there are fast and slow aggregation processes that are occurring, as described by the equation

$$[SWCNT] = A_F \exp(k_F t) + A_S \exp(k_S t)$$

where A_F and A_S are scaling factors (fast and slow), k_F and k_S are rate constants (fast and slow), and t is time.

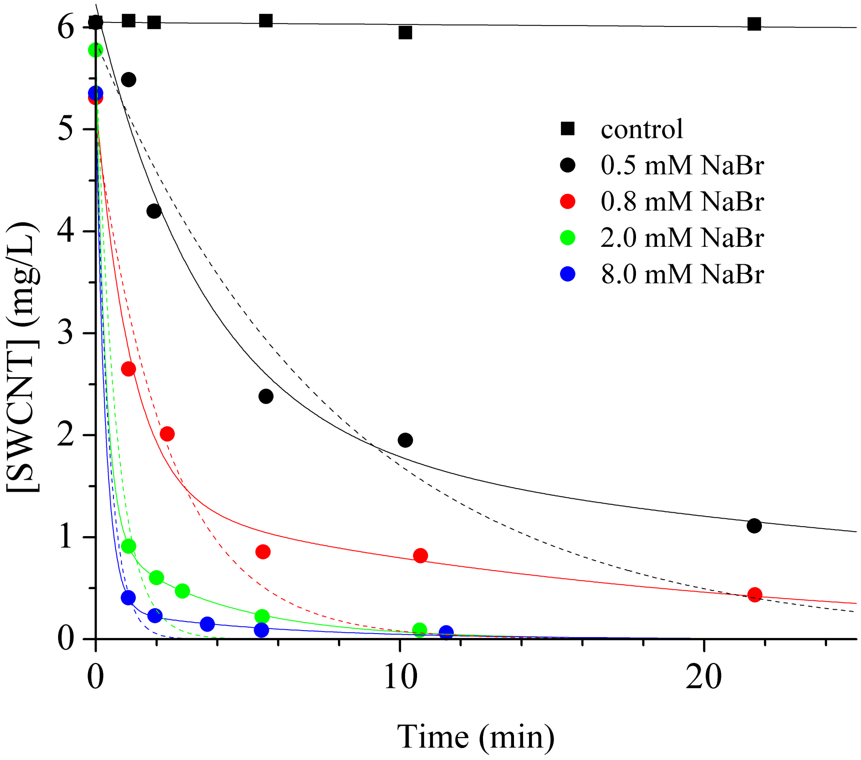

Figure 3.14: Aggregation kinetics data for several concentrations of NaBr in DMF. Single exponential decay fits are shown as dashed lines and double exponential decay fits are shown as solid lines. A representative set of control data is shown as black squares to show that no SWCNTs are removed from the control samples during 20 min of centrifugation at 10,000 g.

In Figure 3.14, single exponential decay fits are shown as dashed lines and double exponential decay fits are shown as solid lines. The double exponential decay model more accurately describes our aggregation data, especially when approaching DLCA. For example, fitting the 2 mM NaBr data in Figure 3.14 with a single exponential gives a reduced χ^2 value of 0.0896, but fitting with a double exponential gives a reduced χ^2 value 5.152×10^{-4}. Similarly, fitting the 8 mM NaBr data with a single exponential gives a reduced χ^2 value of 0.0158, and fitting with a double exponential gives a reduced χ^2 value 6.608×10^{-4}. The fast decay term measures early stages of SWCNT aggregation, and the slow decay term is associated with subsequent aspects of the aggregation process. Consequently, our analysis of the CCCs will rely on the fast rate constant term, where the aggregation rate constant is maximal.

Relative aggregation rate constants are used to determine the inverse stability ratio, $1/W$. The maximum rate constant occurs above the CCC, in the diffusion-limited regime. Our measured k_D values are proportional to the viscosity of the solvent, indicating true diffusion-limited aggregation. The inverse stability ratio, $1/W$, is the ratio of the RLCA rate constant, k_R, to the DLCA rate constant, k_D.

$$\frac{1}{W}=\frac{k_R}{k_D}$$

The inverse stability ratio normalizes aggregation rate constants to the diffusion-limited aggregation rate constant and allows for simple comparison between coagulation experiments. Figure 3.15 shows inverse stability ratio plotted against coagulant concentration for each of the coagulant/solvent systems studied.

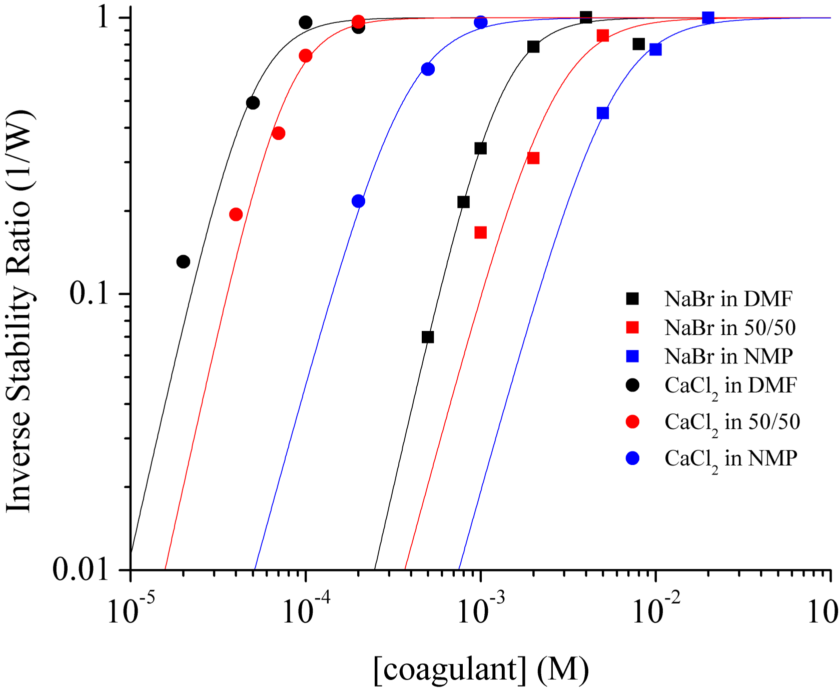

Figure 3.15: Merged plot of inverse stability ratio data for all of the solvent/coagulant combinations tested. Solid lines show the fit of the empirical model we use to calculate CCCs from inverse stability ratio data.

To analyze and interpret these results, we fit the inverse stability ratio data with the following empirical equation[86,112]

$$\frac{1}{W}=\frac{1}{1+\left(CCC/[coagulant]\right)^{\beta}}$$

where the fitting parameters are the CCC and β, the slope $d\log(\frac{1}{W})/d\log([coagulant])$ in the reaction-limited regime. In Figure 3.15, the data are fitted with the equation above and the fits are shown as solid lines. We have tabulated the CCCs, standard error in the CCCs, and the reduced χ^2 of the fit for each coagulant/solvent system in Table 3.3.

3.6.3.1 Comparison of CCCs with "onset of aggregation"

Our recent study reported on SWCNT dispersion stability at the "onset of aggregation" in DMF, NMP, and mixtures of DMF/NMP.[82] We considered the "onset of aggregation" to be the coagulant concentration that caused 50% of the SWCNTs to aggregate in 48 hr, which is significantly lower than the concentration range where CCCs occur, but more relevant to the processing of SWCNT dispersions when ionic species could be introduced into the system. An important finding was that dispersion stability was significantly enhanced by up to 115% in mixtures of DMF and NMP due to optimization of the dispersive Hansen solubility parameter.

Figure 3.15 shows clearly that the CCCs for DMF/NMP mixtures are higher than CCCs in pure DMF and lower than CCCs in pure NMP. We do not observe any enhancement in dispersion stability in this aggregation regime. Since the dispersive Hansen solubility parameter is a bulk solvent property, this result suggests that interactions at the SWCNT-solvent interface become much more important near the

CCC, whereas bulk solvent properties have a greater impact on dispersion stability near the “onset of aggregation”, or at low coagulant concentrations.

Further comparison between our CCC results and “onset of aggregation” results[82] support this conclusion. When comparing dispersion stability using the “onset of aggregation”, we find that NMP dispersions are 1.34 times more stable than DMF dispersions when aggregated with NaBr. Comparing CCCs shows NMP dispersions to be 4.35 times more stable than DMF dispersions when aggregated with NaBr, indicating that the stronger SWCNT-NMP interactions are more important during DLCA. The aggregation mechanism at the “onset of aggregation” appears to be different than at the CCC. Aggregation occurs quite rapidly near the CCC, and the tube-tube distances are quite short, so interfacial interactions play a larger role in determining aggregation kinetics.

Table 3.3: CCCs, standard error in the CCCs, and the reduced χ^2 of the fit for the solvent/coagulant systems tested.

	CCC (M)	Standard error (M)	Reduced χ^2
NaBr in DMF	1.27×10^{-3}	1.37×10^{-4}	9.58×10^{-3}
NaBr in DMF/NMP	2.56×10^{-3}	3.50×10^{-4}	8.05×10^{-3}
NaBr in NMP	5.53×10^{-3}	5.03×10^{-4}	3.39×10^{-3}
$CaCl_2$ in DMF	4.79×10^{-5}	3.50×10^{-6}	3.21×10^{-3}
$CaCl_2$ in DMF/NMP	7.55×10^{-5}	5.01×10^{-6}	4.56×10^{-3}
$CaCl_2$ in NMP	3.61×10^{-4}	3.27×10^{-5}	3.43×10^{-3}

3.6.3.2 Schulz-Hardy analysis

The Schulze-Hardy rule is an empirical rule that describes how the CCC of simple salts varies with the valence of the ion that dominates the coagulation of the dispersion.[77] Since SWCNTs have a negative ζ–potential, we consider the valence of the cation. For Na^+, $z_+ = +1$, and for Ca^{2+}, $z_+ = +2$. The high-potential DLVO model predicts a z^{-6} dependence of the CCC for simple symmetric salts like NaBr. For asymmetric salts like $CaCl_2$ the CCC falls off less steeply. For comparison between 1:1 monovalent electrolytes (NaBr) and 2:1 asymmetric divalent electrolytes ($CaCl_2$), it has been calculated[112,113] that ratio between CCCs should be $2^{-5.4}$. In the low-potential model, the Schulze-Hardy rule predicts a z^{-2} CCC dependence on valence. As with the high-potential model, this dependence varies for asymmetric electrolytes, and the CCC ratio has been calculated[113] to be $2^{-1.8}$ for a 2:1 asymmetric electrolyte. We expect the low-potential model to be valid if the coagulant binds to the particles, which we do not observe.

Our CCC data, in Table 3.3, show reasonable agreement with Schulze-Hardy rule for 2:1 asymmetric electrolytes. For DMF dispersions we find a CCC dependence of $2^{-4.73}$, for DMF/NMP dispersions we find a CCC dependence of $2^{-5.29}$, and for NMP dispersions we find a CCC dependence of $2^{-3.94}$. All of these values are within the range predicted by the Schulze-Hardy rule, though it is difficult to draw specific conclusions from these variations in CCC dependence. This difficulty is highlighted by widely varying results published in the literature,[73,83,84,86] where the Schulze-Hardy dependence ranges from $2^{-3.27}$ to $2^{-6.28}$, for aggregation of oxidized SWCNTs or MWCNTs from aqueous dispersions.

3.6.3.3 “Transient stability” for NMP dispersions

When we use NMP as the solvent, the aggregation kinetics reveal a dramatic difference compared to DMF dispersions. At coagulant concentrations below the CCC, a transient stability that can last longer than 10 min is observed before appreciable aggregation begins. The effect is observed for NMP dispersions aggregated by both NaBr and $CaCl_2$. Figure 3.16 and Figure 3.17 show the difference in the aggregation profile for NaBr and $CaCl_2$, respectively, with DMF dispersions on the left and NMP dispersions on the right. Note that dashed lines are used in Figure 3.16, Figure 3.17, and Figure 3.18 to guide the eye for datasets that exhibit transient stability effects. These data were not used in calculating aggregation rate constants or CCCs.

We hypothesize that the observed transient stability results from the way NMP molecules interact with the surface of SWCNTs. Research has shown that NMP has an extremely high affinity for the surface of SWCNTs and that NMP molecules can remain physisorbed to the SWCNT surface after a 30 min anneal at 340 ºC in UHV.[70] Recent molecular dynamics (MD) simulations[111] calculated potentials of mean force (PMFs) between graphene sheets solvated in various solvents, including DMF and NMP. Based on the calculated PMFs, they concluded that graphene dispersions in NMP should be more stable that in DMF, which is consistent with experimental data for the dispersion of SWCNTs into these solvents.

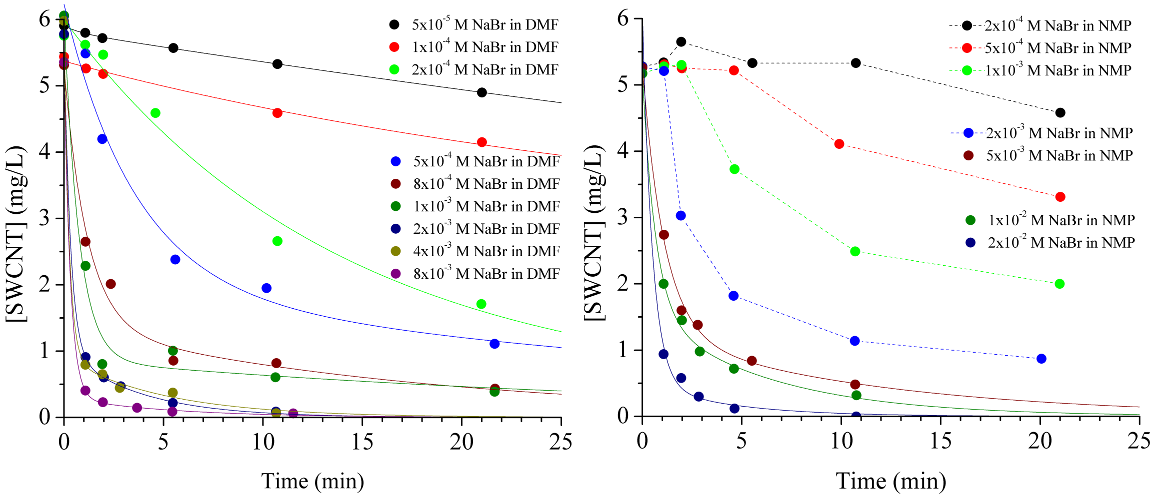

Figure 3.16: Aggregation kinetics of dispersions in DMF (left) and NMP (right) that were aggregated by NaBr. Solid lines are double exponential fits to the aggregation data at a given [NaBr]. When transient stability was observed in NMP dispersions, dashed lines are shown to guide the eye, but this data was not fitted or included in the CCC analysis.

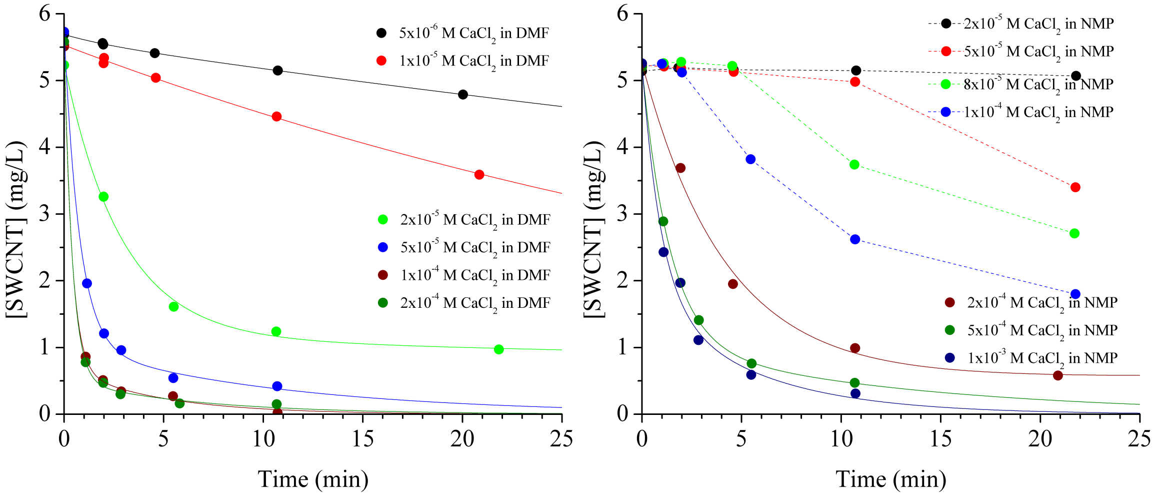

Figure 3.17: Aggregation kinetics of dispersions in DMF (left) and NMP (right) that were aggregated by $CaCl_2$. Solid lines are double exponential fits to the aggregation data at a given [$CaCl_2$]. When transient stability was observed in NMP dispersions, dashed lines are shown to guide the eye, but this data was not fitted or included in the CCC analysis.

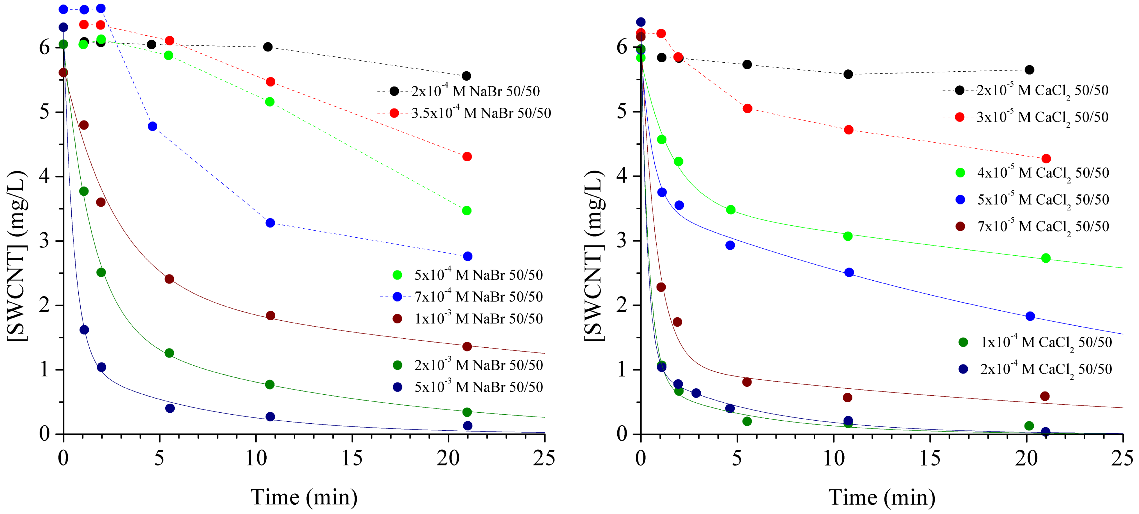

Figure 3.18: Aggregation kinetics of dispersions in DMF/NMP that were aggregated by NaBr (left) and $CaCl_2$ (right). Solid lines are double exponential fits to the aggregation data at a given [$CaCl_2$]. When transient stability was observed in DMF/NMP dispersions, dashed lines are shown to guide the eye, but this data was not fitted or included in the CCC analysis.

Our hypothesis is that, due to the strong surface interactions between NMP and SWCNTs, a surfactant-like shell of NMP molecules must be disrupted before significant aggregation can occur, which leads to transient stability on the order of minutes, even when the coagulant concentration is near the CCC. Recent theoretical work predicts such long-lived transient effects in the aggregation of SWCNTs dispersed in NMP.[110] In this work, the authors use all-atom MD simulations to calculate the Landau free energy vs. inter-SWCNT distance for pairs of SWCNTs fully solvated in NMP. Simulations were run with parallel (180°) and perpendicular (90°) SWCNTs, as well as sixty angles in between (1.5° increments). By calculating the Landau free energy as a function of torsion angle, they found a 5-6 kcal/mol (8-10 kT) barrier between 110° and 140°, which would lead to experimentally measurable effects on aggregation rates.

Further, they propose that a pair of SWCNTs must (1) diffuse rotationally until they are nearly perpendicular in order to minimize the energy required to break the surface tension of the monolayer of highly associated NMP molecules at the SWCNT-NMP interface, then (2) after contact has been made, the 8-10 kT activation barrier will cause a measurable delay before the pair of SWCNTs can form a parallel bundle. We find experimentally that the length of the transient stability decreases with increasing coagulant concentration. Although the average time delay in step (2) should be independent of coagulant concentration, SWCNTs will make contact (step (1)) more rapidly when the coagulant concentration is increased, decreasing the duration of the transient stability.

We find that the aggregation mechanism described above, determined from MD simulations, provides a reasonable model for understanding our experimental observation that NMP dispersions show a period of transient stability before any aggregation can be measured. We hypothesize that such a torsional free energy barrier does not exist, or is significantly smaller, due to the fact that we do not observe any transient stability in the aggregation kinetics of DMF dispersions. We also performed several TGA experiments to compare the desorption of DMF, DMF/NMP, and NMP from SWCNTs. The results qualitatively suggested that higher temperature (energy) was needed to remove DMF/NMP and NMP from SWCNTs, after the residual bulk solvent had been removed. Our desorption experiments showed solvent affinities for SWCNT in the following order: DMF < DMF/NMP < NMP.

3.6.3.4 "Transient stability"for DMF/NMP dispersions

When we study dispersions made in DMF/NMP, we observe the same type of transient stability as with NMP dispersions. Interestingly, in three out of the four salt/solvent combinations, the length of the transient stability correlates well with the amount of SWCNT still dispersed after 20 min of aggregation. For NaBr in NMP, $CaCl_2$ in NMP, and NaBr in DMF/NMP, the aggregation profiles are quite similar at coagulant concentrations where transient stability becomes observable. In contrast, when $CaCl_2$ is the coagulant in DMF/NMP dispersions, the transient stability is less pronounced, and the aggregation profile is distinctly different from the other three coagulant/solvent combinations that show transient stability. Figure 3.19 shows how $CaCl_2$ in DMF/NMP differs from the other combinations when 1-2 min of transient stability is observed. The SWCNT concentrations have been normalized to facilitate comparison between the coagulant/solvent combinations, highlighting how the aggregation kinetics for $CaCl_2$ in DMF/NMP are different. Although the coagulant concentrations vary for each salt/solvent combination, the aggregation profiles shown in Figure 3.19 all correspond to inverse stability ratios of $1/W = 0.02\text{-}0.05$, which reinforces the observation that there is a difference in how $CaCl_2$ coagulates SWCNTs in DMF/NMP.

We also observed that the CCCs of SWCNT dispersions in DMF/NMP are closer to the CCCs of DMF dispersions than NMP dispersions. The DMF bias depends on which coagulant is used. When $CaCl_2$ is the coagulant in DMF/NMP, the CCC is much closer to the CCC of $CaCl_2$ in DMF than NMP. In contrast, the CCC for NaBr in DMF/NMP is closer to an average of the DMF and NMP CCCs, though it is still closer to the DMF CCC (see Table 3.3 and Figure 3.15).

When $CaCl_2$ is the coagulant, both the aggregation profiles and CCCs suggest that DMF's role is more important than NMP's role in determining the aggregation kinetics in DMF/NMP dispersions. When NaBr is the coagulant, the aggregation profiles for DMF/NMP dispersions are similar to NMP dispersions and the CCC is nearly the average of the DMF and NMP CCCs. It appears that the Ca^{2+} ions may somehow disrupt the NMP-SWCNT surface interactions as SWCNTs aggregate. The mechanism of the Ca^{2+} disruption requires further investigation.

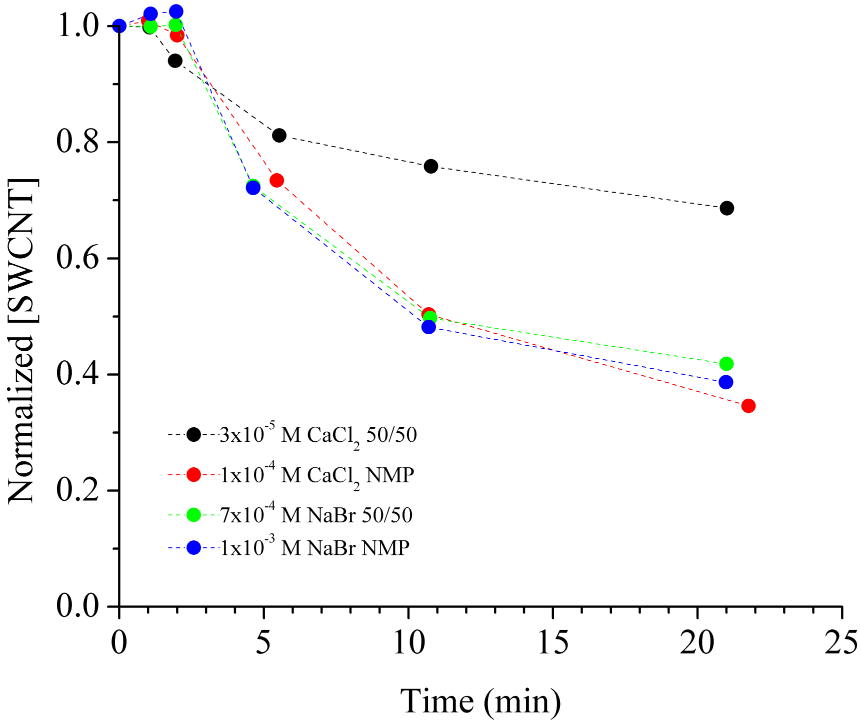

Figure 3.19: Comparison of aggregation profiles when transient stability is observed. When we aggregate DMF/NMP dispersions with CaCl₂, the aggregation profile is markedly different from the other three solvent/salt combinations, as demonstrated by these four data sets where there is 1-2 min of transient stability before measurable aggregation begins.

3.6.3.5 Conclusion

In this dissertation we have presented CCCs for SWCNT dispersions in DMF, NMP, and DMF/NMP when aggregated by NaBr and $CaCl_2$. Aggregation kinetics were studied by measuring [SWCNT] by optical absorption after 1-20 min of aggregation with simultaneous centrifugation to remove aggregated material. The coagulant concentration was increased until the aggregation rate constant saturated, indicating that diffusion-limited aggregation had been reached. Comparison of CCCs showed that the CCC for DMF/NMP is closer to the DMF CCC than the NMP CCC for both coagulants tested.

Transient stability was also observed in the aggregation kinetics of NMP and DMF/NMP dispersions. This transient stability is attributed to a torsional energy barrier of 8-10 kT that aggregating SWCNTs need to overcome before forming a bundle. Theoretical MD simulations predict this torsional energy barrier in NMP dispersions, which should lead to long-lived transients like the transient stability we observe experimentally. We believe that any torsional energy barrier to bundling in DMF dispersions must be significantly smaller, since we do not observe any transient stability in the aggregation kinetics of DMF dispersions

In addition to the results just mentioned, comparison to our recent work near the "onset of aggregation" shows that significant differences in dispersion stability exist in the CCC regime. The enhancement in dispersion stability for DMF/NMP mixtures at lower coagulation concentrations disappears in the diffusion-limited aggregation regime, as interfacial SWCNT-solvent interactions become more important than bulk solvent properties. The results of this work are important for gaining insight into the nature of

SWCNT-solvent interactions near the CCC in these commonly used non-aqueous solvents.

CHAPTER 4: NANOELECTROMECHANICAL ACTUATORS BASED ON CARBON NANOTUBES

4.1 Actuator Design

The superior electrical and mechanical properties of CNTs have inspired many researchers to incorporate CNTs into composites, electronics, photovoltaics, field-emission devices, sensors, and actuators.[4,15,16,62,114-122] CNTs are especially useful when considering electromechanical actuators, as they can be loaded with a large number of electrons[4,123] and have tremendous mechanical integrity.

The proposed design for a nanoelectromechanical actuator can trace its roots to simple bimorphs that have been used for many years in simple devices like thermostats. Efforts to actuate microcantilevers have lead researchers in many fields to exploit the concept of a bimorph using a wide variety of approaches. Several examples are DNA hybridization,[124] virus detection,[125] redox reactions,[126,127] swelling of polymer brushes,[128] and self-assembly of alkanethiols.[129] Our nanoelectromechanical actuator will consist of VA-CNTs grown on one side of a microcantilever, which has not been demonstrated in the literature.

The original inspiration for our actuator design came from the work of Fritz, *et al.*,[124] where DNA hybridization was studied by functionalizing the surfaces of microcantilevers, as shown in Figure 4.1. In this work they measured changes in surface stress on microcantilevers during DNA hybridization by measuring the deflections of the microcantilevers as different DNA pairs were injected into the liquid cell. An optical lever system was used to measure the deflections, which were on the order of tens of nm. This work is a clear demonstration of how microcantilever arrays can provide a good platform for measuring small changes in surface stress based on the interactions of materials on the microcantilever surfaces.

A related source of inspiration for our actuator design comes from research studying the swelling of polymer brushes.[128] Bumbu, *et al*. functionalized the top surfaces of a microcantilever array with PMMA polymer brushes, then placed the microcantilever array into a liquid cell in order to measure the response of the polymer brushes to solvents and non-solvents, as shown schematically in Figure 4.2. They used an optical lever system to measure the deflection of the microcantilevers, which was around 50-200 nm, depending on the solvent system in the liquid cell. Figure 4.3 shows the response of the microcantilevers to changes in the solvent system. In the areas labeled (1), the liquid cell is filled with isopropanol (2-PrOH), which is a non-solvent, and the Δd is roughly 0 nm, aside from some residual deflection after switching solvents. In the areas labeled (2), the cell is filled with a mixture of 2-PrOH and ethyl acetate (EtAc) that is 5% EtAc, which is a solvent. Even with such a small fraction of solvent, the polymer brushes swell enough to cause 50 nm of deflection. Lastly, in the areas labeled (3), the 2-PrOH has been replaced with 100% EtAc. In pure solvent, the polymer brushes swell enough to produced at least 200 nm of deflection. This method of actuating microcantilevers is capable of producing deflections that are an order of magnitude greater than the DNA hybridization demonstrated by Fritz, *et al*.

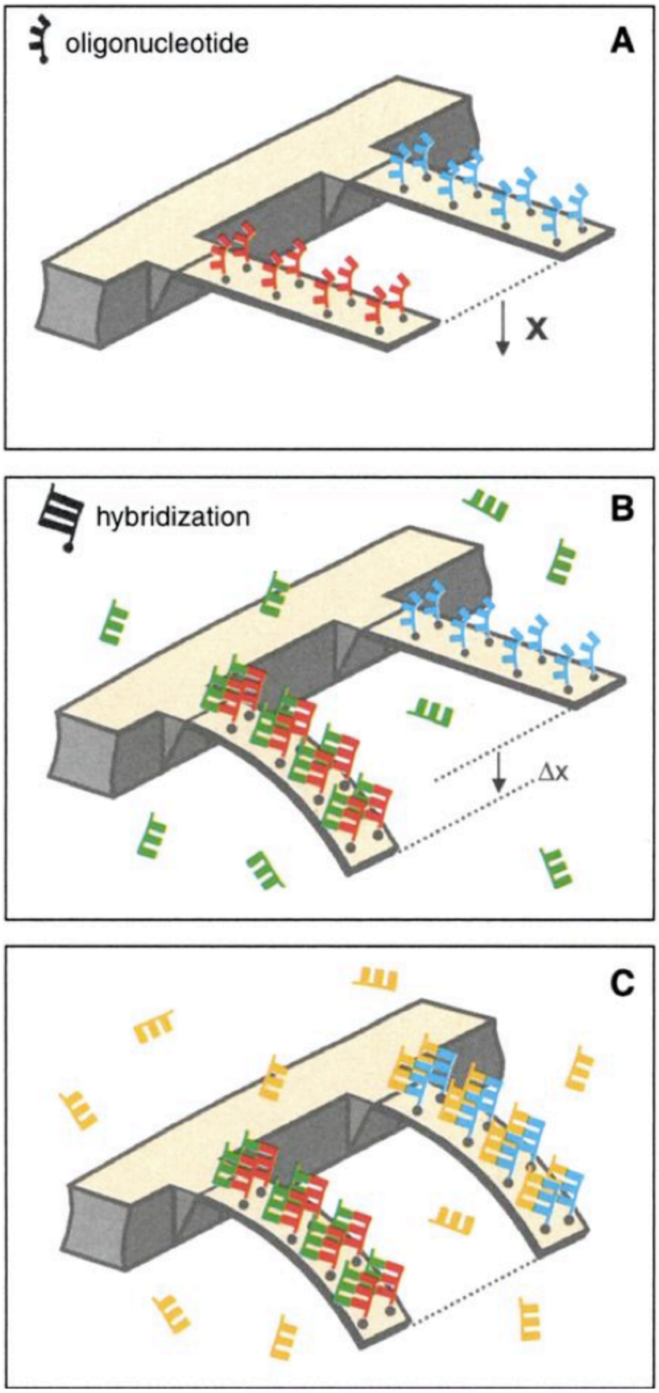

Figure 4.1: Schematic drawing of DNA hybridization experiments by Fritz, *et al*. Different hybridization possibilities are illustrated.

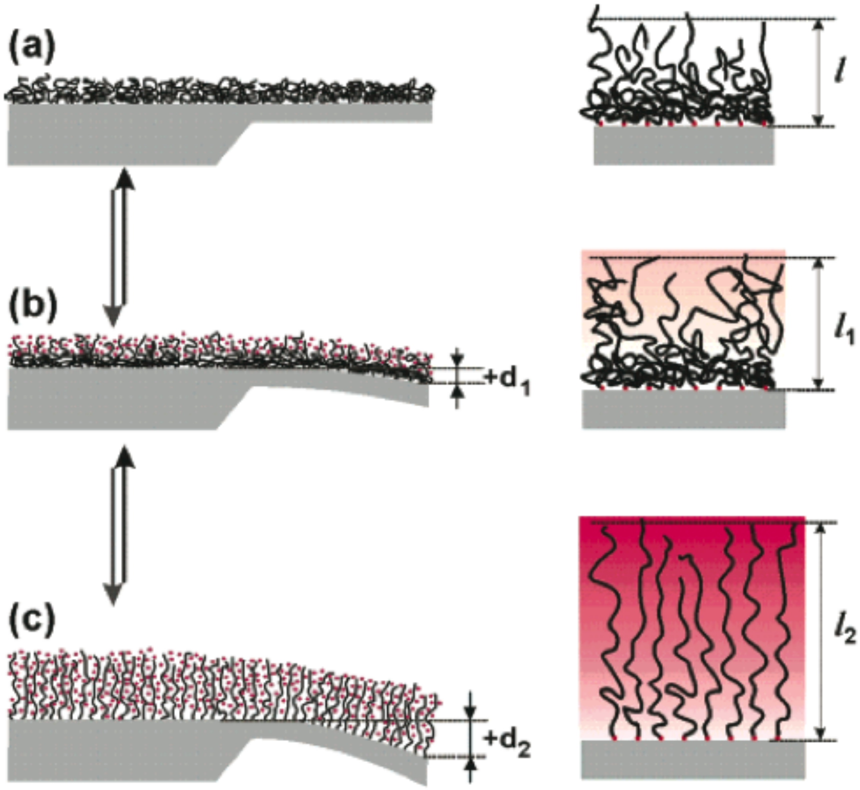

Figure 4.2: Schematic drawing of polymer brushes. (a) shows polymer brushes in a non-solvent, (b) shows polymer brushes in a mixture of solvent and non-solvent, and (c) shows polymer brushes in a solvent.

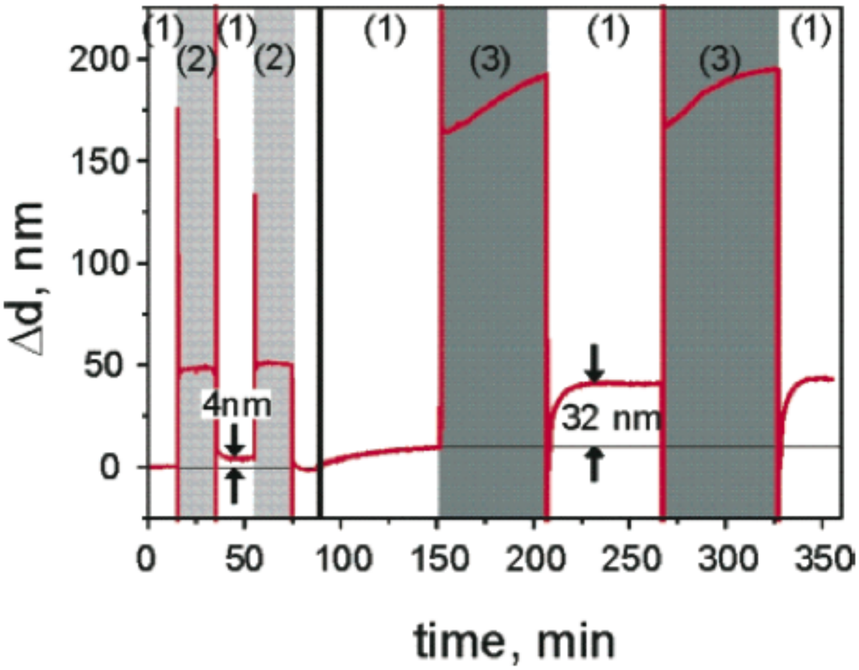

Figure 4.3: Deflection data for the swelling of polymer brushes in non-solvent (1), 5% solvent (2), and 100% solvent (3).

A more recent example[126] of microcantilever actuation used the reduction and oxidation of tethered ferrocene molecules, as shown schematically in Figure 4.4. Norman, *et al*. showed that the insertion of bulky ClO_4^- ions into a self-assembled monolayer of tethered ferrocenium (reduced ferrocenes) can generate surface stresses large enough to produce over 900 nm of microcantilever deflection. Figure 4.5 shows the response of the microcantilevers as the ferrocenes are electrochemically oxidized to ferrocenium, then reduced from ferrocenium back to ferrocene. In this example, the actuator response is on the order of 1 μm, which is roughly one order of magnitude greater than the swelling polymer brush example, and two orders of magnitude greater than the DNA hybridization example.

We believe that actuators based on aligned CNTs have the potential for even greater deflections. Recent work demonstrated making artificial muscles from aligned CNT sheets.[130] In this study, they charged up sheets of MWCNTs by applying a voltage. The repulsive force between the MWCNTs in the sheets caused them to fan out in two dimensions, while contracting in the third (see Figure 4.6). These 50 mm x 2 mm MWCNT actuators contract with high strength and have Poisson's ratios up to 15 when 5 kV is applied to the actuator. This work showed that electrostatic repulsion between CNTs can do macoscale work in the range of kV potentials.

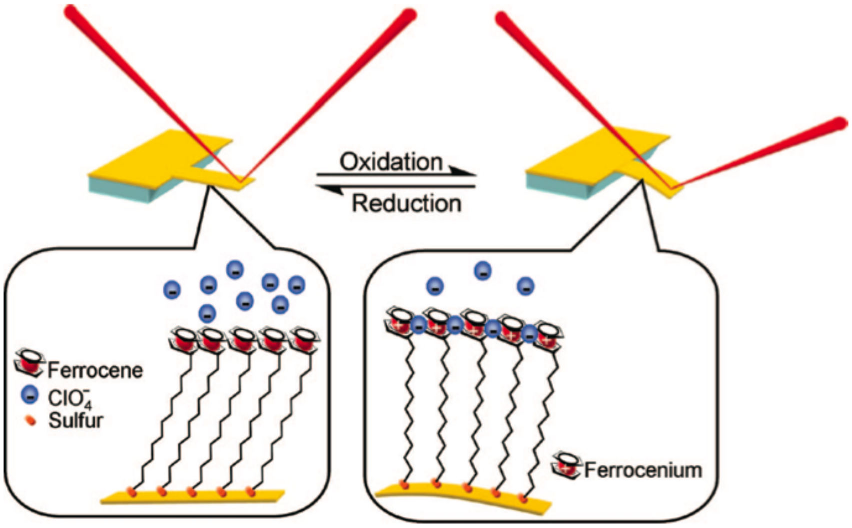

Figure 4.4: Schematic representation of a redox-based microcantilever actuator.

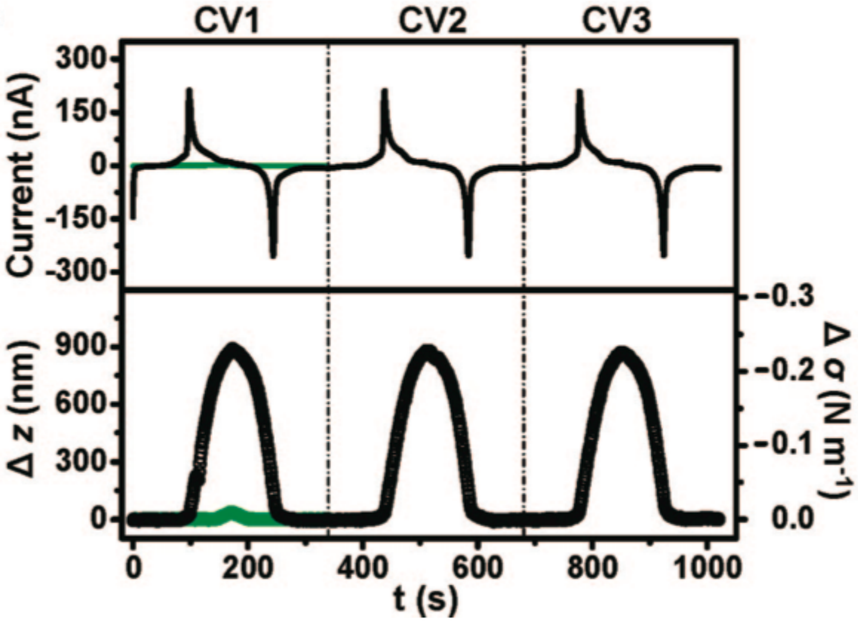

Figure 4.5: Deflection data from a redox-based microcantilever actuator. Deflections of nearly 1 µm are possible.

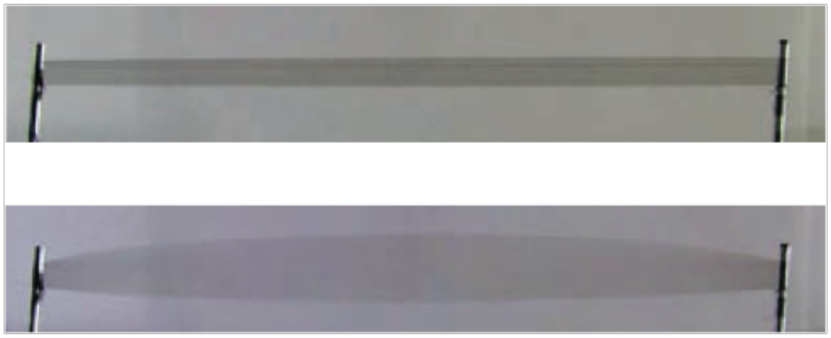

Figure 4.6: CNT aerogel muscles. The top image shows a MWCNT yarn stretched between two metal posts. The bottom image shows the expansion of the MWCNT yarn after applying a 5kV potential, relative to a counter electrode.

In our actuator design, we strive to combine the concept of differential surface stress based microcantilever actuators with CNT arrays that can be electrostatically modulated. Figure 4.7 shows a schematic diagram of our actuator design. We will grow a VA-CNT forest on top of the microcantilever, which will provide a means of force transduction to generate a surface stress on top of the microcantilever when we apply a voltage to the VA-CNT array. Our goal is to be able to achieve micron-scale deflections at significantly lower voltages than those used for CNT aerogel muscles.

The performance of a bimorph, such as a nanoelectromechanical actuator, relies on the ability to induce a difference in surface stresses on each side of a cantilever. This can be mathematically evaluated by using the Stoney formula.[131] More recent work has shown that the Stoney formula does not describe the behavior of microcantilever deflection well.[126,132,133] Grütter's group resolved this discrepancy by deriving a modified version of Hooke's law that defines the surface stress in terms of the spring constant, *k*, the deflection, Δz, Poisson's ratio, ν, and the geometry of the microcantilever. The relation between the deflection, Δz, and the change in surface stress, $\Delta\sigma$, was derived for rectangular microcantilevers

$$\Delta\sigma = \frac{4}{3(1-\nu)}\frac{l}{Wt}k_{rect}\Delta z$$

where W is the width of the microcantilever, *t* is the thickness, l is the length, and k_{rect} is the spring constant of the microcantilever.

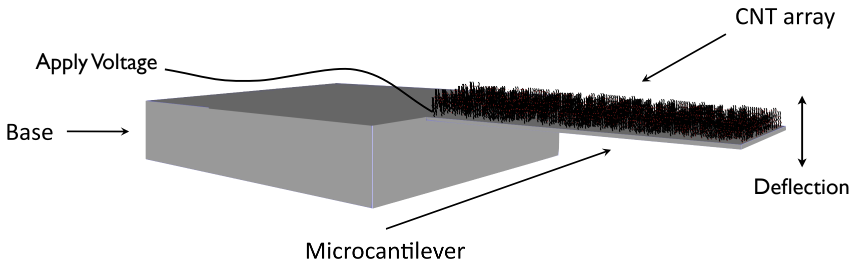

Figure 4.7: Schematic of our actuator design.

When studying the nanoelectromechanical actuator, it will be straightforward to quantify the induced surface stress using the above formula for deflections on the order of tens or hundreds of nm. Larger deflections violate the assumptions of the derivation of the above formula. For smaller deflections, the deflection, Δz, will be measured using an optical lever and a position sensitive device (PSD). Poisson's ratio will be taken as 0.064 for silicon microcantilevers.[126,133,134] Microcantilever spring constants and geometry are specified by the manufacturer and can be experimentally verified. For larger deflections (> 1μm), we will use an optical microscope with a high power objective to observe tip deflections directly.

To demonstrate feasibility of our actuator design, I did some computational modeling of a simplified system using COMSOL Multiphysics. My model had 45 SWCNTs (1 nm diameter, 40 nm long) on a 200 nm x 50 nm x 20 nm Si cantilever that is fixed at one end. The SWCNT spacing is 10 nm, which gives a reasonable areal density of ~0.01 SWCNT/nm^2.[135] Mechanical properties of the SWCNTs are based on data from the literature[5,6,136] and the SWCNTs are modeled as solid cylinders to reduce computational complexity. The SWCNTs have a space charge density corresponding to fewer than one electron per SWCNT. Initial simulations show almost a 1 nm deflection at the free end of the cantilever, which is 0.5% of the length of the 200 nm cantilever. Based on evidence in the literature, we expect that many more electrons (1 electron per 30-100 C atoms[4,117]) can be loaded onto each SWCNT, leading to larger deflections.

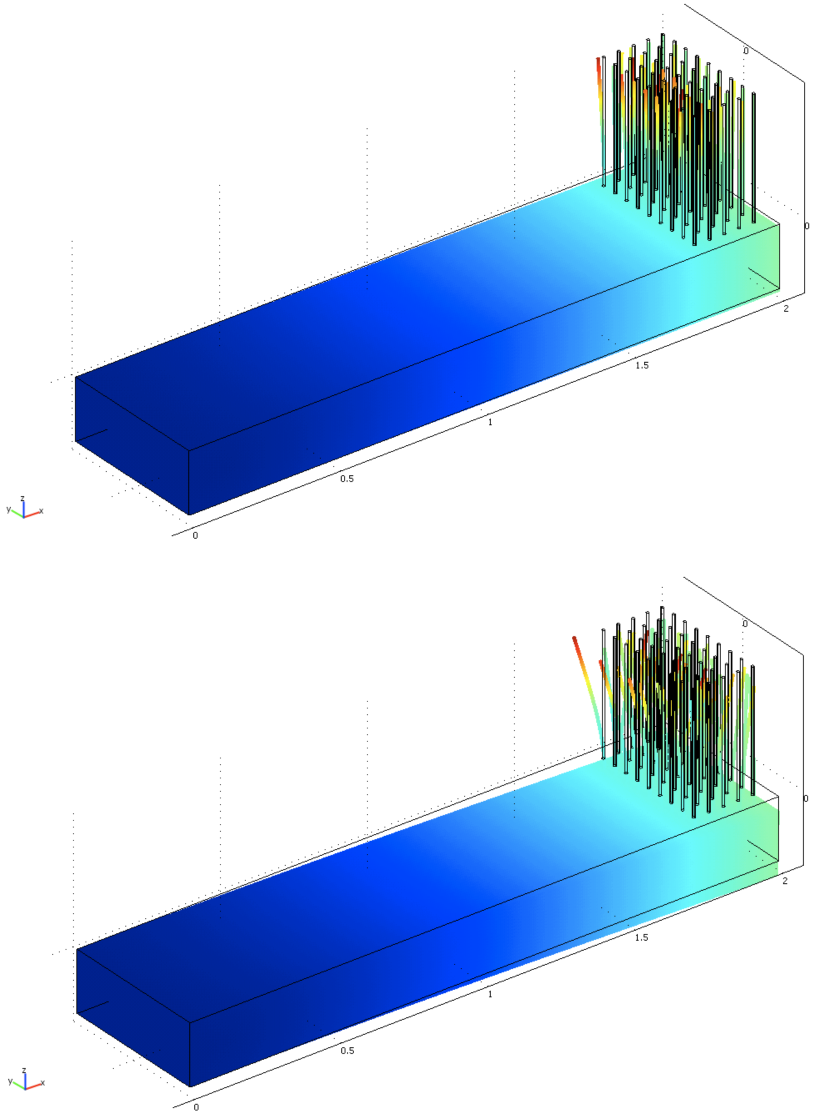

Figure 4.8: COMSOL modeling results. The color gradient indicates the magnitude of deformation, with red being maximal deformation. The top image is drawn to scale, whereas the deformation has been magnified 5x, for visual effect, in the bottom image.

4.2 Actuator Fabrication and Testing

4.2.1 First Generation

We are using a commercially available microcantilever array called the Octosensis to build our actuator systems, purchased through Micromotive Mikrotechnik in Germany. Each sample has eight microcantilevers measuring 500 μm x 90 μm x 1 μm, with a stiffness of ~23 mN/m. In the first generation actuators, we were still using Al as our catalyst support layer (30 nm Al / 1 nm Fe).

While using our original CVD system, we grew VA-MWCNTs on the first Octosensis chip that we tested. The VA-MWNTs were fairly well aligned, but the growth density was low, as shown in Figure 4.9. Unfortunately, the growth results were not reproducible, but we did measure electrostatically induced deflections after making electrical contact to the VA-MWCNT array using silver epoxy.

We have set up experimental apparatus that allows us to carefully control the charging/deflection of VA-CNT actuators. Figure 4.10 shows the equipment set up in our lab. The bottom image shows our control and measurement equipment, which includes an oscilloscope, lock-in amplifier, 1000 V power supply, and a home-built voltage controller that can amplify the lock-in amplifier's reference signal up to the full 1000 V provided by the power supply. We will hopefully not need such high voltages, but we have the capability if necessary.

When testing the actuator shown in Figure 4.9, we used the lock-in amplifier to drive charge sinusoidally on/off the actuator based on the reference signal, then locked onto the signal coming out of the PSD in response to charging/discharging of the VA-CNT array. We collected deflection data at several driving voltages for that actuator and a control sample that had undergone the same processing conditions, aside from the CNT growth. The data is shown in Figure 4.11. The output voltage shown in Figure 4.11 is the output signal from the PSD, as detected by the lock-in amplifier, taken at 100 Hz. That output signal has not been calibrated, but we estimated that we were measuring deflections on the order of 10 nm based on the output of the AFM's PSD.

After updating our CVD system, we started fabricating more actuators to do further testing of microcantilever deflections. A couple of the early actuators we fabricated demonstrated that the process of annealing Al/Fe coated microcantilevers and growing CNTs can generate quite large surface stresses. Figure 4.12 shows the highly curved microcantilevers. The top image shows the curvature of all eight cantilevers and the bottom image shows that the CNT growth is 1-2 μm of randomly aligned CNTs.

Raman spectroscopy verified that the randomly aligned CNTs were SWCNTs, as shown in Figure 4.13. To my amusement, measuring the Raman spectrum on the microcantilevers leads to a sinusoidal background signal due to laser interference with microcantilever array, which has a pitch of 250 μm. This interference is not present when taking Raman spectra of CNTs grown on the base of the Octosensis chips.

SEM images taken from the side allow measurement of microcantilever deflections, as shown in Figure 4.14. The SWCNT sample shown in Figure 4.14 is the same as the one shown in Figure 4.13. The control shown in Figure 4.14 underwent identical processing, except that the C_2H_4 feedstock was not added to the CVD gas stream during the "growth" phase. Both sample and control showed huge deflections of 190-260 μm, with a difference of about 65 μm.

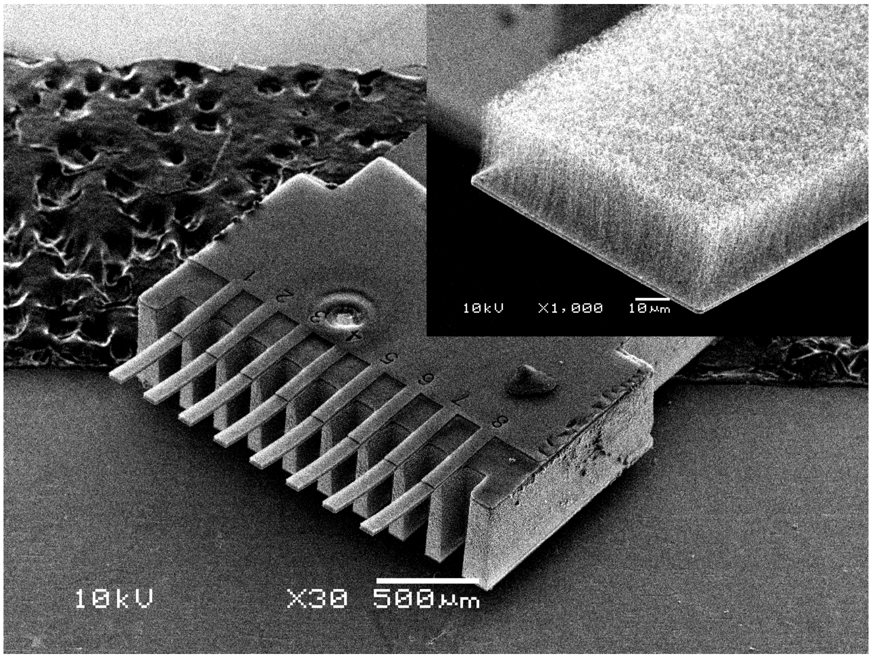

Figure 4.9: First Octosensis with VA-MWCNTs. The growth density was low, as shown in the inset, and the growth results were not repeatable.

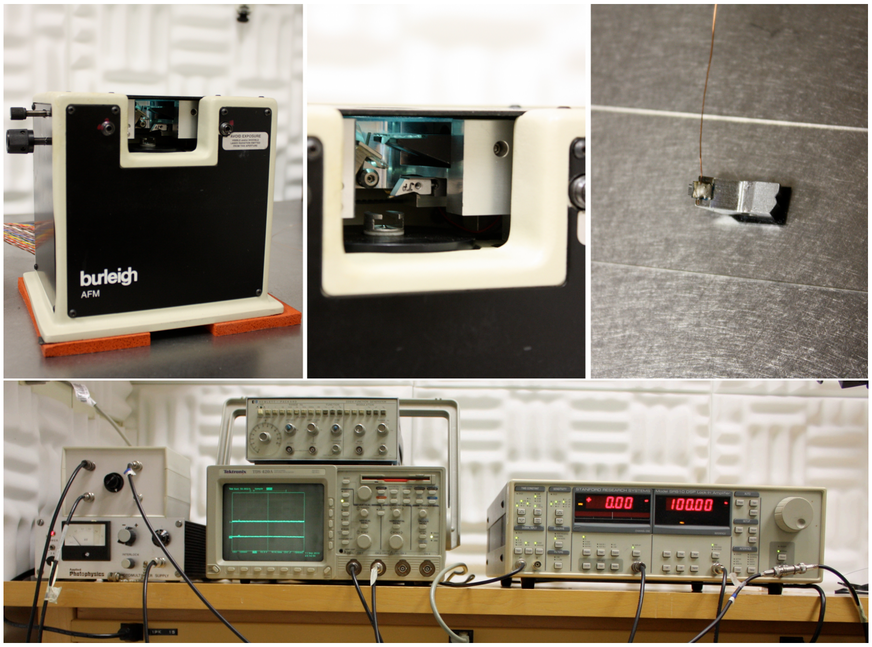

Figure 4.10: Experimental apparatus for measuring actuator deflections. Top left is a Burleigh AFM that is being used for its PSD system, top center is a close-up of the sample holder, top right is a test sample, and the bottom is our control and measurement equipment.

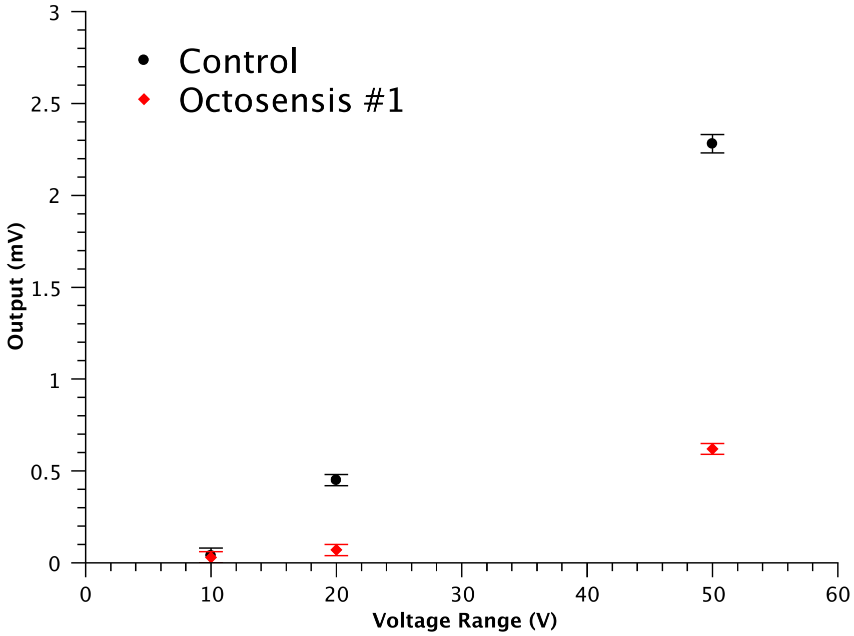

Figure 4.11: Deflection data collected from the first VA-MWCNT actuator. The deflection is represented by an uncalibrated voltage output from the lock-in amplifier.

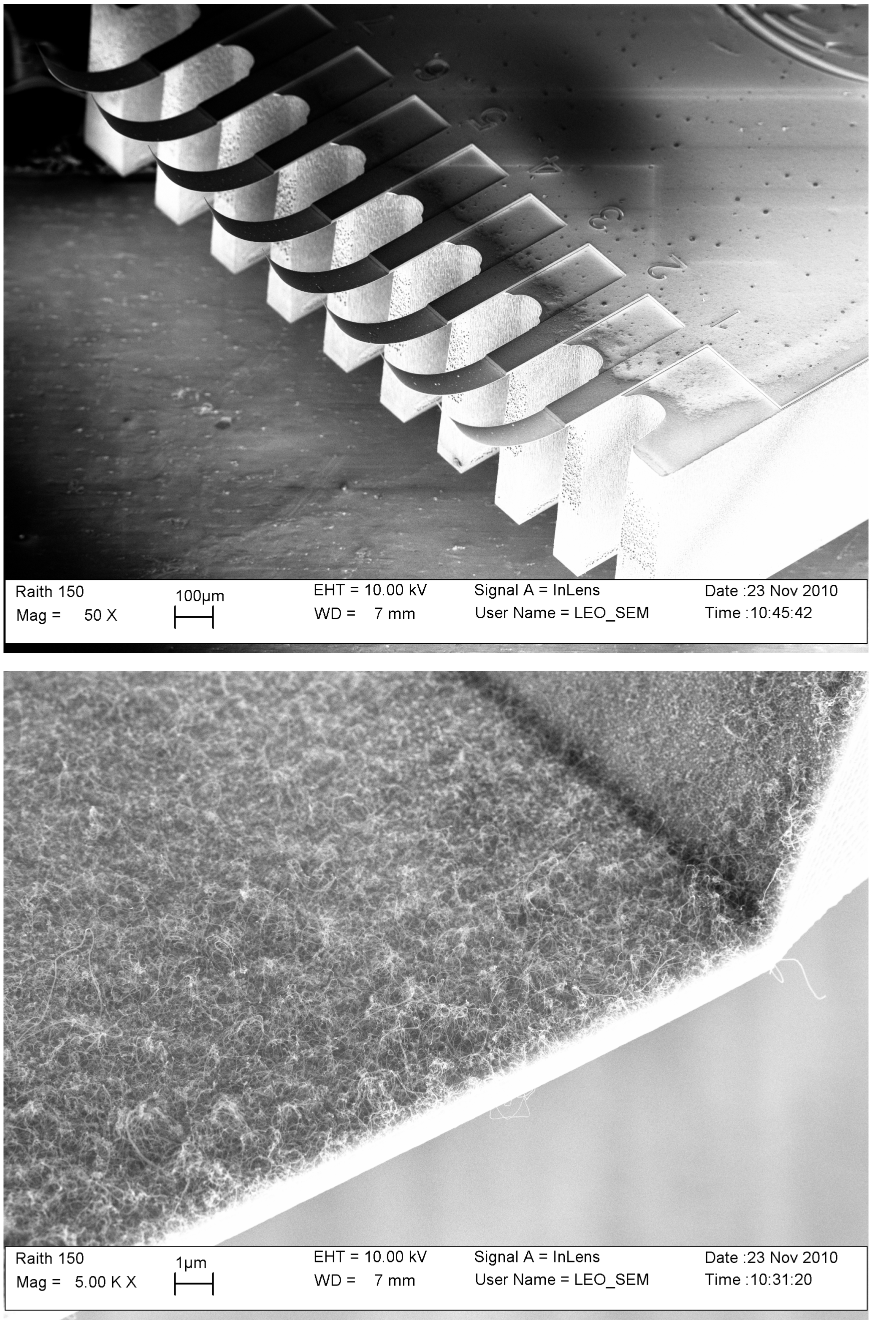

Figure 4.12: Early actuator fabrication, where extreme cantilever deflection occurred after CNT growth.

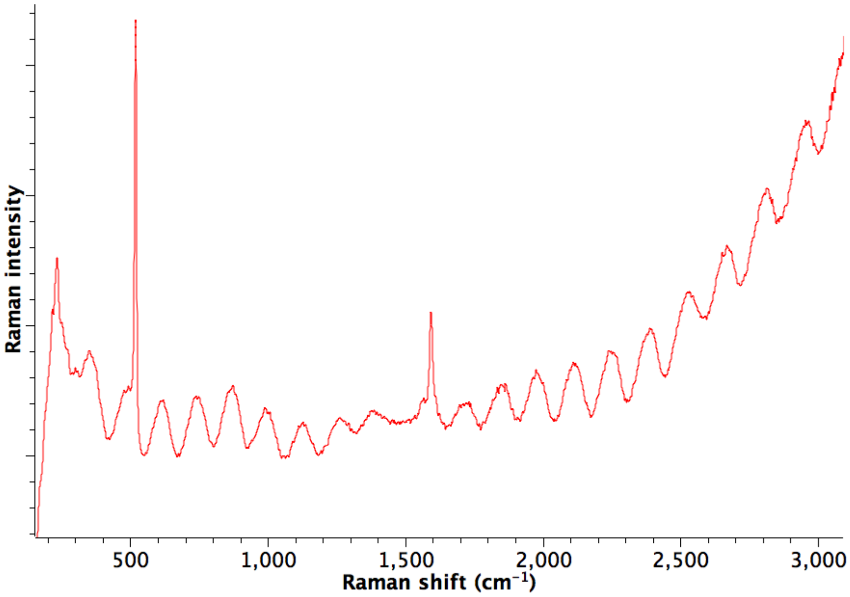

Figure 4.13: Raman spectrum of SWCNTs grown on top of an Octosensis actuator. The sharp G$^+$ peak at 1593 cm^{-1} and the RBMs at ~250 cm^{-1} show that SWCNTs were grown. The sinusoidal background signal is due to the Raman laser interfering with the microcantilever array.

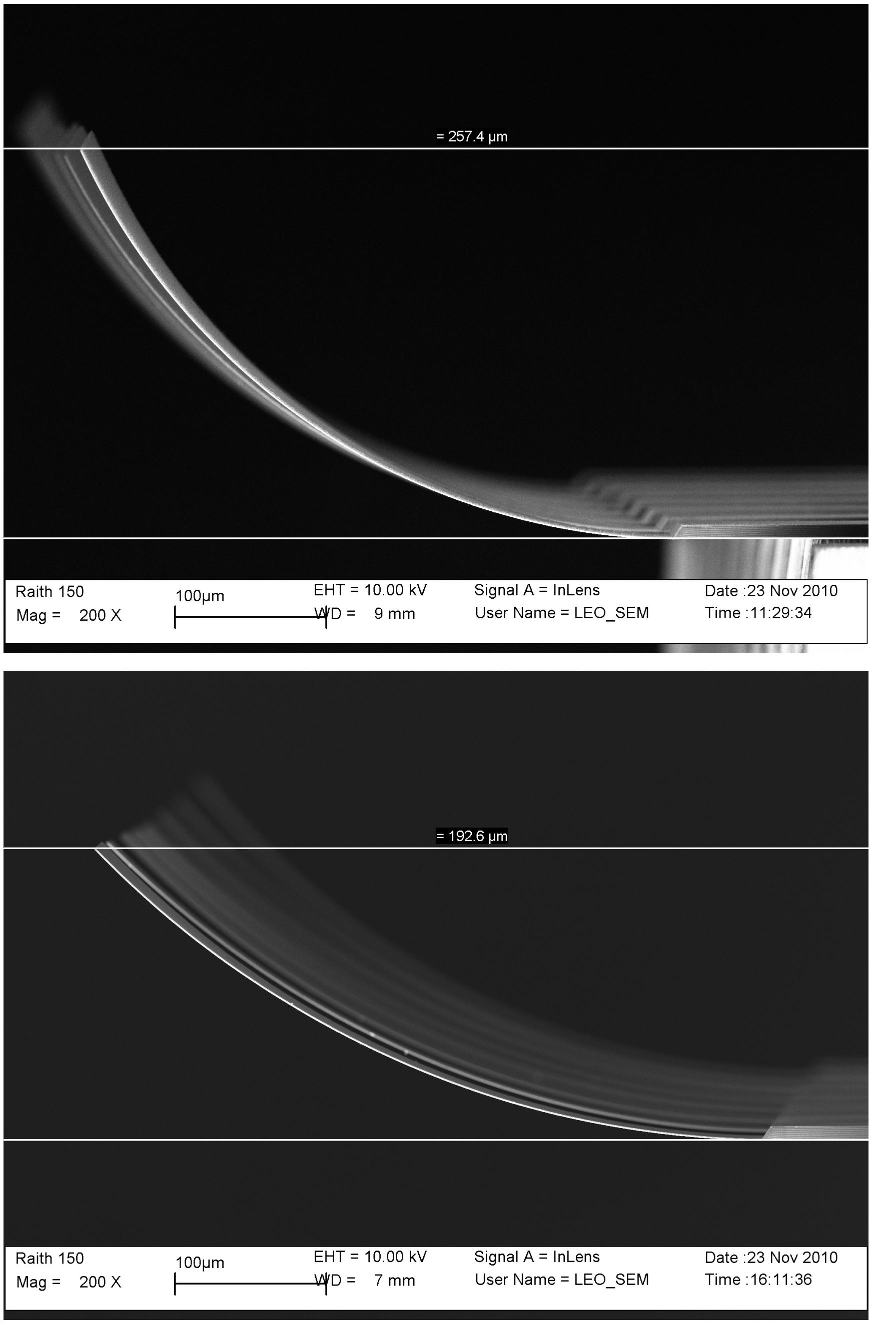

Figure 4.14: SEM measurements of microcantilever deflection after SWCNT growth (top) and microcantilever annealing without SWCNT growth (bottom). The sample with SWCNTs had microcantilever deflections of about 257 µm and the control had microcantilever deflections of about 193 µm.

Since the SWCNT sample had greater deflection, we suspected that the growing SWCNTs might be generating their own surface stress due to self-interactions and surface interactions. We assumed that the rest of the deflection came from surface stresses generated in the metal films. However, the manufacturer states that the microcantilevers are composed of laminated Si and SiO_2 layers, so we tested whether annealing an as-received Octosensis chip would lead to any deflection. Figure 4.15 shows that the microcantilevers are not bent before or after annealing at 750 ºC. Based on this experiment, it is clear that the large deflections in the previous experiments were due to the metal films rather than any stresses in the microcantilevers themselves.

Our next set of experiments was designed to learn more about the surface stresses generated at each step of fabrication. For these experiments we reduced the Al catalyst support layer to 20 nm. Two samples with 1 nm Fe and two with 2 nm Fe were fabricated, such that there was a sample and control for each Fe thickness. We measured the microcantilever deflections for all samples/controls before deposition, after deposition, after annealing (controls – no CNTs), and after CNT growth (samples). The results from these four samples/controls are summarized in Figure 4.16. During the Al/Fe deposition and annealing steps, it is clear that the 2 nm Fe sample has greater deflection than the 1 nm Fe sample. By contrast, the deflection during the CNT growth step is almost the same for the two Fe thicknesses. The reason for the growth induced deflection is not currently understood, but we believe it is either related to attractive interactions between growing CNTs or changes in the surface energy of the catalyst layer as a result of the dissolved carbon.

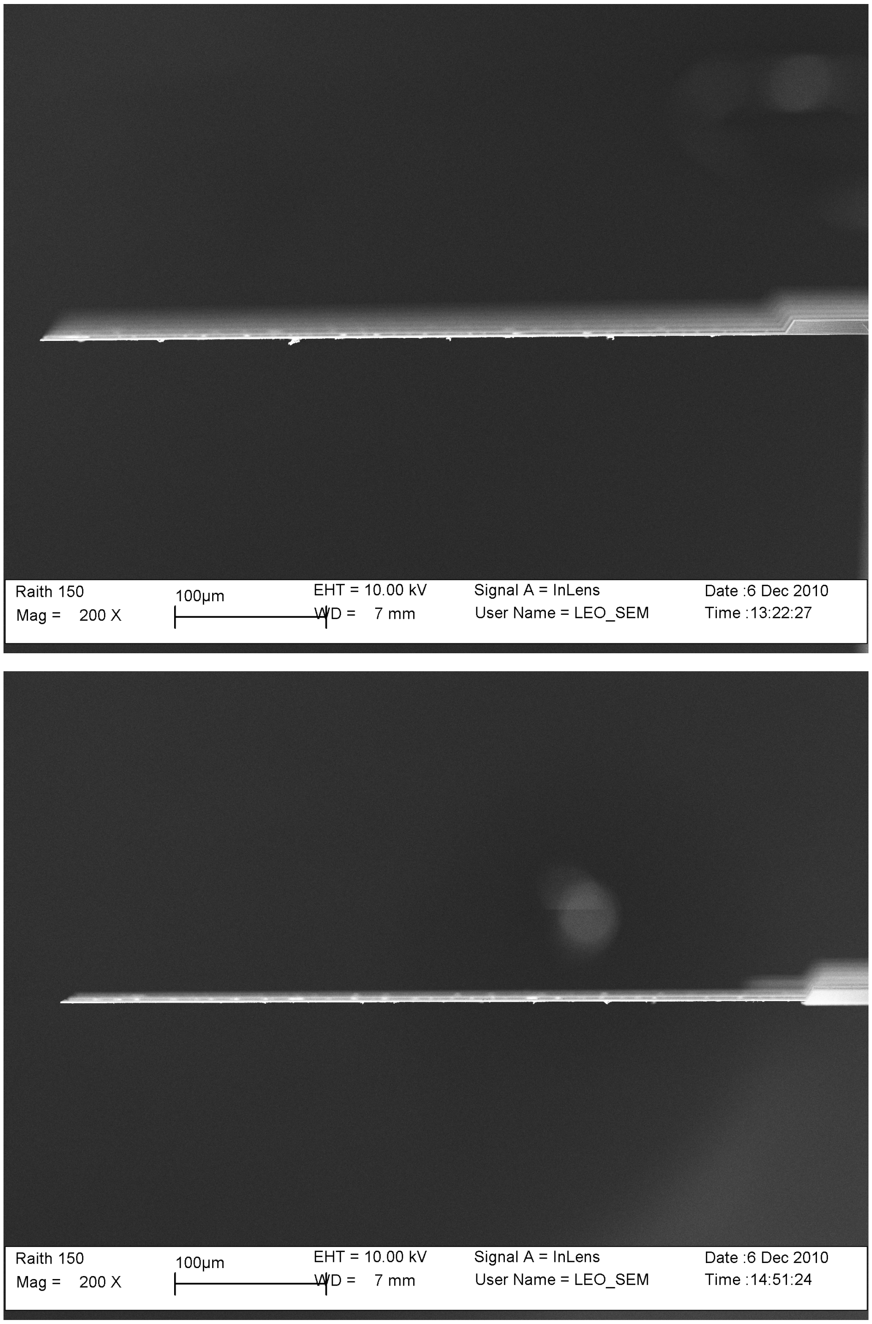

Figure 4.15: Thermal testing of as-received Octosensis. Top image is before annealing and bottom image is after annealing at 750 ºC.

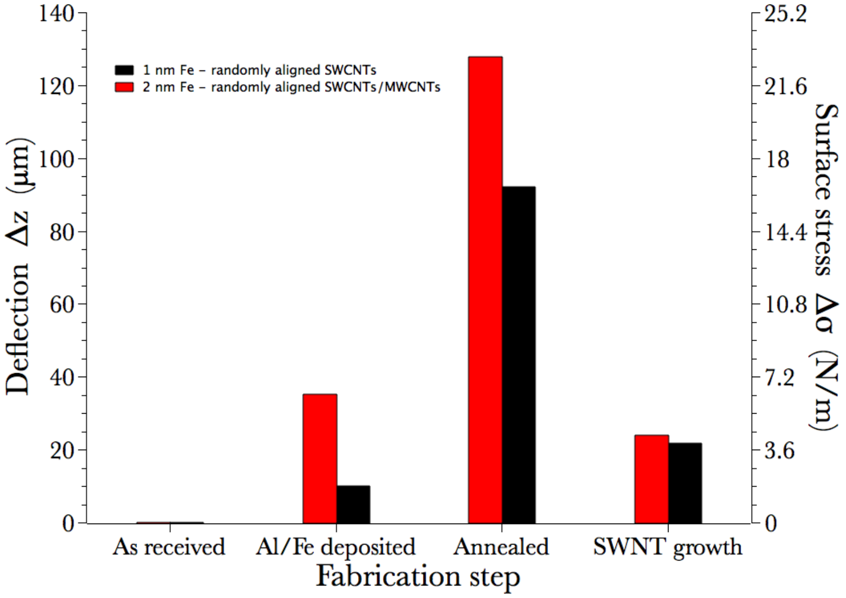

Figure 4.16: Microcantilever deflection, measured at each fabrication step. Two different Fe thicknesses were used and there was a control for each sample.

Similar to the previous experiments, CNT growth increases the positive deflection of the cantilevers and SEM shows 1-2 µm of randomly aligned CNTs. Raman spectra show that the 1 nm Fe sample is composed of predominantly SWCNTs and the 2 nm Fe sample has a mixture of SWCNTs/MWCNTs. It is clear from Figure 4.16 that most of the microcantilever deflection during fabrication comes from the deposition and annealing steps. It was at this point that we started carefully investigating potential sources of surface stress in the Al and Fe thin films that we deposit and discovered the hillocking mechanism of stress relief in Al films during annealing (see Section 2.4.4). Hillocking leads to a tensile stress upon cooling, which explains why the microcantilevers bend up so much after annealing and cooling down. Also, the significantly roughened surface morphology is detrimental to the growth of VA-CNTs.

4.2.2 Second Generation

After understanding the problems related to using Al as a catalyst support layer, we switched to an Al_2O_3 catalyst support layer, as described in Section 2.4.5. We next fabricated a new pair of sample/control actuators, depositing 1 nm Fe on 15 nm Al_2O_3 and using the same CNT growth protocol with 100 sccm C_2H_4 flow to ensure dense aligned growth. Figure 4.17 shows the highly aligned VA-CNTs that can be grown on second generation actuators when Al_2O_3 is used at the catalyst support layer. It is worth noting that the VA-CNT forest height in this sample increases towards the microcantilever tip, almost doubling in height compared to the microcantilever base (20-40 µm tall). Raman spectroscopy shows that the VA-CNTs are a mixture of SWCNTs and MWCNTs.

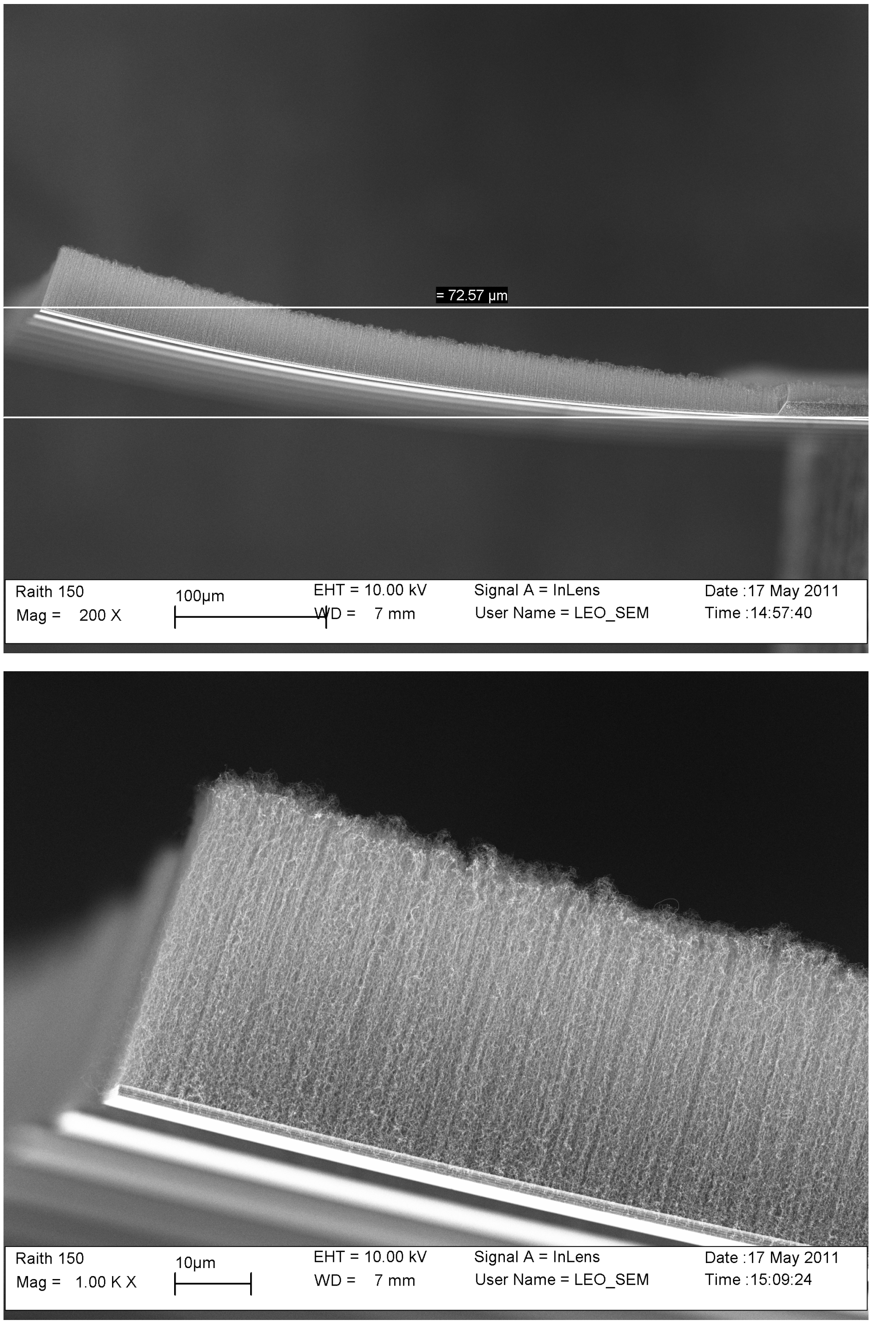

Figure 4.17: VA-CNT growth on second generation actuator. The top image shows that the post-growth deflection is about 1/3 the deflection in the first generation samples. The bottom image shows the well-aligned VA-CNTs at the microcantilever tip.

Another interesting observation about this actuator is that post-growth deflection is less than that of the control, which is the opposite from what was observed in the first generation actuators that had thin randomly aligned CNT arrays. We do not have experimental verification, but we believe that the tall CNT forest may be resisting the compression that results from the upward bending of the microcantilevers.

While studying these samples in the SEM, we realized that our VA-CNT forest may be interacting with the e-beam since CNTs are excellent electron acceptors. If this were the case, it would be excellent evidence to support the practicality of our actuator design. To test this hypothesis, we imaged our actuator in the SEM, varying the aperture size and accelerating voltage to look for changes in microcantilever deflection.

Varying the aperture size changes the beam current, which could affect the electron loading on the VA-CNT forest if the discharge rate is high enough to compete with the rate of electron absorption from the e-beam. We spanned the full range of aperture sizes on the Raith HR-SEM, from 7.5 µm to 120 µm, which covers a beam current range of 0.006 nA to 1.3 nA. Regardless of the aperture size, the microcantilever deflection did not change, indicating that deflection caused by interaction with the e-beam requires less than 0.006 nA beam current.

We next varied the accelerating voltage and found a strong dependence of the microcantilever deflection on the accelerating voltage. We measured deflections at 0.8-10 kV and found approximately 12 µm difference between 0.8 kV and 10 kV. After testing the actuator, we checked the control and found that it had a similar response, meaning that some other factor could be causing the deflection changes. To test this possibility, we measured microcantilever deflections of the actuator and control in an optical microscope to rule our any effects from the e-beam.

We plotted the SEM measured deflections for actuator and control, normalized by the deflection measured by the optical microscope, as shown in Figure 4.18. The optical microscope measurement was subtracted from all deflection measurements, making it a 0 μm deflection at 0 kV. Strikingly, all the deflections for the control are negative and all the deflections for the actuator are positive. In fact, across the entire range of measurements, the difference between the actuator and control is 15.9 ± 0.3 μm. This data strongly suggests that the e-beam is interacting with the VA-CNT forest and causing the microcantilevers to deflect.

We believe that the large variation in deflections across the 0.8-10 kV range is an artifact due to a retarding potential at the end of the SEM column. The e-beam travels down the SEM column at 10 kV, but must be slowed down for imaging at sub-10kV accelerating voltages. Fringe effects from the retarding potential are most likely interacting with the soft microcantilevers. At 10 kV, the deflections measured by SEM and optical microscopy agree for the control, supporting this hypothesis.

The deflection results from our first generation actuator have shown that we can measure deflections using our AFM-based testing apparatus. Our surface stress experiments have highlighted the importance of controlling and understanding the surface stresses that are generated during each processing step. The microscopy results from our second generation actuators have shown conclusively that VA-CNTs grown on microcantilevers can have a large electromechanical response, which is crucial for the advancement of this project.

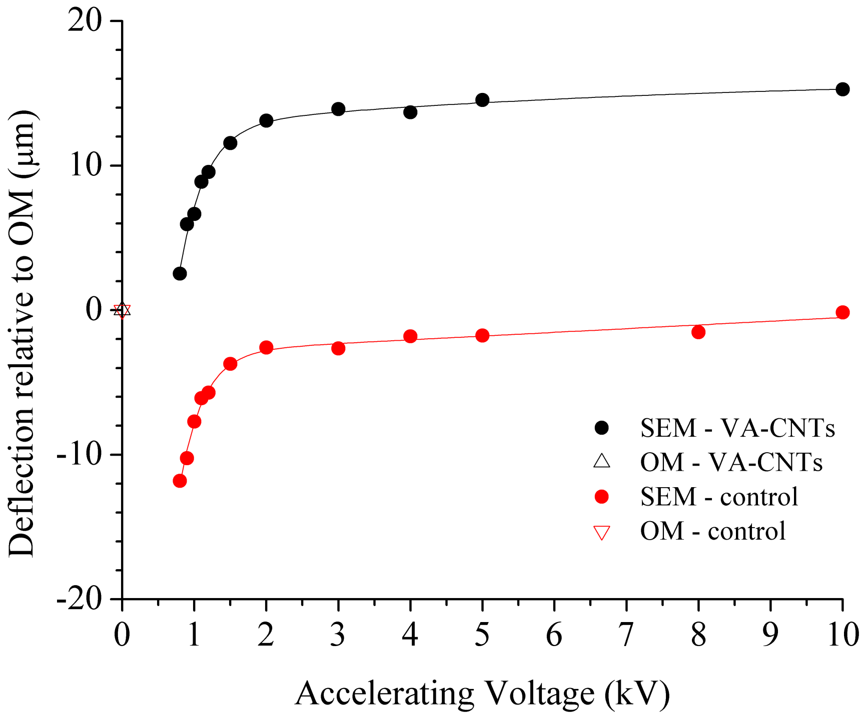

Figure 4.18: Actuator and control deflections, relative to the optical microscope measurement. The actuator is consistently 16 µm more deflected than the control.

4.3 Future Work

The techniques necessary to grow VA-CNTs onto Octosensis microcantilever arrays have been developed, but we need to gain more understanding about the surface stresses that result from annealing and VA-CNT growth in order to make better actuators. The immediate next step is to fabricate several more pairs of actuators/controls to test and better understand the growth-induced deflection. We will grow samples with shorter VA-CNTs to see how the post-growth deflection is affected. The second generation actuator described above was fabricated with a 10 min growth phase, so we will make samples with 5 min, 2 min, and 1 min growth. These samples will be fully characterized by Raman, SEM, and optical microscopy and the results will be compared to the results above.

4.3.1 Electrostatic Actuation

4.3.1.1 Deflection Measurement by Optical Lever

After the spectroscopic and microscopic characterization of the actuator samples with varying VA-CNT forest heights, a full set of VA-CNT forest parameters will be characterized in terms of actuator deflection. We will deposit a thin Ti layer on the base of the Octosensis chips to make electrical contact with the VA-CNT forest. Ti has been shown to wet CNTs, allowing good electrical contact.[137,138] If desired, an Au layer could be deposited on top of the Ti layer to allow a wirebonded connection to a separate contact pad. The deflection of microcantilevers will be measured by optical lever, where a laser is reflected off the back of the microcantilever and measure deflections with a quad cell position sensitive diode. Some preliminary actuator deflection data were presented in

Section 4.2.1, but we will now be able to study a series of samples that have been fabricated with significantly greater control. The four sets of samples will have different VA-CNT forest heights and will give us more information about the electrostatically driven deflections that we measure.

The maximum electron loading will scale linearly with the height of the CNT array, but it is not obvious whether the deflection will also scale linearly. Even VA-CNTs are somewhat tangled and the flexible geometry makes it difficult to model. We will measure the deflection dependence on VA-CNT height and carefully interpret any variations from linearity.

A second study will compare the microcantilever deflection between small (10-20 nm) and large (50-100 nm) diameter MWCNTs of the same height. We will make another set of actuator samples that are composed of varying MWCNT diameters, as controlled by the Fe catalyst thickness. Small diameter MWCNTs will be more flexible and able to rearrange themselves to minimize repulsion. Large diameter MWCNTs will have a higher electron loading capacity, which could allow higher repulsive forces between adjacent MWCNTs. However, the large diameter MWCNTs have a lower areal density and consequently fewer and weaker tube-tube repulsions.

Studying the dependence of microcantilever deflection on CNT length and type will provide a set of calibration curves relating deflection to electron loading. For a given applied voltage, we can measure the amount of charge stored in the CNTs. Relating this value to the amount of deflection allows one to calculate the induced stress and an average force between adjacent CNTs.[126] Not only will this provide a valuable understanding of the interactions between CNTs and the surface stress on the microcantilever, but it will also provide a tool for analyzing the performance of other CNT-based actuators.

4.3.1.2 Deflection Measurement by Optical Microscope

Based on the preliminary data on the large deflections (16 µm) that can be caused by interactions with the SEM e-beam, we anticipate that our VA-CNT actuators will be capable of generating deflections on the order of 10 µm. If so, our microcantilever-based actuators would be able to bend one order of magnitude more than the redox actuators, two orders of magnitude more than the polymer brush actuators, and three orders of magnitude more than from DNA hybridization (see Section 4.1).

Such large deflections cannot be measured using our Burleigh AFM optical lever system, but are large enough for us to measure using a high-magnification objective in an optical microscope. We will test all of the actuator devices fabricated in the previous section at higher voltages and measure deflections by optical microscopy to find the limits of our nanoelectromechanical actuators. We anticipate that these actuators will outperform the literature examples described above.

4.3.2 Actuation by Optical Excitation of Ru Coordination Complexes

Another exciting possibility is to modulate VA-CNT actuators by optical excitation rather than applying a voltage to the system. We hypothesize that CNT arrays can be charged and deflected simply by shining light onto the array, if it has been functionalized with electron donating Ru coordination complexes (see Figure 4.19). Computational and spectroscopic research in the group has shown that optical excitation at the MLCT band can lead to charge transfer to SWCNTs, probably through the tpphz bridge.[103,139]

Our research has also shown good evidence for the mechanical docking of Ru decamer complexes to certain chirality SWCNTs.[103] Smaller Ru complexes, such as dimers, are easier to synthesize and have similar structural and electronic properties to the decamer. An advantage of using the Ru dimers is that they will bind more easily to MWCNTs than the Ru decamer, which has more restrictive binding sites. Additionally, we have the ability to synthesize Ru dimers with +2, +3, and +4 charge states, which impacts how they interact with the CNTs.

Binding +2, +3, and +4 Ru dimers to CNT arrays offers another novel way to actuate microcantilevers, as shown in Figure 4.20, and should provide useful insights into the electronic interactions between the dimers and CNTs. Illuminating the sample at the MLCT band (~450 nm) should push charge onto the CNTs temporarily, until the system relaxes. As long as that relaxation time is long enough or the photon flux is high enough, an equilibrium should form where the CNTs hold an additional charge distribution.

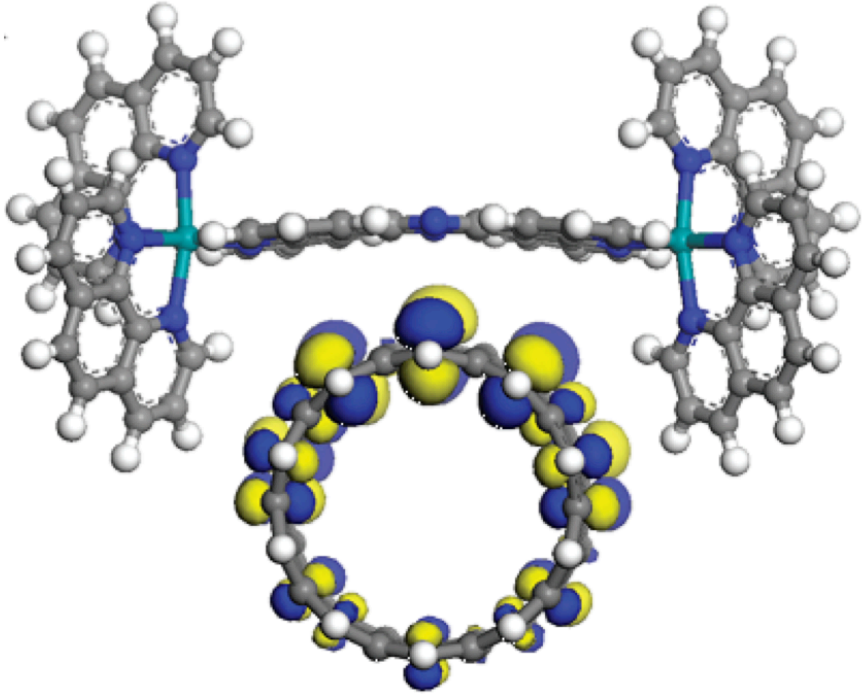

Figure 4.19: Computer model of a Ru dimer bound to a SWCNT, shown looking down the axis of the SWCNT. DFT modeling indicates a sharing of electron density near the tpphz bridge of the Ru dimer.

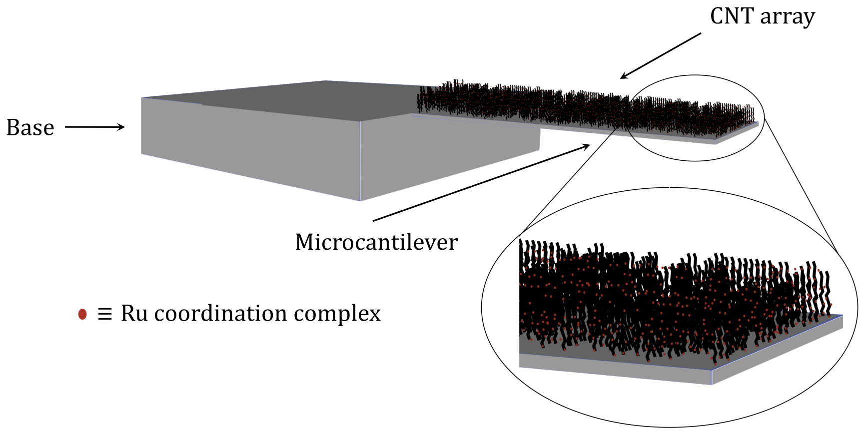

Figure 4.20: Schematic of a microcantilever with a Ru functionalized forest of CNTs grown on top. The CNT array has been functionalized with the Ru coordination complexes that are synthesized in our group.

The calibration curves generated in the previous stage of research will provide insight into the dynamics of this dimer-CNT system. It will be possible to study the electronic loading of the system as a function of light intensity by monitoring the deflection of the microcantilever. The relaxation of the system can then be studied by measuring the rate at which the microcantilever returns to its un-flexed state. The results from these experiments should vary depending on whether the +2, +3, or +4 Ru dimers are used, which will yield a useful study and comparison of the differences in how these dimer-CNT systems interact.

CHAPTER 5: CONCLUSION

The research in this Ph.D. dissertation covered the full spectrum of carbon nanotube research, including CNT growth, SWCNT dispersion stability, and the fabrication of novel nanoelectromechanical actuators. Each of these areas was studied in detail, as described in the previous chapters.

The research presented in this dissertation has made important contributions to the field of CNT dispersion stability in several areas. First, we discovered that ultrasonication of polar aprotic solvents with methyl substituents can lead to the formation of methyl hydroperoxide under certain conditions. The reaction mechanism is an autoxidation reaction that depends on temperature and dissolved oxygen concentration. This result is significant for scaling up dispersion of pristine SWCNTs and other nanomaterials in these solvents.

We next studied dispersion stability at the "onset of aggregation", where SWCNT dispersions are destabilized in 2 days by ionic coagulants that have been added to the dispersion. We found that dispersing SWCNTs into a 50/50 mixture of DMF and NMP could increase dispersion stability by up to 115%. The enhanced stability was a result of optimizing the dispersive Hansen parameter, which is a bulk solvent property. We provided a physical model, based on Maxwell–Boltzmann statistics and DLVO theory, which explained the sigmoidal aggregation profile that we observed.

After studying the "onset of aggregation", we measured true CCCs, as defined by DLVO theory. We developed a sedimentation technique to sediment aggregated

SWCNTs as the aggregates form, then measured the SWCNT concentration remaining after the simultaneous aggregation/centrifugation. These experiments were done with monovalent and divalent salts to check the Schulze–Hardy dependence of the CCCs. Three solvent systems were used to compare with "onset of aggregation" data: DMF, DMF/NMP, and NMP. In these experiments, we observed a "transient stability" effect in dispersions that contained NMP, as predicted by recent computational work.

A CVD system was build for the purpose of growing CNTs. After equipment upgrades, improved sample preparation, and growth protocol refinement, methods were developed to grow VA-CNT arrays on Si chips and Octosensis microcantilever arrays. Our ability to grown CNTs with well defined length will be crucial for future projects in the group, and the ability to grow VA-CNTs enables the development of nanoelectromechanical actuators.

The actuators we are developing will hopefully provide an important contribution to the field of microcantilever actuation by differential surface stress. Preliminary results are promising and suggest that we may be able to outperform similar actuator systems that have been published in the literature. Large displacement in these types of actuators would provide an advance that could lead to better manipulation of matter in the nano/micro regime. These actuators could be used for applications such as nano-manipulators, nano-valves, or drug release mechanisms. Also, basic knowledge about the interactions of charged VA-CNT arrays on microcantilevers will be obtained. Further, future work will provide insight into the electronic interactions between CNTs and Ru coordination complexes by interpreting the mechanical response of an optically modulated actuator system.

REFERENCES

1. Iijima, S. Helical Microtubules of Graphitic Carbon *Nature* **1991**, *354*, 56-58.

2. Dresselhaus, M. S.; Dresselhaus, G.; Jorio, A. Unusual properties and structure of carbon nanotubes *Annu. Rev. Mater. Res.* **2004**, *34*, 247-278.

3. Javey, A.; Guo, J.; Wang, Q.; Lundstrom, M.; Dai, H. J. Ballistic carbon nanotube field-effect transistors *Nature* **2003**, *424*, 654-657.

4. Kongkanand, A.; Kamat, P. V. Electron storage in single wall carbon nanotubes. Fermi level equilibration in semiconductor-SWCNT suspensions *ACS Nano* **2007**, *1*, 13-21.

5. Krishnan, A.; Dujardin, E.; Ebbesen, T. W.; Yianilos, P. N.; Treacy, M. M. J. Young's modulus of single-walled nanotubes *Phys. Rev. B: Condens. Matter* **1998**, *58*, 14013-14019.

6. Natsuki, T.; Tantrakarn, K.; Endo, M. Effects of carbon nanotube structures on mechanical properties *Appl. Phys. A: Mater. Sci. Process.* **2004**, *79*, 117-124.

7. Salvetat, J. P.; Briggs, G. A. D.; Bonard, J. M.; Bacsa, R. R.; Kulik, A. J.; Stockli, T.; Burnham, N. A.; Forro, L. Elastic and shear moduli of single-walled carbon nanotube ropes *Phys. Rev. Lett.* **1999**, *82*, 944-947.

8. Huang, J. Y.; Chen, S.; Wang, Z. Q.; Kempa, K.; Wang, Y. M.; Jo, S. H.; Chen, G.; Dresselhaus, M. S.; Ren, Z. F. Superplastic carbon nanotubes *Nature* **2006**, *439*, 281-281.

9. Saito, R.; Fujita, M.; Dresselhaus, G.; Dresselhaus, M. S. Electronic structure of chiral graphene tubules *Appl. Phys. Lett.* **1992**, *60*, 2204-2206.

10. Forney, M. W.; Poler, J. C. Sonochemical Formation of Methyl Hydroperoxide in Polar Aprotic Solvents and Its Effect on Single-Walled Carbon Nanotube Dispersion Stability *J. Am. Chem. Soc.* **2010**, *132*, 791-797.

11. de Heer, W. A.; Bacsa, W. S.; Chatelain, A.; Gerfin, T.; Humphreybaker, R.; Forro, L.; Ugarte, D. Aligned Carbon Nanotube Films - Production and Optical and Electronic-Properties *Science* **1995**, *268*, 845-847.

12. Lee, C. J.; Kim, D. W.; Lee, T. J.; Choi, Y. C.; Park, Y. S.; Lee, Y. H.; Choi, W. B.; Lee, N. S.; Park, G. S.; Kim, J. M. Synthesis of aligned carbon nanotubes using thermal chemical vapor deposition *Chem. Phys. Lett.* **1999**, *312*, 461-468.

13. de Heer, W. A.; Chatelain, A.; Ugarte, D. A Carbon Nanotube Field-Emission Electron Source *Science* **1995**, *270*, 1179-1180.

14. Koehne, J.; Li, J.; Cassell, A. M.; Chen, H.; Ye, Q.; Ng, H. T.; Han, J.; Meyyappan, M. The fabrication and electrochemical characterization of carbon nanotube nanoelectrode arrays *J. Mater. Chem.* **2004**, *14*, 676-684.

15. Wang, J. Carbon-nanotube based electrochemical biosensors: A review *Electroanalysis* **2005**, *17*, 7-14.

16. Fan, S. S.; Chapline, M. G.; Franklin, N. R.; Tombler, T. W.; Cassell, A. M.; Dai, H. J. Self-oriented regular arrays of carbon nanotubes and their field emission properties *Science* **1999**, *283*, 512-514.

17. Xie, S. S.; Chang, B. H.; Li, W. Z.; Pan, Z. W.; Sun, L. F.; Mao, J. M.; Chen, X. H.; Qian, L. X.; Zhou, W. Y. Synthesis and characterization of aligned carbon nanotube arrays *Adv. Mater.* **1999**, *11*, 1135-+.

18. Rohmund, F.; Falk, L. K. L.; Campbell, E. E. B. A simple method for the production of large arrays of aligned carbon nanotubes *Chem. Phys. Lett.* **2000**, *328*, 369-373.

19. Avigal, Y.; Kalish, R. Growth of aligned carbon nanotubes by biasing during growth *Appl. Phys. Lett.* **2001**, *78*, 2291-2293.

20. Shiratori, Y.; Hiraoka, H.; Takeuchi, Y.; Itoh, S.; Yamamoto, M. One-step formation of aligned carbon nanotube field emitters at 400 degrees C *Appl. Phys. Lett.* **2003**, *82*, 2485-2487.

21. Singh, C.; Shaffer, M. S.; Windle, A. H. Production of controlled architectures of aligned carbon nanotubes by an injection chemical vapour deposition method *Carbon* **2003**, *41*, 359-368.

22. Wei, B. Q.; Vajtai, R.; Jung, Y.; Ward, J.; Zhang, R.; Ramanath, G.; Ajayan, P. M. Assembly of highly organized carbon nanotube architectures by chemical vapor deposition *Chem. Mater.* **2003**, *15*, 1598-1606.

23. Jeong, S. H.; Lee, O. J.; Lee, K. H.; Oh, S. H.; Park, C. G. Preparation of aligned carbon nanotubes with prescribed dimensions: Template synthesis and sonication cutting approach *Chem. Mater.* **2002**, *14*, 1859-1862.

24. Parthangal, P. M.; Cavicchi, R. E.; Zachariah, M. R. A generic process of growing aligned carbon nanotube arrays on metals and metal alloys *Nanotechnology* **2007**, *18*.

25. Islam, M. F.; Rojas, E.; Bergey, D. M.; Johnson, A. T.; Yodh, A. G. High weight fraction surfactant solubilization of single-wall carbon nanotubes in water *Nano Lett.* **2003**, *3*, 269-273.

26. Hu, M. H.; Murakami, Y.; Ogura, M.; Maruyama, S.; Okubo, T. Morphology and chemical state of Co-Mo catalysts for growth of single-walled carbon nanotubes vertically aligned on quartz substrates *J. Catal.* **2004**, *225*, 230-239.

27. Maruyama, S.; Einarsson, E.; Murakami, Y.; Edamura, T. Growth process of vertically aligned single-walled carbon nanotubes *Chem. Phys. Lett.* **2005**, *403*, 320-323.

28. Zhang, L.; Tan, Y. Q.; Resasco, D. E. Controlling the growth of vertically oriented single-walled carbon nanotubes by varying the density of Co-Mo catalyst particles *Chem. Phys. Lett.* **2006**, *422*, 198-203.

29. Koizumi, T.; Ikedai, M.; Takagi, D.; Chiashi, S.; Rokuta, E.; Oshima, C.; Homma, Y. Direct growth of vertically aligned single-walled carbon nanotubes on metal tip by applying electric field *Japanese Journal of Applied Physics Part 1-Regular Papers Brief Communications & Review Papers* **2007**, *46*, 6087-6090.

30. Noda, S.; Hasegawa, K.; Sugime, H.; Kakehi, K.; Zhang, Z. Y.; Maruyama, S.; Yamaguchi, Y. Millimeter-thick single-walled carbon nanotube forests: Hidden role of catalyst support *Japanese Journal of Applied Physics Part 2-Letters & Express Letters* **2007**, *46*, L399-L401.

31. Nozaki, T.; Ohnishi, K.; Okazaki, K.; Kortshagen, U. Fabrication of vertically aligned single-walled carbon nanotubes in atmospheric pressure non-thermal plasma CVD *Carbon* **2007**, *45*, 364-374.

32. Iwasaki, T.; Zhong, G. F.; Aikawa, T.; Yoshida, T.; Kawarada, H. Direct evidence for root growth of vertically aligned single-walled carbon nanotubes by microwave plasma chemical vapor deposition *J. Phys. Chem. B* **2005**, *109*, 19556-19559.

33. Zhong, G. F.; Iwasaki, T.; Honda, K.; Furukawa, Y.; Ohdomari, I.; Kawarada, H. Low temperature synthesis of extremely dense, and vertically aligned single-walled carbon nanotubes *Japanese Journal of Applied Physics Part 1-Regular Papers Short Notes & Review Papers* **2005**, *44*, 1558-1561.

34. Zhong, G. F.; Iwasaki, T.; Kawarada, H. Semi-quantitative study on the fabrication of densely packed and vertically aligned single-walled carbon nanotubes *Carbon* **2006**, *44*, 2009-2014.

35. Futaba, D. N.; Goto, J.; Yasuda, S.; Yamada, T.; Yumura, M.; Hata, K. General Rules Governing the Highly Efficient Growth of Carbon Nanotubes *Adv. Mater.* **2009**, *21*, 4811-4815.

36. Futaba, D. N.; Hata, K.; Yamada, T.; Mizuno, K.; Yumura, M.; Iijima, S. Kinetics of water-assisted single-walled carbon nanotube synthesis revealed by a time-evolution analysis *Phys. Rev. Lett.* **2005**, *95*, 4.

37. Hata, K.; Futaba, D. N.; Mizuno, K.; Namai, T.; Yumura, M.; Iijima, S. Water-assisted highly efficient synthesis of impurity-free single-waited carbon nanotubes *Science* **2004**, *306*, 1362-1364.

38. Yamada, T.; Namai, T.; Hata, K.; Futaba, D. N.; Mizuno, K.; Fan, J.; Yudasaka, M.; Yumura, M.; Iijima, S. Size-selective growth of double-walled carbon nanotube forests from engineered iron catalysts *Nat. Nanotechnol.* **2006**, *1*, 131-136.

39. Wirth, C. T.; Zhang, C.; Zhong, G.; Hofmann, S.; Robertson, J. Diffusion- and Reaction-Limited Growth of Carbon Nanotube Forests *ACS Nano* **2009**, *3*, 3560-3566.

40. Dresselhaus, M. S.; Dresselhaus, G.; Saito, R.; Jorio, A. Raman spectroscopy of carbon nanotubes *Phys. Rep.* **2005**, *409*, 47-99.

41. Rao, A. M.; Jorio, A.; Pimenta, M. A.; Dantas, M. S. S.; Saito, R.; Dresselhaus, G.; Dresselhaus, M. S. Polarized Raman Study of Aligned Multiwalled Carbon Nanotubes *Phys. Rev. Lett.* **2000**, *84*, 1820.

42. Bachilo, S. M.; Strano, M. S.; Kittrell, C.; Hauge, R. H.; Smalley, R. E.; Weisman, R. B. Structure-assigned optical spectra of single-walled carbon nanotubes *Science* **2002**, *298*, 2361-2366.

43. May, G. S.; Spanos, C. J. *Fundamentals of Semiconductor Manufacturing and Process Control*; Wiley-IEEE Press: Hoboken, New Jersey, 2006.

44. Philofsky, E.; Ravi, K.; Hall, E.; Black, J. "Surface Reconstruction of Aluminum Metallization -- a New Potential Wearout Mechanism"; Reliability Physics Symposium, 1971. 9th Annual, 1971.

45. Faith, T. J. Hillock‐free integrated‐circuit metallizations by Al/Al‐O layering *J. Appl. Phys.* **1981**, *52*, 4630.

46. Smith, U.; Kristensen, N.; Ericson, F.; Schweitz, J. A. LOCAL STRESS-RELAXATION PHENOMENA IN THIN ALUMINUM FILMS *J. Vac. Sci. Technol. A-Vac. Surf. Films* **1991**, *9*, 2527-2535.

47. Kusaka, K.; Hanabusa, T.; Nishida, M.; Inoko, F. Residual stress and in-situ thermal stress measurement of aluminum film deposited on silicon wafer *Thin Solid Films* **1996**, *290*, 248-253.

48. Thompson, C. V.; Carel, R. Stress and grain growth in thin films *Journal of the Mechanics and Physics of Solids* **1996**, *44*, 657-673.

49. Kim, D. K.; Nix, W. D.; Vinci, R. P.; Deal, M. D.; Plummer, J. D. Study of the effect of grain boundary migration on hillock formation in Al thin films *J. Appl. Phys.* **2001**, *90*, 781-788.

50. Hwang, S.-J.; Lee, J.-H.; Jeong, C.-O.; Joo, Y.-C. Effect of film thickness and annealing temperature on hillock distributions in pure Al films *Scr. Mater.* **2007**, *56*, 17-20.

51. Cardenas, J. F.; Glerup, M. The influence of surfactants on the distribution of the radial breathing modes of single walled carbon nanotubes *Nanotechnology* **2006**, *17*, 5212-5215.

52. Strano, M. S.; Moore, V. C.; Miller, M. K.; Allen, M. J.; Haroz, E. H.; Kittrell, C.; Hauge, R. H.; Smalley, R. E. The role of surfactant adsorption during ultrasonication in the dispersion of single-walled carbon nanotubes *J. Nanosci. Nanotechnol.* **2003**, *3*, 81-86.

53. O'Connell, M. J.; Bachilo, S. M.; Huffman, C. B.; Moore, V. C.; Strano, M. S.; Haroz, E. H.; Rialon, K. L.; Boul, P. J.; Noon, W. H.; Kittrell, C.et al. Band gap fluorescence from individual single-walled carbon nanotubes *Science* **2002**, *297*, 593-596.

54. Moore, V. C.; Strano, M. S.; Haroz, E. H.; Hauge, R. H.; Smalley, R. E.; Schmidt, J.; Talmon, Y. Individually suspended single-walled carbon nanotubes in various surfactants *Nano Lett.* **2003**, *3*, 1379-1382.

55. Hilding, J.; Grulke, E. A.; Zhang, Z. G.; Lockwood, F. Dispersion of carbon nanotubes in liquids *J. Dispersion Sci. Technol.* **2003**, *24*, 1-41.

56. Liu, J.; Rinzler, A. G.; Dai, H. J.; Hafner, J. H.; Bradley, R. K.; Boul, P. J.; Lu, A.; Iverson, T.; Shelimov, K.; Huffman, C. B.et al. Fullerene pipes *Science* **1998**, *280*, 1253-1256.

57. Tan, Y. Q.; Resasco, D. E. Dispersion of single-walled carbon nanotubes of narrow diameter distribution *J. Phys. Chem. B* **2005**, *109*, 14454-14460.

58. Wang, F.; Dukovic, G.; Brus, L. E.; Heinz, T. F. Time-resolved fluorescence of carbon nanotubes and its implication for radiative lifetimes *Phys. Rev. Lett.* **2004**, *92*.

59. Yamamoto, T.; Miyauchi, Y.; Motoyanagi, J.; Fukushima, T.; Aida, T.; Kato, M.; Maruyama, S. Improved bath sonication method for dispersion of individual single-walled carbon nanotubes using new triphenylene-based surfactant *Japanese Journal of Applied Physics* **2008**, *47*, 2000-2004.

60. Matarredona, O.; Rhoads, H.; Li, Z. R.; Harwell, J. H.; Balzano, L.; Resasco, D. E. Dispersion of single-walled carbon nanotubes in aqueous solutions of the anionic surfactant NaDDBS *J. Phys. Chem. B* **2003**, *107*, 13357-13367.

61. Bandyopadhyaya, R.; Nativ-Roth, E.; Regev, O.; Yerushalmi-Rozen, R. Stabilization of individual carbon nanotubes in aqueous solutions *Nano Lett.* **2002**, *2*, 25-28.

62. Mitchell, C. A.; Bahr, J. L.; Arepalli, S.; Tour, J. M.; Krishnamoorti, R. Dispersion of functionalized carbon nanotubes in polystyrene *Macromolecules* **2002**, *35*, 8825-8830.

63. Nakashima, N.; Tomonari, Y.; Murakami, H. Water-soluble single-walled carbon nanotubes via noncovalent sidewall-functionalization with a pyrene-carrying ammonium ion *Chem. Lett.* **2002**, 638-639.

64. Star, A.; Stoddart, J. F. Dispersion and solubilization of single-walled carbon nanotubes with a hyperbranched polymer *Macromolecules* **2002**, *35*, 7516-7520.

65. Zheng, M.; Jagota, A.; Semke, E. D.; Diner, B. A.; McLean, R. S.; Lustig, S. R.; Richardson, R. E.; Tassi, N. G. DNA-assisted dispersion and separation of carbon nanotubes *Nat. Mater.* **2003**, *2*, 338-342.

66. Hirsch, A.; Vostrowsky, O. Functionalization of carbon nanotubes *Top. Curr. Chem.* **2005**, *245*, 193-237.

67. Ausman, K. D.; Piner, R.; Lourie, O.; Ruoff, R. S.; Korobov, M. Organic solvent dispersions of single-walled carbon nanotubes: Toward solutions of pristine nanotubes *J. Phys. Chem. B* **2000**, *104*, 8911-8915.

68. Bahr, J. L.; Mickelson, E. T.; Bronikowski, M. J.; Smalley, R. E.; Tour, J. M. Dissolution of small diameter single-wall carbon nanotubes in organic solvents? *Chem. Commun.* **2001**, 193-194.

69. Landi, B. J.; Ruf, H. J.; Worman, J. J.; Raffaelle, R. P. Effects of alkyl amide solvents on the dispersion of single-wall carbon nanotubes *J. Phys. Chem. B* **2004**, *108*, 17089-17095.

70. Bergin, S. D.; Nicolosi, V.; Streich, P. V.; Giordani, S.; Sun, Z. Y.; Windle, A. H.; Ryan, P.; Niraj, N. P. P.; Wang, Z. T. T.; Carpenter, L.et al. Towards solutions of single-walled carbon nanotubes in common solvents *Adv. Mater.* **2008**, *20*, 1876-1881.

71. Bergin, S. D.; Sun, Z. Y.; Rickard, D.; Streich, P. V.; Hamilton, J. P.; Coleman, J. N. Multicomponent Solubility Parameters for Single-Walled Carbon Nanotube-Solvent Mixtures *ACS Nano* **2009**, *3*, 2340-2350.

72. Bergin, S. D.; Sun, Z. Y.; Streich, P.; Hamilton, J.; Coleman, J. N. New Solvents for Nanotubes: Approaching the Dispersibility of Surfactants *J. Phys. Chem. C* **2010**, *114*, 231-237.

73. Sano, M.; Okamura, J.; Shinkai, S. Colloidal Nature of Single-Walled Carbon Nanotubes in Electrolyte Solution: The Schulze-Hardy Rule *Langmuir* **2001**, *17*, 7172-7173.

74. Giordano, A. N.; Chaturvedi, H.; Poler, J. C. Critical coagulation concentrations for carbon nanotubes in nonaqueous solvent *J. Phys. Chem. C* **2007**, *111*, 11583-11589.

75. Verwey, E. J. W.; Overbeek, J. T. G. *Theory of the Stability of Lyophobic Colloids*; Elsvier Pub. Co.: New York, 1948.

76. Deryagin, B.; Landau, L. Theory of the stability of strongly charged lyophobic sols and of the adhesion of strongly charged particles in solutions of electrolytes *Acta. Phys. Chim. URSS* **1941**, *14*, 633-662.

77. Evans, D. F.; Wennerström, H. *The Colloidal Domain: Where Physics, Chemistry, Biology, and Technology Meet*, Second Edition ed.; Wiley-VCH, 1999.

78. Hu, H.; Yu, A. P.; Kim, E.; Zhao, B.; Itkis, M. E.; Bekyarova, E.; Haddon, R. C. Influence of the zeta potential on the dispersability and purification of single-walled carbon nanotubes *J. Phys. Chem. B* **2005**, *109*, 11520-11524.

79. Jiang, L. Q.; Gao, L.; Sun, J. Production of aqueous colloidal dispersions of carbon nanotubes *J. Colloid Interface Sci.* **2003**, *260*, 89-94.

80. Sun, Z.; Nicolosi, V.; Rickard, D.; Bergin, S. D.; Aherne, D.; Coleman, J. N. Quantitative evaluation of surfactant-stabilized single-walled carbon nanotubes: Dispersion quality and its correlation with zeta potential *J. Phys. Chem. C* **2008**, *112*, 10692-10699.

81. Chen, K. L.; Smith, B. A.; Ball, W. P.; Fairbrother, D. H. Assessing the colloidal properties of engineered nanoparticles in water: case studies from fullerene C-60 nanoparticles and carbon nanotubes *Environ. Chem.* **2010**, *7*, 10-27.

82. Forney, M. W.; Poler, J. C. Significantly Enhanced Single-Walled Carbon Nanotube Dispersion Stability in Mixed Solvent Systems *The Journal of Physical Chemistry C* **2011**, *115*, 10531-10536.

83. Li, M. H.; Huang, C. P. Stability of oxidized single-walled carbon nanotubes in the presence of simple electrolytes and humic acid *Carbon* **2010**, *48*, 4527-4534.

84. Saleh, N. B.; Pfefferle, L. D.; Elimelech, M. Aggregation Kinetics of Multiwalled Carbon Nanotubes in Aquatic Systems: Measurements and Environmental Implications *Environ. Sci. Technol.* **2008**, *42*, 7963-7969.

85. Saleh, N. B.; Pfefferle, L. D.; Elimelech, M. Influence of Biomacromolecules and Humic Acid on the Aggregation Kinetics of Single-Walled Carbon Nanotubes *Environ. Sci. Technol.* **2010**, *44*, 2412-2418.

86. Smith, B.; Wepasnick, K.; Schrote, K. E.; Bertele, A. H.; Ball, W. P.; O'Melia, C.; Fairbrother, D. H. Colloidal Properties of Aqueous Suspensions of Acid-Treated, Multi-Walled Carbon Nanotubes *Environ. Sci. Technol.* **2009**, *43*, 819-825.

87. Smith, B.; Wepasnick, K.; Schrote, K. E.; Cho, H. H.; Ball, W. P.; Fairbrother, D. H. Influence of Surface Oxides on the Colloidal Stability of Multi-Walled Carbon Nanotubes: A Structure-Property Relationship *Langmuir* **2009**, *25*, 9767-9776.

88. Furtado, C. A.; Kim, U. J.; Gutierrez, H. R.; Pan, L.; Dickey, E. C.; Eklund, P. C. Debundling and dissolution of single-walled carbon nanotubes in amide solvents *J. Am. Chem. Soc.* **2004**, *126*, 6095-6105.

89. Giordani, S.; Bergin, S. D.; Nicolosi, V.; Lebedkin, S.; Kappes, M. M.; Blau, W. J.; Coleman, J. N. Debundling of single-walled nanotubes by dilution: Observation of large populations of individual nanotubes in amide solvent dispersions *J. Phys. Chem. B* **2006**, *110*, 15708-15718.

90. Misik, V.; Kirschenbaum, L. J.; Riesz, P. Free-radical Production by Sonolysis of Aqueous Mixtures of N,N-Dimethylformamide - An EPR Spin-trapping Study *J. Phys. Chem.* **1995**, *99*, 5970-5976.

91. Misik, V.; Riesz, P. EPR study of free radicals induced by ultrasound in organic liquids .2. Probing the temperatures of cavitation regions *Ultrason. Sonochem.* **1996**, *3*, 25-37.

92. Wang, J.; Huang, L. Y.; Chen, G. A.; Huang, J. L. The sonochemiluminescence of Lucigenin in N,N-dimethylformamide solution under the influence of natural flavonoids *Chem. Lett.* **2005**, *34*, 1514-1515.

93. Miko, C.; Milas, M.; Seo, J. W.; Gaal, R.; Kulik, A.; Forro, L. Effect of ultraviolet light irradiation on macroscopic single-walled carbon nanotube bundles *Appl. Phys. Lett.* **2006**, *88*.

94. Misik, V.; Riesz, P. Peroxyl radical formation in aqueous solutions of N,N-dimethylformamide, N-methylformamide, and dimethylsulfoxide by ultrasound: Implications for sonosensitized cell killing *Free Radical Biol. Med.* **1996**, *20*, 129-138.

95. Cardenas, J. F. Protonation and sonication effects on aggregation sensitive Raman features of single wall carbon nanotubes *Carbon* **2008**, *46*, 1327-1330.

96. Sabnis, R. W. *Handbook of acid-base indicators*; CRC Press, Taylor & Francis Group: Boca Raton, 2007.

97. Perkins, M. J. *Radical Chemistry: The Fundamentals*; Oxford University Press: New York, 2000.

98. Pryor, W. A. *Free Radicals*; McGraw-Hill Book Company: New York, 1966.

99. Nakamura, E.; Sato, K.; Imanishi, Y. Sonochemical Synthesis of Alkyl Hydroperoxides by Aerobic Reductive Oxygenation of Alkyl-halides *Synlett* **1995**, 525-526.

100. Fischer, K.; Wilken, M. Experimental determination of oxygen and nitrogen solubility in organic solvents up to 10 MPa at temperatures between 298 K and 398 K *J. Chem. Thermodyn.* **2001**, *33*, 1285-1308.

101. Packer, L.; Glazer, A. N.; Ames, B. *Oxygen radicals in biological systems*, 1 ed.; Elsevier, 1994.

102. Che, Y.; Tsushima, M.; Matsumoto, F.; Okajima, T.; Tokuda, K.; Ohsaka, T. Water-induced disproportionation of superoxide ion in aprotic solvents *J. Phys. Chem.* **1996**, *100*, 20134-20137.

103. Chaturvedi, H.; Giordano, A. N.; Kim, M.-J.; MacDonnell, F. M.; Subaran, S. S.; Poler, J. C. "Mechanically Docked" Metallodendrimers about Single-Walled Carbon Nanotubes *J. Phys. Chem. C* **2009**, *113*, 11254-11261.

104. Chaturvedi, H.; Poler, J. C. Binding of rigid dendritic ruthenium complexes to carbon nanotubes *J. Phys. Chem. B* **2006**, *110*, 22387-22393.

105. Caminade, A.-M.; Majoral, J.-P. Dendrimers and nanotubes: a fruitful association *Chem. Soc. Rev.*, *39*, 2034-2047.

106. Derjaguin, B.; Landau, L. Theory of the stability of strongly charged lyophobic sols and of the adhesion of strongly charged particles in solutions of electrolytes *Acta. Phys. Chim. URSS* **1941**, *14*, 633-662.

107. Hansen, C. M. *Hansen Solubility Parameters - A User's Handbook*; CRC Press: Boca Raton, FL, 2007.

108. Detriche, S.; Zorzini, G.; Colomer, J.; Fonseca, A.; Nagy, J. Application of the Hansen Solubility Parameters Theory to Carbon Nanotubes *J. Nanosci. Nanotechnol.* **2008**, *8*, 6082-6092.

109. Usrey, M. L.; Chaffee, A.; Jeng, E. S.; Strano, M. S. Application of Polymer Solubility Theory to Solution Phase Dispersion of Single-Walled Carbon Nanotubes *J. Phys. Chem. C* **2009**, *113*, 9532-9540.

110. MacKernan, D.; Blau, W. J. Exploring the mechanisms of carbon-nanotube dispersion aggregation in a highly polar solvent *EPL (Europhysics Letters)* **2008**, *83*, 66009.

111. Shih, C.-J.; Lin, S.; Strano, M. S.; Blankschtein, D. Understanding the Stabilization of Liquid-Phase-Exfoliated Graphene in Polar Solvents: Molecular Dynamics Simulations and Kinetic Theory of Colloid Aggregation *J. Am. Chem. Soc.* **2010**, *132*, 14638-14648.

112. Grolimund, D.; Elimelech, M.; Borkovec, M. Aggregation and deposition kinetics of mobile colloidal particles in natural porous media *Colloids and Surfaces A: Physicochemical and Engineering Aspects* **2001**, *191*, 179-188.

113. Hsu, J.-P.; Kuo, Y.-C. The Critical Coagulation Concentration of Counterions: Spherical Particles in Asymmetric Electrolyte Solutions *J. Colloid Interface Sci.* **1997**, *185*, 530-537.

114. Jungen, A.; Stampfer, C.; Hoetzel, J.; Bright, V. M.; Hierold, C. Process integration of carbon nanotubes into microelectromechanical systems *Sensors and Actuators A: Physical* **2006**, *130-131*, 588-594.

115. Li, J.; Lu, Y. J.; Ye, Q.; Cinke, M.; Han, J.; Meyyappan, M. Carbon nanotube sensors for gas and organic vapor detection *Nano Lett.* **2003**, *3*, 929-933.

116. Bonard, J. M.; Salvetat, J. P.; Stockli, T.; Forro, L.; Chatelain, A. Field emission from carbon nanotubes: perspectives for applications and clues to the emission mechanism *Applied Physics a-Materials Science & Processing* **1999**, *69*, 245-254.

117. Kongkanand, A.; Dominguez, R. M.; Kamat, P. V. Single wall carbon nanotube scaffolds for photoelectrochemical solar cells. Capture and transport of photogenerated electrons *Nano Lett.* **2007**, *7*, 676-680.

118. Coleman, J. N.; Khan, U.; Gun'ko, Y. K. Mechanical reinforcement of polymers using carbon nanotubes *Adv. Mater.* **2006**, *18*, 689-706.

119. Martin, C. A.; Sandler, J. K. W.; Windle, A. H.; Schwarz, M. K.; Bauhofer, W.; Schulte, K.; Shaffer, M. S. P. Electric field-induced aligned multi-wall carbon nanotube networks in epoxy composites *Polymer* **2005**, *46*, 877-886.

120. Qian, D.; Dickey, E. C.; Andrews, R.; Rantell, T. Load transfer and deformation mechanisms in carbon nanotube-polystyrene composites *Appl. Phys. Lett.* **2000**, *76*, 2868-2870.

121. Schadler, L. S.; Giannaris, S. C.; Ajayan, P. M. Load transfer in carbon nanotube epoxy composites *Appl. Phys. Lett.* **1998**, *73*, 3842-3844.

122. Deshmukh, S.; Ounaies, Z. Single Walled Carbon Nanotube (SWNT)-Polyimide Nanocomposites as Electrostrictive Materials *Sensors and Actuators A: Physical*, *In Press, Accepted Manuscript*.

123. Kongkanand, A.; Kamat, P. V. Interactions of single wall carbon nanotubes with methyl viologen radicals. Quantitative estimation of stored electrons *J. Phys. Chem. C* **2007**, *111*, 9012-9015.

124. Fritz, J.; Baller, M. K.; Lang, H. P.; Rothuizen, H.; Vettiger, P.; Meyer, E.; Guntherodt, H. J.; Gerber, C.; Gimzewski, J. K. Translating biomolecular recognition into nanomechanics *Science* **2000**, *288*, 316-318.

125. Ilic, B.; Yang, Y.; Craighead, H. G. Virus detection using nanoelectromechanical devices *Appl. Phys. Lett.* **2004**, *85*, 2604-2606.

126. Norman, L. L.; Badia, A. Redox Actuation of a Microcantilever Driven by a Self-Assembled Ferrocenylundecanethiolate Monolayer: An Investigation of the Origin of the Micromechanical Motion and Surface Stress *J. Am. Chem. Soc.* **2009**, *131*, 2328-2337.

127. Tabard-Cossa, V.; Godin, M.; Grutter, P.; Burgess, I.; Lennox, R. B. Redox-Induced Surface Stress of Polypyrrole-Based Actuators *The Journal of Physical Chemistry B* **2005**, *109*, 17531-17537.

128. Bumbu, G. G.; Wolkenhauer, M.; Kircher, G.; Gutmann, J. S.; Berger, R. Micromechanical cantilever technique: A tool for investigating the swelling of polymer brushes *Langmuir* **2007**, *23*, 2203-2207.

129. Berger, R.; Delamarche, E.; Lang, H. P.; Gerber, C.; Gimzewski, J. K.; Meyer, E.; Guntherodt, H.-J. Surface Stress in the Self-Assembly of Alkanethiols on Gold *Science* **1997**, *276*, 2021-2024.

130. Aliev, A. E.; Oh, J. Y.; Kozlov, M. E.; Kuznetsov, A. A.; Fang, S. L.; Fonseca, A. F.; Ovalle, R.; Lima, M. D.; Haque, M. H.; Gartstein, Y. N.et al. Giant-Stroke, Superelastic Carbon Nanotube Aerogel Muscles *Science* **2009**, *323*, 1575-1578.

131. Stoney, G. G. The Tension of Metallic Films Deposited by Electrolysis *Proceedings of the Royal Society of London. Series A, Containing Papers of a Mathematical and Physical Character* **1909**, *82*, 172-175.

132. Tabard-Cossa, V.; Godin, M.; Beaulieu, L. Y.; Grutter, P. Erratum to: "A differential microcantilever-based system for measuring surface stress changes induced by electrochemical reactions" [Sensors and Actuators B 107 (2005) 233-241] *Sensors and Actuators B: Chemical* **2006**, *119*, 352-354.

133. Tabard-Cossa, V.; Godin, M.; Beaulieu, L. Y.; Grutter, P. A differential microcantilever-based system for measuring surface stress changes induced by electrochemical reactions *Sensors and Actuators B: Chemical* **2005**, *107*, 233-241.

134. Brantley, W. A. Calculated elastic constants for stress problems associated with semiconductor devices *J. Appl. Phys.* **1973**, *44*, 534-535.

135. Wang, Y. Y.; Gupta, S.; Nemanich, R. J.; Liu, Z. J.; Qin, L. C. Hollow to bamboolike internal structure transition observed in carbon nanotube films *J. Appl. Phys.* **2005**, *98*, 014312-014316.

136. Schelling, P. K.; Keblinski, P. Thermal expansion of carbon structures *Phys. Rev. B* **2003**, *68*, 035425.

137. DiLeo, R. A.; Castiglia, A.; Ganter, M. J.; Rogers, R. E.; Cress, C. D.; Raffaelle, R. P.; Landi, B. J. Enhanced Capacity and Rate Capability of Carbon Nanotube

Based Anodes with Titanium Contacts for Lithium Ion Batteries *ACS Nano* **2010**, *4*, 6121-6131.

138. Felten, A.; Suarez-Martinez, I.; Ke, X.; Van Tendeloo, G.; Ghijsen, J.; Pireaux, J.-J.; Drube, W.; Bittencourt, C.; Ewels, C. P. The Role of Oxygen at the Interface between Titanium and Carbon Nanotubes *ChemPhysChem* **2009**, *10*, 1799-1804.

139. Chaturvedi, H.; Poler, J. C. Photon enhanced aggregation of single walled carbon nanotube dispersions *Appl. Phys. Lett.* **2007**, *90*.

140. Afanas'ev, I. B. *Superoxide Ion: Chemistry and Biological Implications*; CRC Press, 1989; Vol. I.

141. Afanas'ev, I. B. P., S. V.; Mal'tseva, T. Ya.; Samokhvalov, G. I. Electron transfer reactions between the superoxide ion and quinones *Int. J. Chem. Kinet.* **1974** *6*, 643-661.

142. Afanas'ev, I. B. P., S. V.; Samokhvalov, G. I. Relative rate constants for reactions of superoxide ion with benzoquinone and trimethylbenzoquinone *Kinet. Katal.* **1974**, *15*, 922-928.

143. Ozawa, T.; Hanaki, A.; Yamamoto, H. SPECTRALLY WELL-DEFINED AND STABLE SOURCE OF SUPEROXIDE ION O-(2) *FEBS Lett.* **1977**, *74*, 99-102.

144. MacInnes, D. A. *The Principles of Electrochemistry*; Reinhold Publishing Company, Dover Publications Inc.: New York, 1961.

145. Heller, D. A.; Jeng, E. S.; Yeung, T. K.; Martinez, B. M.; Moll, A. E.; Gastala, J. B.; Strano, M. S. Optical detection of DNA conformational polymorphism on single-walled carbon nanotubes *Science* **2006**, *311*, 508-511.

APPENDIX A: ADDITIONAL EXPERIMENTS RELATED TO METHYL HYDROPEROXIDE STUDY

Before determining that methyl hydroperoxide was forming during ultrasonication, several alternative hypotheses were considered. In our JACS paper, we discussed the role of water, radical generation and possible SNWT cross-linking, and solvent modification as possible alternatives that had been ruled out. Another hypothesis, which did not get a detailed discussion in the paper, was that we were forming superoxide (O_2^-). This hypothesis was generated because we were looking for a stable ion (or at least semi-stable) that was related to oxygen. This hypothesis was tested by a series of experiments and eventually ruled out.

Optical absorption was the first technique used to try to detect the presence of superoxide, as it should have an optical absorption maximum at 257.5 nm with $\varepsilon = 2500 \pm 150\ M^{-1}cm^{-1}$.[140] Spectra from "IB" ultrasonicated DMF, DMA, and NMP showed what appeared to be absorption peaks in the 250-270 nm range (see Figure A.1). Unfortunately, each of these solvents have UV cutoffs of 270-290 nm, therefore the apparent peaks are artifacts resulting from the solvent cutoff.

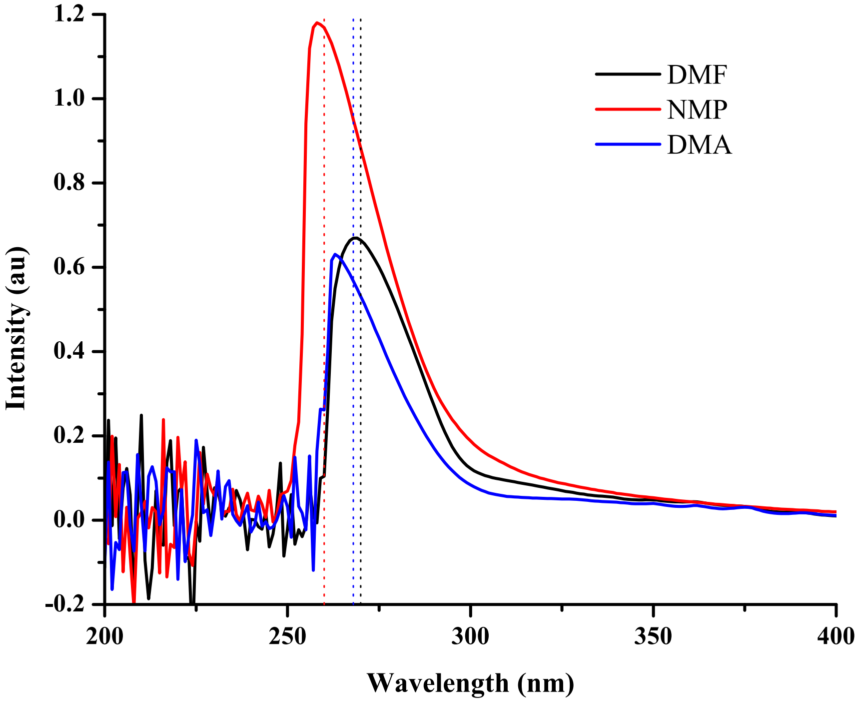

Figure A.1: Absorption spectra of superoxide in DMF, NMP, and DMA. The real peak is obscured, as the UV cutoffs of these solvents are too high (indicated with vertical dotted lines).

The next approach used to detect superoxide was the reduction of benzoquinone (BQ) to benzosemiquinone (BSQ). This reaction should occur in the presence of superoxide, and it provides a colorimetric test for superoxide because BSQ has a distinctive absorption spectrum in the 400-500 nm range.[141,142] Initial tests on "IB" ultrasonicated DMF were unsuccessful at producing BSQ, indicating that superoxide was not present.

Next, I assembled an electrochemical cell to try to generate superoxide electrochemically and verify that the reduction of BQ to BSQ test would work as expected (see Figure A.2). The cell was contained in a 50 mL glass beaker. It held two Pt wire basket electrodes, one nested inside the other. O_2 was delivered between the electrodes by a pipette tip. A BK Precision 1651A Triple Output DC Power Supply provided the 1 V potential needed to convert O_2 to O_2^-.[141-143] The electrolyte was tetrabutylammonium hexafluorophosphate ($TBAPF_6$), at a concentration of 0.025 M in DMF.

The electrochemical reduction of O_2 to O_2^- in O_2 saturated DMF and acetonitrile were performed at 1 V for 2 hr. After the electrochemical reduction step, BQ was added to the samples, and the formation of BSQ was checked by UV-Vis spectroscopy. Despite several trials and refinement of the experimental apparatus, superoxide was not successfully produced or identified by the BSQ test.

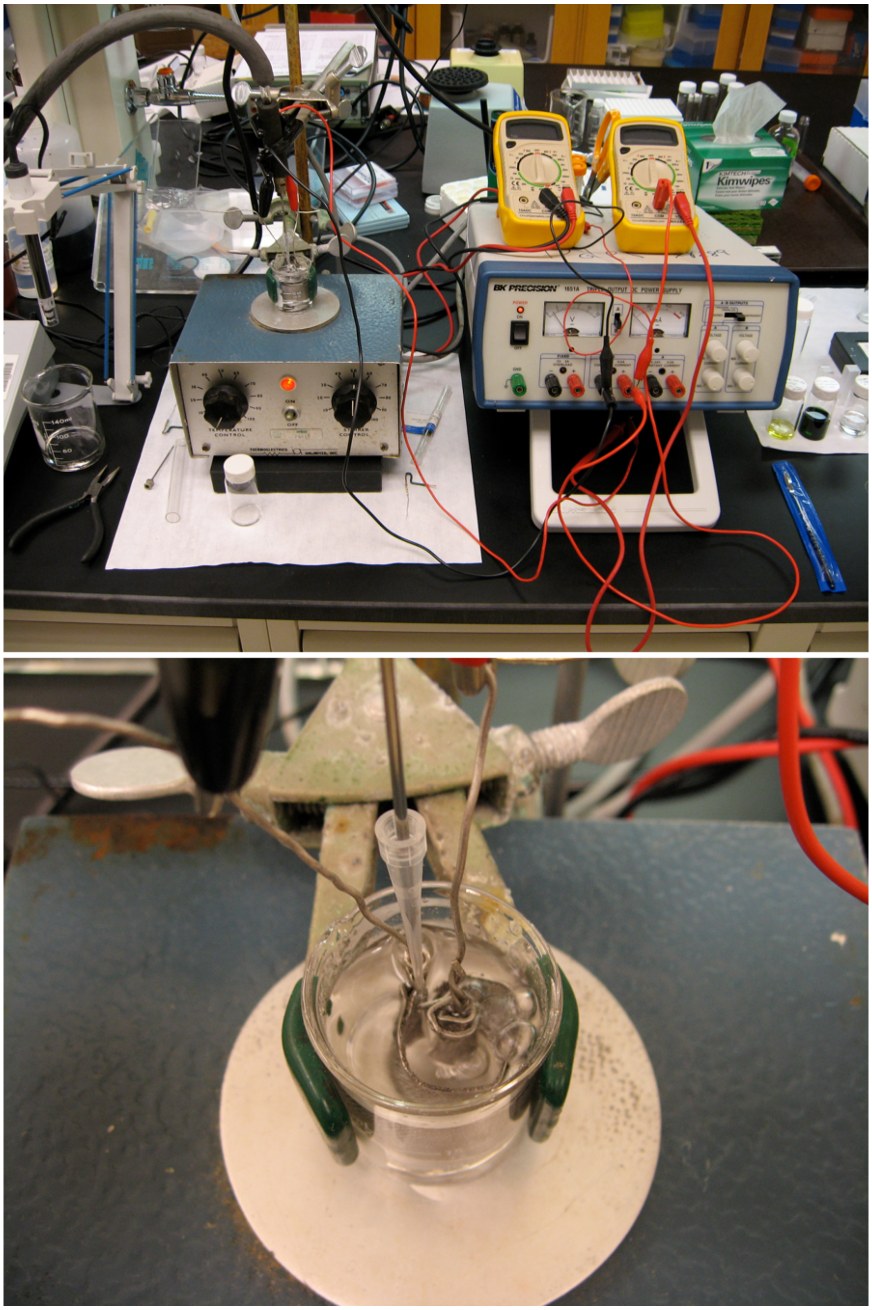

Figure A.2: Electrochemical cell built for generating superoxide. The left image shows the full apparatus, with cell, stir plate, power supply, and multimeters visible. The right image is a close-up of the cell, showing the Pt wire basket electrodes and a pipette tip for O_2 delivery.

Further research revealed that BQ should be bright yellow, but the BQ we had been working with was a dingy gray. Apparently, BQ quickly oxidizes and degrades, so BQ requires purification by cold finger sublimation before use. The unpurified BQ was loaded into a coldfinger apparatus for purification. Cold water was run through the coldfinger while the apparatus was gently heated from the bottom by a hot plate, under moderate vacuum. Within 30 min, the purified BQ (60% of original mass) had crystallized on the cold finger and was a bright yellow (see Figure A.3).

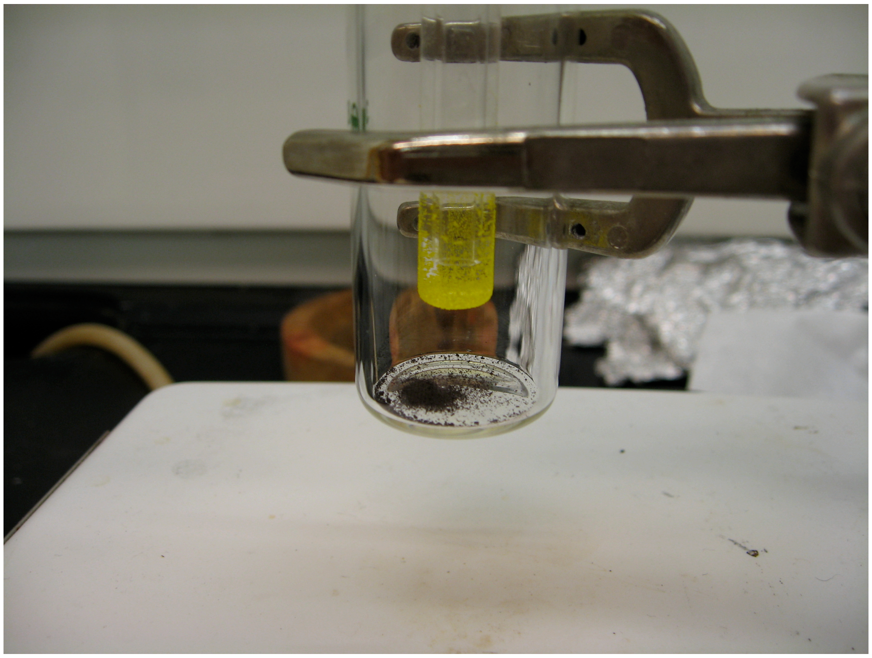

Figure A.3: BQ purification. Pure BQ has crystallized on the coldfinger and is bright yellow. The residual un-purified material is gray/black and remains on the bottom.

UV-Vis spectra confirmed that the purified material was BQ. A solution of pure BQ was used to test a sample of "IB-O_2" ultrasonicated DMF, but no conversion of BQ to BSQ was observed by UV-Vis spectroscopy. Due to the repeated lack of success in detecting superoxide that has been produced ultrasonically or electrochemically, we decided to test the reduction of BQ to BSQ by superoxide directly, by adding a KO_2 salt to DMF or acetonitrile (see Figure A.4). Finally, using this method, we were able to observe a change from BQ to BSQ, and the spectrum matched the literature.[142] It was difficult to get the correct spectrum, initially, because the superoxide decays quickly. If there is some water in the solvent, and these are hygroscopic solvents, superoxide will be disproportionated by water and become H_2O_2.[102]

It was necessary to take the UV-Vis spectrum immediately after adding KO_2 to the solution containing BQ, so that the superoxide did not disappear before it could react with BQ to form BSQ. This result indicated that superoxide was not the likely source of dispersion instability, as the acidic/conductive species remained present for an indefinite amount of time. To confirm this conclusion, the ultrasonicator was set up over the UV-Vis-NIR spectrometer and a sample was ultrasonicated with BQ present in the solvent. The temperature controller block was used to ensure that a constant 20 ºC was maintained (mimicking the ice bath). No superoxide was detected and the superoxide hypothesis was rejected.

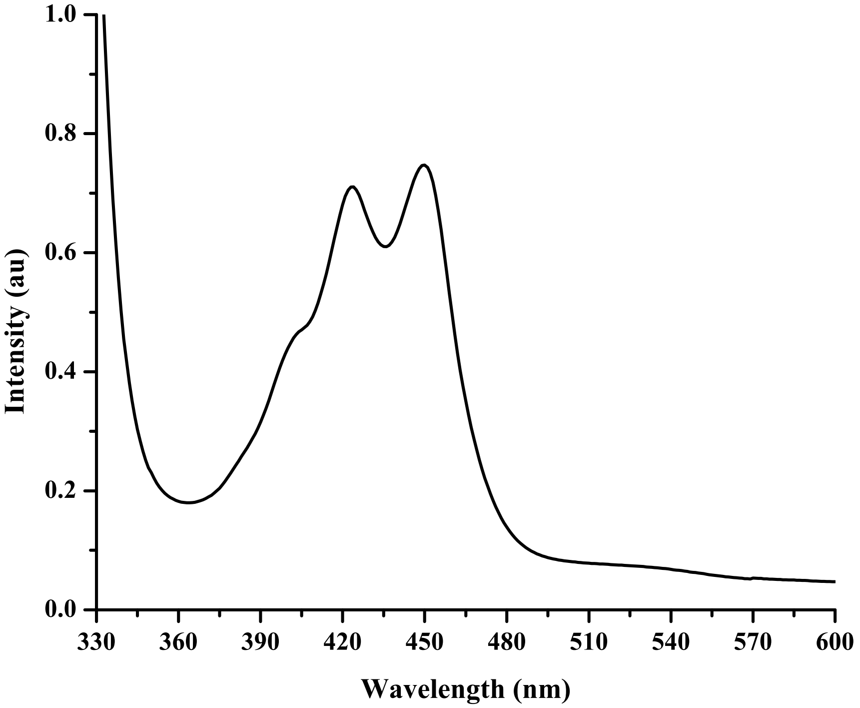

Figure A.4: Absorption spectrum of BSQ that was formed by adding KO_2 to a solution of BQ.

APPENDIX B: CONDUCTIVITY EXPERIMENTS

B.1 Introduction

Electrolyte solutions are formed when salts dissolve and dissociate in aqueous or non-aqueous media, resulting in positive and negative ions that are capable of conducting current. The properties of simple electrolyte solutions have been well studied and characterized by physical chemists decades ago.[144] The conductivity of an electrolytic solution is highly dependent on the concentration, the degree of dissociation of the salt (strong or weak electrolyte), and the dielectric constant of the solvent.

Conductivity is typically normalized by concentration to get molar conductivity, which allows the direct comparison of electrolyte conductivities. It is well known that the molar conductivity increased as the concentration of electrolyte is reduced and approaches a limiting molar conductivity (LMC), which is the best way to compare electrolytes. Extremely dilute electrolytes have increased molar conductivities due to lower interaction between ions and a higher level of dissociation

My first series of experiments were designed to develop a technique for measuring the LMC for simple monovalent salts, such as NaCl or KCl. The goal was to refine a technique that could be used to measure the LMC of $Si(bpy)_3^{4+}$, which was synthesized by Dr. Tom Schmedake. After many trials and improvements the experimental apparatus, a method was developed for aqueous solutions of NaCl and KCl that successfully measured the LMCs.

B.2 Experimental

Materials:

- 170x90 recrystalization dish
- Temperature controlled hot plate with magnetic stirrer (Kika ETS-D4 fuzzy & RTC basic)
- Accumet AR20 pH/Conductivity Meter
- 0.1 cm^{-1} and 1 cm^{-1} Accumet Conductivity Cells
- Utility clamp
- 40 mL sample vial
- 25 mL volumetric flask
- Thermocouple temperature probe
- 2 magnetic stir bars
- Micropipette(s) and tips
- Solid KCl and NaCl
- Ultrapure millipore DI water

Setup:

Prepare a water bath in the recrystalization dish, filling it about 90% full. Place the water bath on the hot plate/stirrer. Place one magnetic stir bar and the temperature probe from the ETS-D4 fuzzy unit into the water bath. Position a utility clamp over the center of the hot plate/stirrer and attach it to the Kika RTC basic's built in ring stand (this will hold the 40 mL sample vial later).

Procedure:

1. Begin by preparing stock solutions of both KCl and NaCl (recommended: concentration ~ 0.5 M, volume ~ 100 mL)

2. Bring the water bath up to temperature by setting the ETS-D4 fuzzy controller to 25 ºC, setting the temperature knob on the RTC basic to ~50 ºC, and setting the Mot knob on the RTC basic to 5.5-6.0. NOTE: If the actual bath temperature reads 25.5 ºC, the sample temperature will likely end up closer to 25.0 ºC.
3. Clean everything that will contact the sample with methanol (dry with N_2 if needed)
4. Once the bath temperature stabilizes, use the utility clamp to hold the 40 mL vial as far under the surface of the bath as possible.
5. If the conductivity probe has been recently, skip to step 11, otherwise continue to step 5.
6. Put a standard KCl solution into the 40 mL sample vial.
7. Insert the second magnetic stir bar into the 40 mL sample vial.
8. Insert the thermocouple probe and appropriate conductivity probe into the 40 mL sample vial.
9. Wait until the thermocouple indicates a sample temperature of exactly 25.0 ºC.
10. Standardize the probe using the AR20.
11. Discard the standardized solution and clean the glassware/probes/stirrer.
12. Use a 25 mL volumetric flask to measure out the initial sample volume of pure DI water, then pour it into the 40 mL sample vial.
13. Insert the second magnetic stir bar into the 40 mL sample vial.
14. Insert the thermocouple probe and appropriate conductivity probe into the 40 mL sample vial.
15. Wait until the thermocouple indicates a stable sample temperature of 25.0±0.1 ºC.

16. Remove conductivity probe (being careful not to lose any of the sample).
17. Add an aliquot (ex., 50 μL or 250 μL) of the KCl or NaCl stock solution to your 25 mL sample.
18. Replace the conductivity probe, making sure that there are no bubbles on the electrodes.
19. Record the conductivity as measured by the AR20 and the sample temperature indicated by the thermocouple.
20. Repeat steps 16-20 for as many data points as desired.

B.3 Discussion and Results

There are several key factors to getting good conductivity measurements. It is important to have good temperature regulation, otherwise the conductivity will fluctuate several percent per degree celsius. Use of a hot plate or temperature regulating bath is sufficient and mixing with a stir bar really helps maintain a uniform bath temperature. An extremely important factor is efficient mixing after adding an aliquot of salt solution. The most effective method found was to use a stir bar in the sample vial. Additionally, careful attention to pippetting was needed to make sure that no extraneous salt solution sticks on the outside of the pippet tip. Once results come within a few percent of the literature values, most of the errors will be random experimental errors, so it becomes necessary to average over multiple trials to improve the data quality.

B.3.1 KCl Limiting Molar Conductivity

The LMC for KCl was measured using conductivity probes with cell constants of 0.1 cm^{-1} and 1.0 cm^{-1}. The 1.0 cm^{-1} probe was tested first. The results from averaging four trials gave a limiting molar conductivity (LMC) of 149.73±0.72 cm^2S/mol (see

Figure B.1), which matches with the literature value of 149.86 cm^{2}S/mol, within errors.[144] The slope of the line, -64.20±9.81 cm^{2}S/mol·M$^{1/2}$, doesn't quite match the literature value of about -84.702 cm^{2}S/mol·M$^{1/2}$.[144] This may have been due to the use of an older micropippette that seemed less accurate for the first three trials, the temperature being a little bit high for those first three trials, or probe inaccuracy.

Next, I measured the LMC of KCl with the 0.1 cm^{-1} probe. The results from averaging four trials gave a LMC of 151.84±0.53 cm^{2}S/mol (see Figure B.2), which is a little higher than the literature value of 149.86 cm^{2}S/mol.[144] Nevertheless, the LMC is only 1.32% off. The main problem with this experiment is that the slope of the line is a factor of ~3 different from what it should be. This problem is still unresolved and unexplained, yet reproducible. I contacted Fisher Scientific, the producer of the Accumet probes, and they were also unable to solve the problem or suggest any viable solutions.

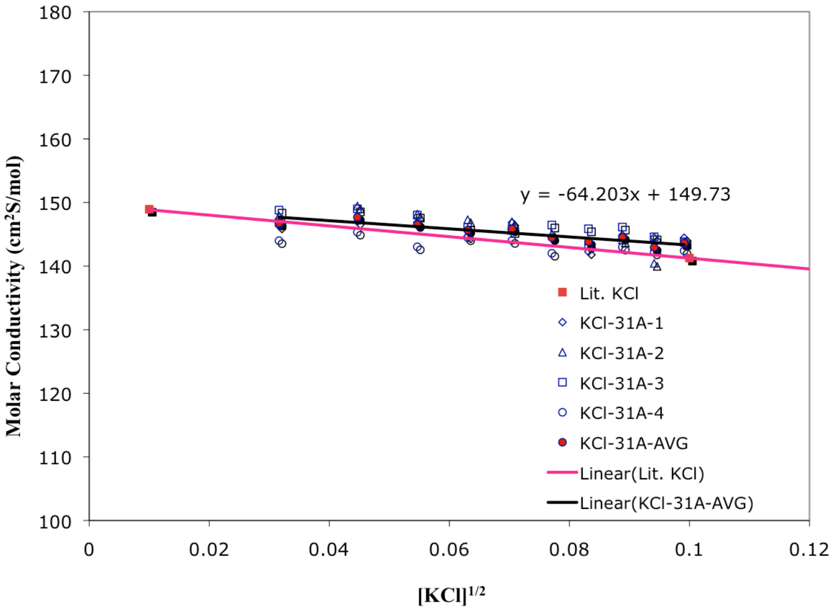

Figure B.1: Conductivity data for KCl gathered with the 1.0 cm^{-1} probe. Four trials were averaged to get higher accuracy.

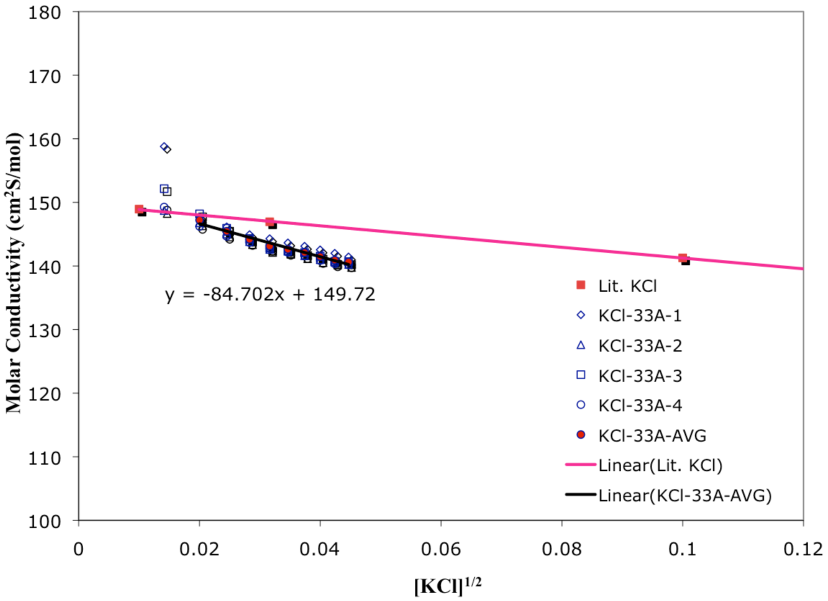

Figure B.2: Conductivity data for KCl gathered with the 0.1 cm^{-1} probe. Four trials were averaged to get higher accuracy. The slope of the data is incorrect, but the LMC is approximately correct.

B.3.2 NaCl Limiting Molar Conductivity

As with KCl, the LMC for NaCl was measured using conductivity probes with cell constants of 0.1 cm^{-1} and 1.0 cm^{-1}. The 1.0 cm^{-1} probe was tested first. The results from averaging four trials gave a limiting molar conductivity (LMC) of 126.71±0.42 cm^2S/mol (see Figure B.3), which matches with the literature value of 126.45 cm^2S/mol.[144] The slope of the line is also good at -80.12±5.68 $cm^2S/mol\cdot M^{1/2}$, compared to the literature value of -78.141 $cm^2S/mol\cdot M^{1/2}$.

Next I measured the LMC of NaCl with the 0.1 cm^{-1} probe. The results from averaging four trials gave a LMC of 128.30±0.41 cm^2S/mol (see Figure B.4), which is a little higher than the literature value of 126.45 cm^2S/mol. Nevertheless, the LMC is only 1.46% off. As with the KCl measurements, the main problem with this experiment is that the slope of the line is a factor of ~3 different from what it should be.

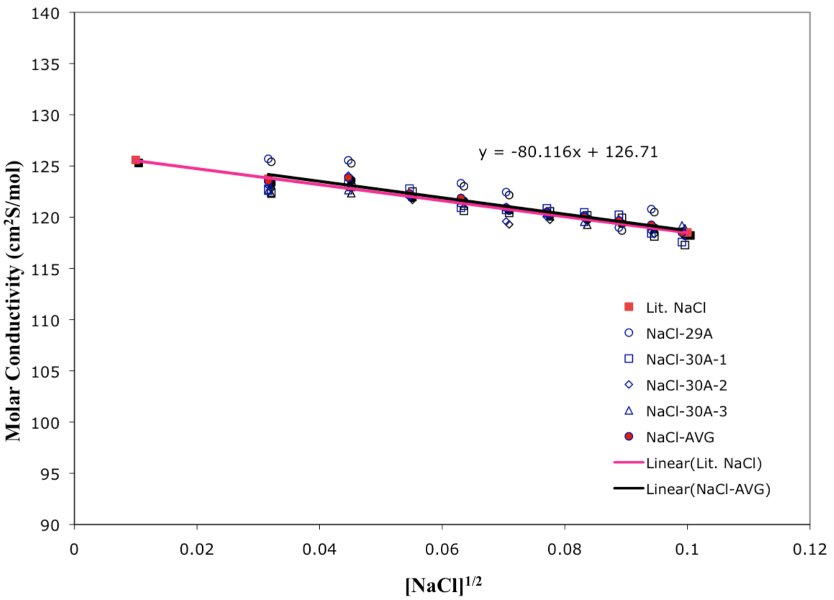

Figure B.3: Conductivity data for NaCl gathered with the 1.0 cm^{-1} probe. Four trials were averaged to get higher accuracy.

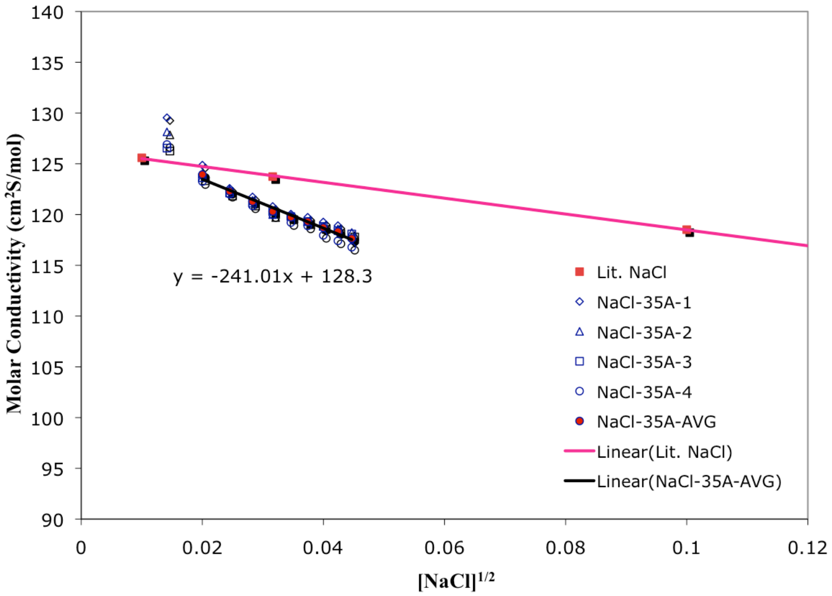

Figure B.4: Conductivity data for NaCl gathered with the 0.1 cm^{-1} probe. Four trials were averaged to get higher accuracy. The slope of the data is incorrect, but the LMC is approximately correct.

APPENDIX C: SWCNT FLUORESCENCE

C.1 Introduction

Band-gap fluorescence is a method by which SWCNT dispersions may be characterized. Fluorescence is especially useful when analyzing a SWCNT dispersion, because it can reveal the chirality of SWCNTs present in the dispersion as well as the relative abundance of each chirality. SWCNTs have characteristic excitation and emission energies depending on the chirality of the SWCNT.

SWCNT excitation/emission peaks in the near infrared are used to uniquely identify SWCNT chirality. Consequently, three-dimensional fluorescence scans are commonly used to observe the emission over a range of excitation wavelengths. From these scans, a contour plot is generated, which allows one to match excitation with emission energies when a SWCNT fluoresces.

In order to correctly interpret the fluorescence spectra from SWCNT dispersions, it was necessary to use both fluorescence and Raman spectroscopy to assign specific chirality SWCNTs to the appropriate peaks. Over 30 assignments were made by Weisman, *et al.*[42] and can be used to rapidly identify some of the SWCNTs that are typically found in SWCNT dispersions. A shortcoming of fluorescence is that some SWCNT chirality do not fluoresce strongly enough to be detected and metallic SWCNTs, of course, do not fluoresce at all.

C.2 Experimental

Sample preparation for measuring SWCNT fluorescence is more challenging than for UV-Vis-NIR absorption or Raman spectroscopy. Bundled SWCNTs disturb each other's electronic properties and quench the already weak fluorescence signal. The predominant method for preparing SWCNT samples for fluorescence measurements was developed by Smalley's group.[53] HiPco grown SWCNTs are first dispersed into D_2O/SDS by sonication. The surfactant-based method was chosen to minimize the re-aggregation of SWCNTs once the dispersion has been made. Next, ultracentrifugation is employed to remove as many of the small (or large) bundles that remain partially dispersed. Ultracentrifugation fields on the order of 100,000 g for several hours ensure that only the well-dispersed, individual SWCNTs remain in the supernatant, which is then used for fluorescence spectroscopy.

C.3 Discussion and Results

While preparing samples to measure SWCNT fluorescence, we first assumed that H_2O/SDS dispersions should work just as well as D_2O/SDS, but we were unsuccessful. Since we also had interest in detecting SWCNT fluorescence when SWCNTs were dispersed in organic solvents such as DMF, DMA, or NMP, I investigated why the H_2O/SDS dispersions were unsuccessful. The fluorescence emission of HiPCO SWCNTs is generally studied in the NIR range of 900 nm – 1400 nm, so I compared the absorption of each of those solvents to the absorption of D_2O in that range (see Figure C.1). This comparison elucidates why SWCNT fluorescence is extremely difficult to detect in H_2O, DMA, DMF, or NMP. The strongest emission peaks in HiPCO SWCNTs are in the 1100 nm – 1300 nm range, where those solvents can absorb 5-50 times as much emission as D_2O does. We also measured the absorption spectrum of deuterated DMF, and it may have weak enough absorption in the NIR for successful measurement of SWCNT fluorescence, though it still absorbs several times more NIR light than D_2O.

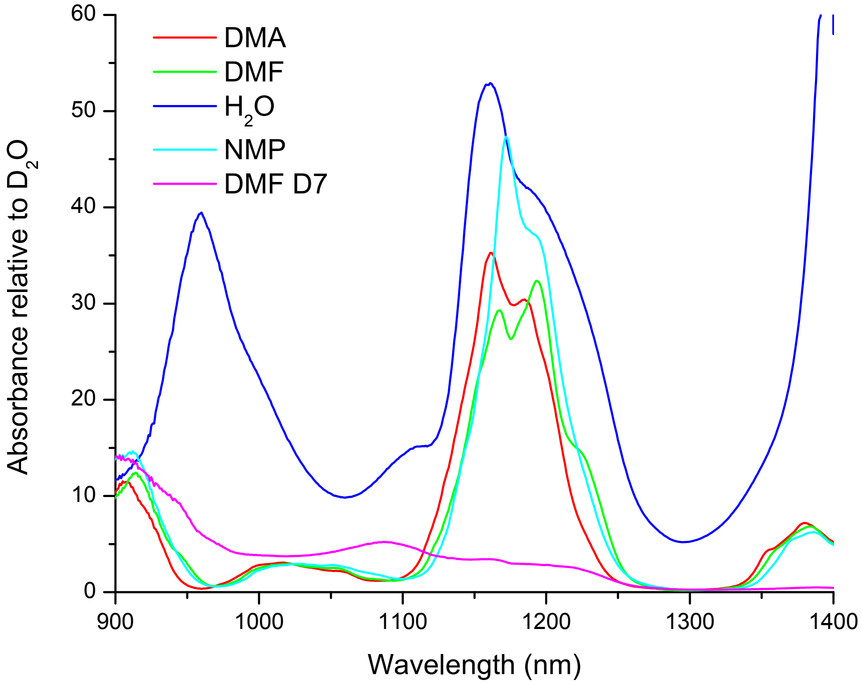

Figure C.1: Relative absorbances normalized to the absorption spectrum of D_2O. SWCNT fluorescence is too weak to compete with the strong absorption by H_2O, DMA, DMF, and NMP. Deuterated DMF may work for measuring SWCNT fluorescence of pristine SWCNTs.

After preparing some samples with D_2O/SDS, I was able to get a 3D SWCNT fluorescence spectrum. The contour plot (see Figure C.2) compares well with published spectra for HiPCO SWCNTs.[42,145] When the data is plotted in 3D (see Figure C.3), it is apparent that my samples are not optimal, since the intensity of the peaks is lower than other groups have achieved.

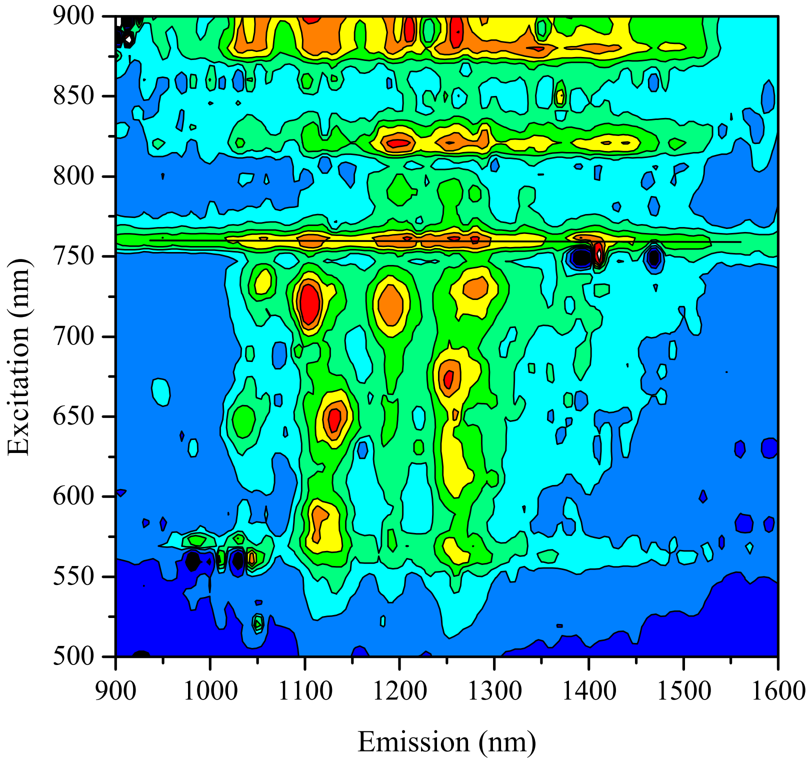

Figure C.2: Contour plot of HiPCO SWCNT fluorescence (D_2O/SDS dispersion).

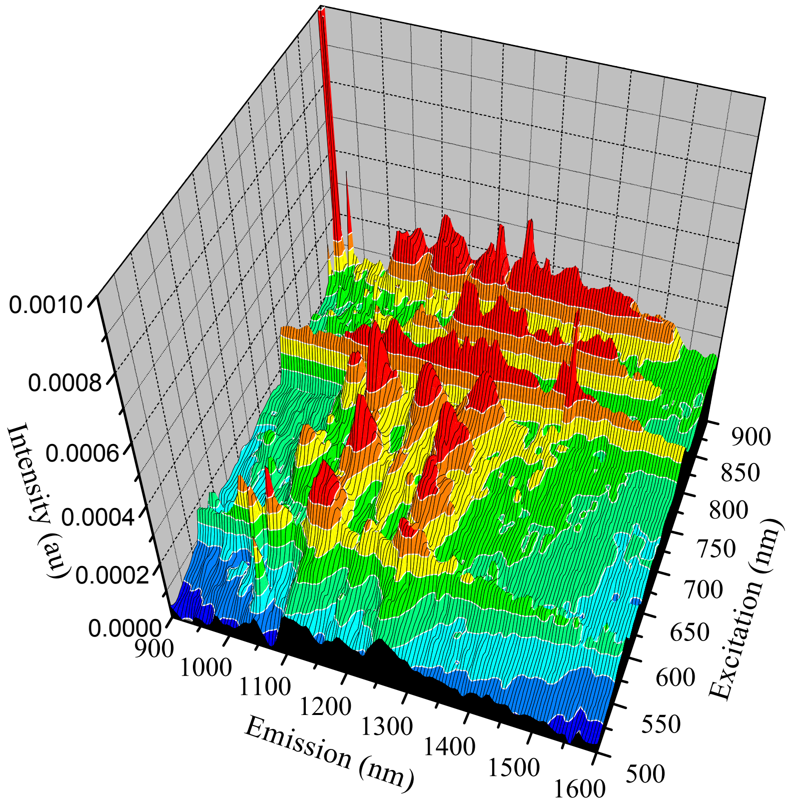

Figure C.3: 3D plot of HiPCO SWCNT fluorescence (D_2O/SDS dispersion).

APPENDIX D: PROCEDURE FOR GROWING VA-CNT FORESTS

D.1 Thermolyne 79300 Furnace Configuration

If this is the first time you are using the CVD system or it has not been used recently, you should check to make sure that the thermal ramp settings are correct. See the furnace manual for detailed instructions on operating the Eurotherm 2416 PID temperature controller. When configuring the PID, you have to specify each step explicitly. To use the thermal ramp profile described in Section 2.4.5, the ramp needs to be set as follows:

1. ProG : LiSt
2. Hb : OFF
3. Hb U : 0
4. rmP.U : min
5. dwL.U : min
6. CYC.n : 1
7. SEG.n : 1
8. tYPE : rmP.t
9. tGt : 700
10. dur : 10.0 (min)
11. SEG.n : 2
12. tYPE : rmP.t

13. tGt : 740
14. dur : 3.0 (min)
15. SEG.n : 3
16. tYPE : rmP.t
17. tGt : 750
18. dur : 20.0 (min)
19. SEG.n : 4
20. tYPE : End
21. End.t : dwEll

D2. Dry Oxidation of Si Chips

Note: if you're working with Octosensis chips, skip this section and go to the Al_2O_3 and Fe deposition section. As described in Section 2.4.3.3, dry oxidation gives us an accurate oxide layer thickness and takes roughly 21 hr to grow 500 nm of SiO_2. First, prepare the Si chips:

1. Use a small wafer tweezers to remove Si chips from the diced wafer
2. Wash the chips with acetone, then methanol
3. Dry the chips with the house nitrogen
4. Cover cleaned chips

Next, then chips must be loaded into the CVD, gas valves adjusted, and the samples get oxidized at 1000 ºC:

1. Load chips onto the ¾" wide quartz slide

2. Pick up the quartz slide with the small wafer tweezers and place it inside the 1” quartz tube
3. Use the quartz pushrod to move the slide 6” into the CVD (use /redraw the marker line that is 4.5” from the bent end of the pushrod – this will put the center of the 3” long slide 6” inside the CVD)
4. Close the black handled valve between the MFCs and the flexible steel mesh gas line
5. Open the red handled valve between the CVD and the compressed air line on the left side of the hood
6. Slowly open the orange compressed air valve on the left side of the hood – adjust the flow so that you can hear it coming out of the CVD, but it does not need to be blasting
7. Make sure that the furnace set point is 1000 ºC
8. Flip the “heat” switch to turn on the furnace
9. After the CVD has reached 1000 ºC, let the samples dry oxidize for 21 hr
10. Shut off the heat and let the CVD cool to room temperature – you can speed up the process slightly by propping the furnace open with the small Al block. I typically let the CVD cool to around 600 ºC, then insert the block to prop the lid open about 1”. After cooling below 400 ºC, I rotate the block to prop the lid open about 2”. Once the CVD is below 200 ºC, I rotate the block again to prop the lid open about 4”. Finally, I open the lid all the way after the CVD is below 100 ºC and allow everything to cool to room temperature

11. Use the pushrod to reach in and pull out the quartz slide – I find it helps to turn the bend end sideways (looks like an L from the top) when passing over the slide
12. Grab the slide with the small wafer tweezers and remove it from the CVD
13. Place the samples in a storage container

D.3 Al_2O_3 and Fe deposition

You will need to use the Lesker PVD 75, in the Grigg cleanroom, to deposit the Al_2O_3 and Fe films. The entire process will probably take 2-2.5 hr. If you have never used the Lesker PVD 75, you will need to be trained by Lou Deguzman (or the current tool manager) before depositing films.

1. Log into the PVD software
2. Check to make sure that both cooling lines are green (“Cooling” tab) and that the crystal health is above 20% (“Sigma” tab) – if either of these has a problem, get the tool manager to fix it before venting the chamber
3. Vent the PVD chamber (takes about 10 min)
4. Replace the clear plastic window guard, if necessary (it should be completely transparent, not coated with metal)
5. Make sure that the Fe crucible is loaded into crucible position #2 and Al_2O_3 crucible is loaded into crucible position #4 – update the “Crucible Setup” Word document, so that other users know what materials are loaded in the PVD
6. Rotate the crucible holder to position #4
7. Remove the sample holder
8. Load samples onto the sample holder, carefully clipping them down
9. Put the sample holder back into the PVD and turn on the rotation (10 RPM)

10. Pump the PVD chamber (takes 20-30 min to get below 6 µT – might benefit from pumping down overnight in the future for higher quality films)
11. Al_2O_3 layer (target thickness: 15 nm)
    a. Set the control switch to manual on the control rack
    b. Set the e-beam pattern to spiral #4 (or the one with a medium spot size)
    c. In the SQS-242 software, select the Al2O3-MWF process
    d. In the Operation software, select “Cru Pos 4” (“Deposition” tab) to activate crucible #4
    e. Turn on the HV (“Deposition” tab)
    f. Slowly bring up the power setpoint in 0.5% increments until you reach 5% power, keeping the chamber pressure below 7 µT – let it soak for 5-10 min
    g. Zero the film thickness in the SQS-242 software
    h. Open the e-beam shutter (“Deposition” tab)
    i. Monitor the deposition rate in the SQS-242 software. Try to stay close to a deposition rate of 1 Å/s – you may have to bring the power up to 6.5%.
    j. The tooling factor for the PVD is approximately 0.184, so to get a 15 nm film, you should deposit Al2O3 until SQS-242 measures a thickness of approximately 0.8150 kÅ (81.5 nm). Close the e-beam shutter a few seconds before reaching 0.8150 kÅ, as it does not close instantaneously
    k. Slowly bring the power back to 0% in 0.5% increments – this should take about 10 min
    l. Click “HV off” (“Deposition” tab) to turn off the high voltage, as it will stay on even if you have 0% power

   m. Wait 10 min to allow the chamber to cool before proceeding with Fe deposition

12. Fe deposition (target thickness: 1 nm)
    a. In the SQS-242 software, select the IronSample-MWF process
    b. Rotate the crucible holder to position #2
    c. In the Operation software, select "Cru Pos 2" ("Deposition" tab) to activate crucible #2
    d. Turn on the HV ("Deposition" tab)
    e. Slowly bring up the power setpoint in 0.5% increments until you reach 4% power, keeping the chamber pressure below 7 μT – let it soak for 5-10 min. It will probably get below 2 μT for this step.
    f. Zero the film thickness in the SQS-242 software
    g. Open the e-beam shutter ("Deposition" tab)
    h. Monitor the deposition rate in the SQS-242 software. Try to stay close to a deposition rate of 0.1-0.2 Å/s – you may have to bring the power up to 4.5%.
    i. The tooling factor for the PVD is approximately 0.184, so to get a 1 nm film, you should deposit Fe until SQS-242 measures a thickness of approximately 0.0543 kÅ (5.43 nm). Close the e-beam shutter a few seconds before reaching 0.0543kÅ, as it does not close instantaneously
    j. Slowly bring the power back to 0% in 0.5% increments – this should take about 10 min

  - k. Click “HV off” (“Deposition” tab) to turn off the high voltage, as it will stay on even if you have 0% power

13. Vent the PVD
14. Unload your samples
15. Start the Pump process before signing out and leaving the tool

D.4 VA-CNT growth

If this is the first time you have used the CVD system for growing CNTs, you should first make sure that the gas tank regulators, gas lines, and MFCs are set up properly.

1. Adjust the regulator so that the pressure on the outgoing line is roughly 20 PSI (if you’re not sure how to do this safely, check with Poler)
2. After you have pressurized the stainless steel gas lines that go to the MFCs, turn on the MKS 247C controller and allow the MFCs to warm up for about an hour before using. NOTE: The MFCs should never be turned on without gas pressure on the inlet, because they can become damaged otherwise.
3. Close the red handled valve between the CVD and the compressed air line on the left side of the hood

After preparing the CVD system, you can proceed with growing CNTs.

1. Flip the switch to turn on the Ar flow (line 1) – it will not immediately start flowing, because there is a pressure valve that needs to be released
2. Slowly turn on the compressed air line on the right side of the hood. You will be able to hear a soft click when the pressure valves for the MFCs open

3. Verify that the Ar flow jumps up to 300 sccm. If the flow rate is incorrect, adjust the setpoint with a small screwdriver
4. Open the black handled valve between the MFCs and the flexible steel mesh gas line to release the building pressure in the gas mixing chamber.
5. Flip the switch to turn on the H_2 flow (line 2)
6. Verify that the H_2 flow is set to 200 sccm. If not, adjust the setpoint
7. Load samples onto the quartz slide and place the slide into the CVD with the small wafer tweezers
8. Use the quartz pushrod to move the slide 6” into the CVD. An experiment showed that there is more carbon deposition at this position than in the center of the CVD
9. Press the “run” button on the furnace to start the ramp program from Section D.1 and flip the “heat” switch
10. Wait 20 min for the thermal ramp and annealing steps (10 min each)
11. Flip the switch to turn on the C_2H_4 flow (line 3)
12. Wait 10 min for growth step to finish
13. Turn off the H_2 and C_2H_4 flows, turn off the heat, and let the CVD cool down to room temperature in the Ar flow
14. Remove samples